Computation of Localized Erosion–Corrosion in Disturbed Two–Phase Flow

A Thesis

Submitted to the Faculty of Graduate Studies and Research

in Partial Fulfillment of the Requirements

for the Degree of

Doctor of Philosophy

in the

Department of Chemical Engineering

University of Saskatchewan, Saskatoon

by

Srdjan Nešić

July, 1991

In presenting this thesis in partial fulfillment of the requirements for a Postgraduate degree from the University of Saskatchewan, I agree that the libraries of this University may make it freely available for inspection. I further agree that permission for copying of this thesis in any manner, in whole or in part, for scholarly purposes may be granted by the professor or professors who supervised my thesis work or, in their absence, by the Head of the Department or the Dean of the College in which my thesis was done. It is understood that any copying or publication or use of this thesis or parts thereof for financial gain shall not be allowed without my written permission. It is also understood that due recognition shall be given to me and the University of Saskatchewan in any scholarly use which may be made of any material in my thesis.

Requests for permission to copy or to make other use of material in this thesis in whole or part should be addressed to:

The Head of the Department of Chemical Engineering

University of Saskatchewan

Saskatoon, Saskatchewan

Canada

S7N 0W0

To my Family

Acknowledgements

Thanks are due in the first place to my supervisor Dr.J.Postlethwaite for his assistance, exceptional support and sound guidance during all stages of my work. His experience and enthusiasm helped me bridge the two fields of engineering science included in this work.

In addition, I would like to thank my committee members: Dr.D.J.Bergstrom, Dr.M.N.Esmail, Dr.S.Yannacopoulos, Dr.G.A.Hill and Dr.N.N.Bakshi for their supervision.

Special thanks to Živana Pavić, my wife, for her support throughout this difficult three-year period.

Financial support came from the University of Saskatchewan in the form of a graduate scholarship and computing facilities.

ABSTRACT

Erosion–corrosion is accelerated corrosion of a metal as a result of the flow removing the protective film from the surface that otherwise slows down the rate of corrosion. In some cases of solid/liquid flows particle-wall impacts can additionally cause erosion of the underlying metal. Study of erosion–corrosion in disturbed two-phase flow requires knowledge from several engineering disciplines including: turbulent fluid flow, particle motion, erosion and corrosion. Very few studies exist that cover this problem adequately especially from a modelling point of view.

This thesis describes the development of a general predictive numerical model for localized erosion–corrosion of metals in disturbed two–phase liquid/solid flow. The flow structure is determined by the application of two-phase flow version of a $\mathbf{k}-\epsilon$ eddy viscosity model (EVM) of turbulence. The Eulerian approach for the fluid flow is coupled with a Lagrangian approach for particle motion. Local values of fluid velocity and turbulent and molecular transport coefficients are determined along with particle–wall interactions in terms of impact velocity, angle and frequency. The corrosion component of the model assumes mass transfer control. The mass transfer rates are determined by the solution of the mass transport equation simultaneously with the fluid flow equations. The erosion is determined on the basis of the computed

particle–wall interactions and cutting wear erosion equations.

Unlike the erosion–corrosion in flow in a straight pipe, or other simple geometries, in disturbed flow there is no obvious relation between the bulk flow parameters and the local rates of erosion-corrosion, so they must be measured or obtained from numerical simulation studies. We have chosen the numerical path with the objective of developing predictive models for erosion–corrosion. Before the developed overall model was verified, each component (e.g. flow, erosion, corrosion) was separately validated.

The hydrodynamic model including two approaches for the near wall region, the wall function approach (WF) and the low Reynolds number approach (LRN), was tested by comparing the predictions with laser Doppler velocimetry (LDV) measurements of liquid flow through a sudden pipe expansion. Satisfactory agreement for the mean flow parameters has been achieved with both approaches.

To validate the model of mass–transfer–controlled corrosion, mass transfer in aqueous, turbulent, recirculating, aqueous flow was simulated with a LRN $k-\epsilon$ EVM model. The predictions were tested against experimental data for flow through a sudden pipe expansion. Good agreement was obtained over a wide range of Reynolds numbers.

The predictions of particle motion made with the two-phase flow model, which includes a EVM $k-\epsilon$ model of turbulence (WF), accompanied with

a Lagrangian particle motion model, have shown an overall good agreement with the LDV measurements, for flow of 0.1% water/sand slurry through a sudden pipe expansion.

Lagrangian models of particle motion provide details of individual particle trajectories and particle–wall impacts. Predictions of erosion rates made with a cutting wear model and based on predicted particle–wall interactions were in good agreement with the erosion measurements, for a water/sand slurry flow through a sudden expansion in a stainless steel pipe.

In the erosion–corrosion process it was assumed that the protective scale was completely removed by the eroding particles. Corrosion rates were calculated on the bases of predicted local oxygen–mass transfer rates. Predictions of metal loss by erosion–corrosion (erosion plus corrosion in our model) were compared with measurements for flow of oxygen saturated 2% water/sand slurry through a mild steel sudden pipe expansion. It was found that the dominant mode of metal loss is corrosion, with the sand removing the protective rust film. The rate of erosion of the base metal was an order of magnitude smaller than the rate of corrosion. The model of erosion-corrosion used was successful in predicting the profile and rates of metal loss in the geometries studied.

After components and the overall model have been successfully verified for flow through a sudden pipe expansion, erosion–corrosion in flow over a groove in a pipe has been predicted to demonstrate the generality of the model.

Contents

List of Figures

List of Tables

Chapter 1

Introduction

Erosion–corrosion can be defined as accelerated corrosion of a metal as a result of the movement of a fluid relative to the metal surface. It is common to assume that the erosion component of the flow is responsible for removing a protective film from the surface that otherwise slows down the rate of corrosion of the base metal. Many other similar definitions exist but they all imply high local rates of metal loss as a result of the moving fluid. Erosion–corrosion is a well recognized and serious problem in many practical situations: erosion–corrosion of steel elements of oil/gas production and distribution pipelines, erosion–corrosion of copper based alloys at the inlet of tube and shell heat exchangers and condensers, erosion–corrosion of slurry pipelines, erosion–corrosion of tees, valves and bends in process plant pipelines, being some of the examples.

Remedies to the erosion–corrosion problem have been mostly concerned

with limiting the velocity of the fluid and using materials that appear to have a better resistance for the given conditions. A more scientific approach has been taken by attempts to simulate the service conditions in laboratories and research the problem in more detail. Small scale tests with rotating discs and cylinders answered some initial questions but fell short of giving comprehensive criteria for onset of accelerated corrosion. The reason lies in the difficulties in transferring the data from these simple flow conditions to practical systems. More was achieved with the experimental flow loops which on a smaller scale simulate the hydrodynamic conditions found in practice. However, in disturbed flows and two–phase flows, which cause most severe erosion–corrosion problems, similarity criteria in a classical sense, become very complicated or fail to exist altogether. Actually, the only similarity criteria available for these situations are the equations describing the individual phenomena such as fluid flow, corrosion and erosion. Thus, the only avenue remaining open is the numerical simulation of the erosion–corrosion phenomena by solving the relevant set of equations. Computer simulations cannot substitute the experiments, as our models are always simplifications of reality, but they can help us reduce the amount of tedious and often expensive experimentation to a minimum.

This work is devoted to studying erosion–corrosion in single and two–phase liquid/solid flow in disturbed flow conditions. It is a natural continuation of the previous work done in the same laboratory on straight pipe erosion–

corrosion in solid/liquid flow. There are a large number of geometries that create disturbed flow conditions that produce severe erosion–corrosion damage. When developing computational models it is essential for the model to retain generality and to be able to handle most of the geometries of interest with the least number of modifications. In our case this can be realized only by solving the fundamental flow, erosion and corrosion equations. The task is not easy as we end up with a set of coupled nonlinear partial differential equations. However, with the appearance of powerful and low cost computers on the market in the last decade the stage has been set for their solution. Even more so by the modern developments of the numerical techniques required for effective computation.

Developments of computational models for two–phase turbulent recirculating flows have gone a long way in the eighties. Further, a substantial body of experimental findings in the field of erosion–corrosion has accumulated over the same period. However, the bridge that would connect the two worlds was very weak. The flow simulation specialists struggled with their own problems in advancing the state of art, but so did the erosion–corrosion scientist in their own field. So, on one hand we have sophisticated computer codes that can solve instantaneous Navier–Stokes equations for turbulent flow with astounding detail and on the other hand researchers are arguing whether to use the bulk Reynolds number as a universal similarity criterion for erosion–corrosion

in the same way as for hydrodynamics. The present work is to a large extent an attempt to bridge the gap between the two fields and to integrate the existing knowledge, resulting in qualitatively and quantitatively new findings.

In Chapter 2 results on previous research in both two–phase flow and erosion–corrosion are reviewed and suggestions are made about the ways to integrate the two fields. In the following chapters the models of fluid flow, particle motion, corrosion and erosion, used in the present study, are described. For fluid flow, the $k-\epsilon$ eddy–viscosity model of turbulence has been coupled with two different models for the boundary conditions: the wall function model (WF) and the low Reynolds number model (LRN). The stochastic Lagrangian model for particle motion has been revised to include the erosion model. Corrosion has been assumed to be under mass transfer control and a full mass transport equation has been solved simultaneously with the flow equations by using the LRN model in the near–wall region.

In Chapter 7 the developed model has been validated by comparing the predictions with available experimental results in literature. Initially, each component of the model has been tested separately. The single–phase flow model, both the WF and the LRN version have been validated with two sets of laser Doppler velocimetry (LDV) measurements for flow through a sudden pipe expansion. The corrosion model was validated with electrochemical mass transfer measurements made under disturbed flow conditions. The par-

ticle motion model was verified against the LDV measurements for dilute liquid/solid flow through a sudden pipe expansion. The erosion predictions made with two different sets of erosion equations were compared with stainless steel erosion measurements. Finally, the overall model of erosion–corrosion was validated with carbon steel erosion–corrosion measurements for a water/sand flow through a sudden pipe expansion, where the corrosion rate was under oxygen–mass–transfer control. Satisfactory agreement was achieved in most tests which verified the adopted assumptions and model constants.

In Chapter 8 conclusions are made and in Chapter 9 the whole work is discussed in terms of its potential for future developments.

Chapter 2

Literature Review

The study of erosion–corrosion in disturbed two-phase flow requires proficiency in a several engineering disciplines including: turbulent fluid flow, particle motion, erosion and corrosion. Since this study is primarily devoted to *modelling* of erosion–corrosion the literature review is focused mainly on the models of the individual phenomena. However, in order to validate the models an insight into some experimental research is needed so several of the more important experimental studies in each discipline are mentioned. The coverage of literature is structured into three main parts: literature on single-phase flow, literature on two-phase flow and literature on erosion–corrosion.

2.1 Single–Phase Flow Studies

In this work the focus is placed upon disturbed flows with separation and reattachment as these are related to some of the most severe erosion–corrosion problems in practice. There are many flow geometries that are of interest but most cases, when simplified, can be classified in one of the few categories: sudden expansion, sudden contraction, groove and protrusion (fence). From a purely hydrodynamic point of view all of these geometries have not been thoroughly studied. The most extensive research has been done on the sudden expansion geometry. Because of its importance as a generic geometry and the wealth of information in the literature, the sudden expansion geometry was selected as a principal test case in this work.

Without going far back into history this literature review focuses on the studies that appeared over the past two decades as this period is marked by rapid developments in both the computational and experimental fields. In the computational field the first numerical models for simulating multidimensional flows have emerged in the early seventies. In parallel, the laser–Doppler velocimetry (LDV) technique enabled nonintrusive accurate measurements of the hydrodynamic parameters.

2.1 Single–Phase Flow Studies

In this work the focus is placed upon disturbed flows with separation and reattachment as these are related to some of the most severe erosion–corrosion problems in practice. There are many flow geometries that are of interest but most cases, when simplified, can be classified in one of the few categories: sudden expansion, sudden contraction, groove and protrusion (fence). From a purely hydrodynamic point of view all of these geometries have not been thoroughly studied. The most extensive research has been done on the sudden expansion geometry. Because of its importance as a generic geometry and the wealth of information in the literature, the sudden expansion geometry was selected as a principal test case in this work.

Without going far back into history this literature review focuses on the studies that appeared over the past two decades as this period is marked by rapid developments in both the computational and experimental fields. In the computational field the first numerical models for simulating multidimensional flows have emerged in the early seventies. In parallel, the laser–Doppler velocimetry (LDV) technique enabled nonintrusive accurate measurements of the hydrodynamic parameters.

2.1.1 Modelling Studies

Models of turbulent flow are often classified as *zero-, one-, two–equation models, stress-equation, large-eddy simulation* and *direct simulation* models.

Prandtl's [1] mixing length model is the best known of the *zero-equation* models. There are a number of other zero-equation models such as the ones of Cebeci and Smith [2] and Crawford and Kays [3]. Such models are relatively simple and useful in many engineering applications but rely heavily on experiments and lack generality.

One–equation[1] models often use the concept of eddy viscosity. One such model employs the Kolmogorov–Prandtl expression $\mu_t = C_\mu \rho k^{0.5} L$ where eddy viscosity μ_t is calculated from the kinetic energy of turbulence k and the mixing length L. A transport equation is solved to obtain k while the length scale L of turbulence has to be prescribed. There is a number of other one–equation models that do not use the eddy viscosity concept such as the model of Bradshaw and Ferris [4]. In general, one-equation models are more successful than zero–equation models but still are not suitable for complex flows where it is difficult to obtain a length scale distribution.

The problems with one–equation models prompted development of *two–*

[1] This number relates to the number of extra transport equations that have to be solved in order to obtain the turbulent stresses. In the Prandtl [1] mixing length approach no new equations had to be solved so it could be considered as the zero-equation model of turbulence.

equation models where an extra equation is solved to obtain the turbulence length scale L. Some propositions included solution of a transport equation for the length scale directly, so called $k - L$ models [5]. Others used indirect methods for obtaining the length scale L by solving transport equations for related variables such as turbulent vorticity ($\mathcal{W} = k/L^2$) [6]. However, one of the most frequently used versions is the model of Jones and Launder [7], where an additional equation for the dissipation rate of turbulence, ϵ is solved. Such a $k - \epsilon$ model is used in this work. The reason is the relative simplicity of the ϵ equation. The $k - \epsilon$ models have been well established for shear–layers and confined recirculating flows and are becoming a powerful tool for solution of many engineering problems.

Stress equation or *Reynolds stress transport models* (RSTM), are based on direct solutions of the transport equations for turbulent stresses. The assumption of isotropy of turbulent stresses, implicitly present in the eddy viscosity models, is removed in the RSTM. The somewhat increased complexity of the equations is counterbalanced by more accurate solutions especially for the turbulent stresses. Although still not used in everyday engineering practice RSTMs are becoming increasingly popular over the last few years.

The most complex of all – the *large–eddy simulation* and *direct simulation* models which rely on direct simulation of instantaneous Navier–Stokes equations, are still out of reach of most researchers. Reasons lie in the fact that

there is a need to simulate a very large scale of turbulent motions directly in time. This is stretching the capabilities of todays fastest computers to the limits.

Even if our review is limited to $k-\epsilon$ models and looks only at the sudden expansion geometry, there is still a very large body of work accumulated over the past 20 years. Thus only several that relate to axisymmetric sudden expansion geometry will be described to outline the state of art in the field.

One of the first numerical studies of complex flows with recirculation was the work of Gosman et al. [8], in which they presented predictions for seven different flow geometries using a $k-\epsilon$ WF flow model. The predictions made for flow through an axisymmetric sudden expansion were compared with the experimental findings of Back and Roschke [9], and good agreement for the reattachment length was reported. However, they reported some discrepancies for the case of swirling flows and bluff body stabilized flow. Some of the problems they had were in part attributed to the performance of their dissipation equation.

Ha Minh and Chassaing [10] presented a study of air flow through a sudden expansion, both confined and unconfined – jet flow. The predictions were made by using an Eddy Viscosity Model (EVM) and a Reynolds Stress Transport Model (RSTM). The authors reported that the agreement between predictions and their own measurements made with hot-wire anemometers was reasonably

good for both models used.

Recently Gould et al. [11] compared the results of predictions made with a $k-\epsilon$ model with their own simultaneous two-component LDV measurements made in the incompressible turbulent air flow field following an axisymmetric expansion. They found good agreement for the mean axial velocity, turbulent kinetic energy, and turbulent shear stresses, but poor agreement for the mean radial velocity and the normal turbulent stresses. The disagreement was partly blamed on the inability of the eddy–viscosity models to account for the anisotropy of the flow.

In an extensive study, Yap [12] evaluated the performance of several turbulence models for near-wall flow by computing momentum and heat transfer in recirculating and impinging flows. In particular he used a $k-\epsilon$ EVM and an Algebraic Stress Model (ASM) to predict the hydrodynamics and heat transfer for flow downstream of a sudden axisymmetric expansion. Near the walls, he considered the use of wall functions, a Low Reynolds Number (LRN) model, and a one equation model of turbulence, the latter two being employed with a fine near-wall grid. The best agreement between predictions and experiments for hydrodynamic and heat transfer data was obtained with an ASM/LRN model [13]. Initially, the predicted heat transfer rates were 5 times higher than those measured; this led to the use of an extra source term in the dissipation equation, which resulted in significantly improved results.

It can be concluded from this short review that there are a number of advanced studies on modelling purely hydrodynamic aspects of turbulent recirculating flows. Some of the studies are concerned with the effect of the hydrodynamics on heat transfer. Mass transfer studies, of interest for our work, such as the numerical study on mixing of helium in turbulent swirling flow in a pipe (Hirai et al. [14]) are rare. Most researchers have used air as the flow medium. The reason is that for modelling purposes liquid flows introduce additional complications, since their high Prandtl–Schmidt numbers prevent equating the heat and mass transfer boundary layers with the hydrodynamic boundary layer.

2.1.2 Experimental Studies

Several good experimental (LDV) studies of flow through a sudden expansion have been published recently, and deserve mentioning.

Khezzar et al. [15] have measured mean and fluctuating velocities and wall static pressure for flow through a sudden expansion for a wide range of Reynolds numbers. They reported the reattachment length to increase with Reynolds number to a maximum of six downstream diameters at Re=800, then decrease to about two diameters at Re=4000 and then remain approximately constant up to Re=40000.

In a study Szczepura [16] reported measurements of mean velocity and

double and triple fluctuating velocity correlations using two-component LDV. He measured water flow through a sudden pipe expansion at $Re = 2 \times 10^5$. The reattachment length was 2.3 downstream diameters and the ocurrence of a small counter-eddy in the corner region was recorded. The reported details and high accuracy of his results made them a benchmark set of results for computational flow studies.

Gould et al. [11] and Durrett et al. [17] in related studies reported measurements of mean and fluctuating velocities and turbulent stresses by simultaneous two–component LDV measurements for air flow through a sudden pipe expansion at $Re = 84000$. Using a special correction lens system they were able to perform measurements on 83% of the pipe radius otherwise difficult because of optical aberrations introduced by the circular tube. They also computed production, diffusion and convection terms for k directly from their measurements. Comparisons with predictions made with their $k - \epsilon$ model were reasonably successful.

The most recent set of benchmark measurements of flow through a sudden pipe expansion was published by Stieglmeier et al. [18] for Re=15600. The problem of making measurements in the near wall region due to refraction of the laser beams on the cylindrical surfaces of the test section was solved by matching the refractive index of the working fluid with that of the containment glass. In addition to the sudden expansion geometry they have also

studied two other diffuser geometries with a 14° and 18° diffuser angles. The authors reported measurements for the mean velocity, all components of the turbulent stresses and the reattachment length. It was observed that for lower diffuser angles the proximity of the diffuser walls after the separation, caused higher mean velocity gradients and production of turbulence, causing faster spreading of the separated shear layer and smaller reattachment lengths. The details of the presented measurements and the small uncertainty errors reported prompted us to select them as the primary source for verification of our flow predictions (Section 7.2.2).

From this brief review it is clear that there are several reliable and detailed experimental LDV studies of flow through a sudden expansion that can be used for validation of computational models. Other geometries of interest such as grooves, fences and constrictions are substantially less researched. However, with the LDV measuring technique becoming cheaper, more user–friendly and altogether more available to researchers over the last decade, it is realistic to expect that the data on the other geometries of interest will appear in the near future.

2.2 Two–Phase Flow Studies

Two–phase flow studies especially on liquid/solid flows are not nearly as numerous as the single–phase flow studies. The reason lies in their complexity. In addition to all the problems encountered in recirculating turbulent single–phase flows, particles add a new set of unknowns through the way they interact with the flow pattern. The two–way coupling between the particles and the mean and turbulent components of fluid flow is still not resolved completely although several good modelling and experimental studies exist.

2.2.1 Modelling Studies

The motion of a dispersed particulate phase within a fluid flow field can be determined by either Lagrangian or Eulerian methods. In the Eulerian or so called *two–fluid* approach the particles are treated as a "second fluid". In other words clouds of particles are treated as a continuum. The resulting equations for particle motion are very similar to the fluid transport equation and so is the solution procedure. In the Lagrangian or *tracking* approach a large number of individual particle trajectories is computed. Mean particle parameters are calculated by averaging. In both approaches coupling between the fluid and particle equations is done through the particle source terms appearing in fluid equations. Both approaches have been studied and several good reviews exist [19], [20].

Eulerian models. Elghobashi et al. [21] have tested an Eulerian two–phase turbulence model previously published by Elgobashi and Abou-Arab [22]. They validated the predictions by comparing them with the measurements of Modarress et al. [23] for flow of a two–phase turbulent axisymmetric gaseous jet and found good agreement for the predictions of the mean and turbulent parameters. They found that additional dissipation of turbulence produced by the relative velocity fluctuations has a significant effect on the jet development.

Rizk and Elgobashi [24] used the same flow model coupled with a low Reynolds number turbulence model proposed by Jones and Launder [7] and simulated the experimental data of Tsuji et al. [25] and Maeda et al. [26] for turbulent gas/particle flow in a vertical pipe. They found that the significant reduction in the fluid turbulent shear stress and turbulent kinetic energy occurs due to the dissipating effect of particles. They suggested that the use of the law-of-the-wall for two–phase flows is in error for loading ratios larger than 0.05%.

Pourahmadi and Humphrey [27] have developed a two–phase flow Eulerian model. They used the same turbulent diffusion coefficient for the particles as Elgobashi et al. [21] determined previously by Peskin [28]. Pourahmadi and Humphrey [27] have demonstrated good agreement of predictions and experimental results for straight pipe two-phase flow as well as for erosion of

bends in ducts for hydraulic transport.

Lagrangian models. Milojević et al. [29], [30] presented a Lagrangian model for particle dispersion which included the two way fluid–particle coupling for both momentum and turbulence equations. The model takes into account the effect of crossing trajectories by accounting for relative velocity between the eddies and the particles as well as adjustment of the particle–eddy interaction to local flow conditions. They compared their results with measurements of Snyder and Lumley [31], Wells and Stock [32], Arnason [33] and their own LDV measurements. Their model was a basis for the work presented in this thesis and is described in details in the sections to follow.

Berlemont et al. [34] developed a Lagrangian model for simulation of particle dispersion in turbulent flow. Based on the flow simulation with a $k-\epsilon$ model they predicted dispersion of both *fluid* and *solid* particles with a Lagrangian model. This enabled them to compute particle–fluid fluctuation–velocity–correlation–matrix and to account for the effect of crossing trajectories. They compared their predictions with the same experiments as the previous study of Milojević et al. [29], [30]. They also predicted the measurements of three two-phase round jets (Modarress et al. [23], Hishida et al. [35] and Shuen et al. [36]) and found good agreement. Some discrepancies found for particle predictions were attributed to inaccurate particle initial conditions.

Comparisons. According to a numerical study by Durst et al. [37], both

Eulerian and Lagrangian methods have their advantages and shortcomings. Eulerian methods are easier to implement and less expensive from the standpoint of computational time. However, Eulerian models contain a larger number of problematical experimental constants that yet need to be confirmed for different flow geometries. Further, for poly–disperse flows, flows with change of particle size along the trajectory (e.g. evaporating droplets) and significant particle–wall interactions, the Lagrangian approach seems advantageous, since it gives more direct information about the particles.

Mostafa and Mongia [38] presented a comparison of Eulerian and Lagrangian models for prediction of turbulent flow of evaporating sprays. They compared their predictions with LDV spray measurements of Solomon et al. [39]. They found that both methods are in good agreement with the measurements. The Eulerian approach that included a model of a poly–disperse particulate phase performed better in the region far from the nozzle. They have tested both a deterministic and a stochastic version of the Lagrangian model. In a cost-of-computing analysis they found that the sequence was, from least to most expensive: single-fraction Eulerian model, deterministic Lagrangian model, multi-fraction Eulerian model, stochastic Lagrangian model. However, the two least expensive models could hardly be considered appropriate for turbulent two-phase flow with particle size change along a trajectory.

Adeniji-Fashola and Chen [40] modelled confined turbulent flow with both

the Eulerian and Lagrangian models. As in other Eulerian models, in order to model particle turbulent dispersion, they used the gradient diffusion approximation coupled with the turbulent Schmidt number for particles, which was equated with kinematic eddy viscosity. In the Lagrangian model they used a stochastic procedure to model a large number of particle trajectories. For validation they used experimental results of Tsuji et al. [25] for vertical upflow of an air/particle mixture in a straight pipe. Somewhat better predictions were obtained with the Eulerian method but they suggested that Lagrangian schemes are more promising for many flows and should be further developed.

So far, concensus has not been reached as to which approach, Eulerian or Lagrangian, is generally better. It seems that benefits and drawbacks have to be estimated for each particular application. For the present study, where detailed information on particle trajectories and particularly particle–wall interactions are essential for erosion modelling, the Lagrangian model is undoubtfully advantageous. The Eulerian model would require an extra set of dubious constants which are difficult to verify.

2.2.2 Experimental Studies

There is not a large number of reliable experimental studies for disturbed fluid/solid flows. The reasons are that these flows are very complex and measurement of the important parameters like mean and fluctuating particle and

fluid velocities, local particle concentrations or particle turbulent dispersion is a very difficult task.

In the sixties and seventies the most successful experimental techniques were the hot wire anemometry for the fluid flow parameters and the fast photography for the particle phase. One of the most interesting studies of this type are measurements of Snyder and Lumley [31] for dispersion of four kinds of different particles from a point source behind a mesh in a vertical air tunnel. They found reduction of particle turbulent dispersion with increased particle terminal velocity due to effect of crossing trajectories.

In the late seventies and the eighties, when the LDV technique was fully established and available, a number of detailed fluid/particle flow studies appeared. Wells and Stock [32] used LDV to study dispersion of 5 and 57 μm glass beads in a horizontal air tunnel with a homogeneous electrostatic field. By electrically charging the particles they studied the effect of crossing trajectories and found that this effect has a more significant effect on particle dispersion than the particle inertia alone.

Lee and Durst [41] used LDV to measure air and particle velocities (100, 200, 400 and 800 μm in diameter) in the case of air/particle flow in a vertical developed turbulent pipe flow. They found a very flat profile of particle axial velocity with particles lagging behind the fluid near the axis and the reverse being true near the walls. This can be explained by radial dispersion of the

particles and their insensitivity to the proximity of the walls (slip condition).

Milojević et al. [30] reported both LDV measurements and predictions of motion of 110 μm glass beads in a confined air/particle jet flow. They found that no equilibrium of momentum exchange was reached between the phases. The motion of particles was heavily influenced by the inlet conditions and due to the mixing, fast moving particles were leading the fluid in the near wall region. It was suggested that movement of particles in the near wall region including the impacts is something requiring further attention.

A number of studies has been published for gas/particle *jet* flows. These include the study of Modarress et al. [23] where a vertical turbulent air jet carrying 50 μm and 200 μm glass beads at different concentrations, was measured with LDV. They developed an original method for distinguishing the signals coming from the larger particles and the small ones used as the fluid tracer. They found a slower spreading of the two–phase flow jet and significant damping of turbulence by the particles. In a similar study Tsuji et al. [25] have used LDV coupled with a specially designed optical fiber probe for particle concentration measurements. They found a delay in the decrease of the centreline velocity and slower spreading of the air/particle jet, this effect being more pronounced for the smaller 170 μm particles rather than for the large 1400 μm ones.

Two-phase flow studies in *disturbed* flow conditions with recirculation are

very rare, most of them appearing in the last five years. Ruck and Makiola [42] have studied particle dispersion in air flow over a single–sided backward–facing step by LDV. They used mono–dispersed particles in the range of 1–70 μm with the 1 μm particles serving as the fluid tracer. They presented mean and turbulent velocity data for both phases and deduced that larger particles have smaller velocity fluctuations which can be explained by their higher inertia and lower sensitivity to fluid turbulence. They also found that the dimensions of the recirculation region decreased with increasing particle size.

Park and Chen [43] have shown LDV measurements of single– and two–phase gas/particle flow of a confined coaxial jet through a sudden expansion. They used 40 μm glass beads and varied the particle loading as well as the relative velocities of the two streams. The observed particle effect was similar to the one in particle–laden free jets. They found the particles to lag behind the fluid near the injector but had a higher mean velocity further downstream which can be explained by the particles not sensing the sudden expansion directly but only through the fluid drag.

Blatt et al. [44] have reported both LDV flow measurements and erosion–corrosion measurements for water carying 1000 ppm of sand through a sudden pipe expansion. They presented axial profiles of mean and turbulent velocity at the centreline and 2 mm from the wall, and related the latter to erosion–corrosion measurements. Their study was selected as one of the test cases in

our work and is described in more detail in Section 7.2.1.

It can be concluded that the database with reliable experimental results for recirculating two-phase flows is somewhat small but has been rapidly growing over the past decade. As new studies emerge we will be able to validate our models for different flow patterns thus increasing the generality and reliability of predictions.

2.3 Erosion–Corrosion Studies

Numerous classifications of erosion–corrosion exist based on the actual phenomenology of the process [45]. However, most special cases of erosion–corrosion can be classified, depending on the nature of the flow, in one of the two categories:

1. erosion–corrosion in single–phase flow

2. erosion–corrosion in multi-phase flow

In the first group we usually encounter situations *with* or *without* the presence of protective films, that normally stifle rates of mass transfer and corrosion. Films are removed at high velocities and at locations in the vicinity of geometrical iregularities.

The second group includes some very severe erosion–corrosion cases such as solid-particle-impact erosion–corrosion, cavitation erosion–corrosion and

liquid-droplet-impact erosion-corrosion. In solid-particle–impact erosion–corrosion protective films are usually almost completely removed by repeated particle impacts. In some cases the underlying metal can be eroded as well.

2.3.1 Single-Phase Flow Erosion–Corrosion

In single–phase flow erosion–corrosion there are two main effects of the flow on erosion–corrosion, both related to altering mass transfer conditions:

- Effect of flow on the corrosion rate by altering the conditions for mass transfer through the fluid boundary layer.
- Effect of flow on the corrosion rate through disrupting the protective films.

In both cases the fluid velocity affects corrosion rate through the change in dynamics of diffusional mass transport, resulting in a change in the interfacial concentrations of the transported species (oxygen, metal-ions).

No films case. The effect of flow on the reaction $M^{z+} + ze \rightleftharpoons M_{solid}$, in the absence of surface films has been discussed by Postlethwaite [46] for a wide range of charge-transfer rate constants and bulk-solution concentrations. The range of rate constants was selected to cover the transition metals such as iron and nickel, which present a large resistance to charge transfer, through to metals such as silver which have a much greater degree of reversibility.

A set of E/i curves was shown for each of the three selected values for the rate constant, each set containing E/i curves for three concentrations, and two Reynolds numbers, one in the laminar, the other in the turbulent flow region. It was shown that there is an effect of mass transport on all the metal deposition (cathodic) curves. For the anodic curves, at the lowest values of the rate constant used, there was no effect of mass transport, whereas at higher values of the rate constant, deviations could be expected if the flow rates were decreased to give increased interfacial concentration of metal-ions, or if supersaturation and film precipitation occurred.

Sydberger and Lotz [47] have presented a study of mass–transfer rates in different flow geometries with sudden obstacles, such as orifices or circumferential slots. As their experiments were done with smooth clean pipes with no scale or deposits, variation in mass transfer was the consequence of the disturbed mass transfer boundary layer alone. Their results suggested that local maxima in mass transfer occured downstream from the obstacles, where increased turbulence occurred. In the analysis the latter authors tried to correlate their mass-transfer results with some universal (global) parameters of the flow, rather than with local flow conditions. However, their experimental findings are very important, as they represent a unique set of measurements for mass transfer in disturbed flow that can be used to validate computational models and their results were used to validate the mass–transfer–controlled

corrosion model as described in Section 7.3.2.

Surface films present. Protective films on metal surfaces present an additional resistance to mass transfer. Thus their presence affects the surface concentration of the species and the corrosion rate. Under flow conditions these films may be partially or completely removed. The structure of the films forming under flow conditions vs. the ones forming under stagnant conditions is different; they appear to be more compact when flow is present [48]. Thus the picture of flow–dependent corrosion is now more complicated. Flow affects rates of mass transfer by increased transport in the fluid phase and by altering the protective films. While the first effect has been sufficiently explained, the effect of single-phase flow on disruption of protective films is still somewhat unclear.

Over the past few decades an attempt was made to find some universal fluid parameters that could be related to onset of accelerated corrosion (triggered by removal of the protective films) including: *velocity* (Copson [49]), *Reynolds number* (Mahato et al. [50]; Shemilt et al. [48]) and *wall shear stress* (Efird [51]; Silverman [52]). In more recent studies (Blatt and Heitz [53]; Nešić and Postlethwaite [54],[55]) the *local near–wall turbulence* has been proposed as a key factor.

For attached flow in a simple geometry such as a straight pipe or a rotating cylinder, an increase in bulk velocity corresponds to an increase in the

Reynolds number and wall shear stress. Higher shear stress creates higher local turbulence levels close to wall and higher rates of mass transfer and corrosion. So, it is acceptable, in such simple flow geometries to use any of the mentioned parameters for correlation of the flow with erosion–corrosion.

However, problems readily arise when results from one simple geometry such as a rotating cylinder, which is a popular system for laboratory studies, are applied to a practical system involving pipes. Similar velocities and Reynolds numbers in the two systems do not guarantee hydrodynamic and mass transfer similarity, so the results from different studies are hardly comparable (Syrett, [56]). Thus use of *breakaway velocities* and *critical Reynolds numbers* as integral similarity criteria has to be ruled out.

However, the use of *wall shear stress* overcomes this problem. In a simple flow geometry with no flow separation, the main source of turbulence is the wall shear stress and it is not surprising that the wall shear stress is a suitable correlating factor for the effect of flow on erosion–corrosion.

Based on the idea that the wall shear stress strips the protective layer of oxide, when its value exceeds the binding force between the film and the base metal, Efird [51] has presented a test technique for determination of the critical shear stress for flow of sea water in copper based alloy pipes. His simplified mechanistic approach has proved to be appealing, as a number of researchers has followed this concept of erosion-corrosion.

Silverman [52] has presented an analysis on the influence of velocity on the rate of corrosion by using a rotating cylinder electrode. His argument that this kind of experiments enables tests with a good control of hydrodynamics is valid, but his choice of the shear stress as a governing variable in erosion-corrosion is limiting. However, Silverman [52] goes one step further from the Effird's [51] mechanistic approach, by adding a hydrodynamical aspect to the action of the shear stress. Shear stress according to the Reynolds analogy of momentum and mass transfer, is related to the mass transfer coefficient. If we consider the assumptions underlying this analogy (Schmidt numbers equal to one and small pressure gradients) acceptable for particular flow conditions, Silverman's proposal that the shear stress is related not only to mechanical removal of the protective film but to the thickness of the mass transfer boundary layer is valid.

In a review paper Syrett [56] has described some of the more important variables affecting erosion-corrosion of copper-nickel alloys in sea water, and suggested a possible mechanism of the process. He implied that all existing mechanistic concepts of explaining the onset of erosion-corrosion with a break-away velocity or even a shear stress that "strips off" the protective oxide layer, are unsatisfactory. He suggested that there is a complex influence of the flow pattern on the removal of the protective film, by chemical and electrochemical mechanisms, but he leaves the reader without any details of how this might

happen. Syrett [56] hinted that the degree of *fluid turbulence* might have a significant effect, which some of the latest studies [53],[54] have shown to be of major importance. Syrett's [56] review has revealed substantial differences in findings of different researchers, who tested the same materials but using a variety of techniques (simulated service test, rotating disc, rotating cylinder, impinging jets, multivelocity jets). His suggestion that the geometry of the test system is important, and that erosion-corrosion is not a simple function of the relative velocity between the water and the metal suggests that the experimental setup should, whenever possible, simulate the industrial conditions (simulated service test).

Disturbed flows. Erosion–corrosion problems encountered in industry often involve disturbed flow conditions at geometrical irregularities such as weld beads or fittings. Under such conditions turbulence is transported downstream from the point of separation and there is no simple relation between the bulk flow parameters and the local near–wall hydrodynamic and mass transfer conditions. In these systems there is no similarity between the wall shear stress and the turbulence profiles, so they must be measured or obtained from numerical simulation studies (Zeisel and Durst, [57]; Nešić and Postlethwaite, [54],[55]).

Turbulent fluctuations interfere with the formation of protective films and also affect the rate of mass transfer of corrosion reactants through the liquid

boundary layer. For example when the reduction of dissolved oxygen is the cathodic reaction, the process of corrosion may be mass transfer controlled (Shemilt, [48]). Following Loss and Heitz [58], we can adopt the concept of a double layer resistance to mass transfer, consisting of the resistance in the protective corrosion film on the metal surface and the resistance in the fluid boundary layer. Intensive turbulence close to the wall probably affects both, by disturbing the mass transfer boundary layer, and by disrupting the protective corrosion layer.

2.3.2 Multi-Phase Flow Erosion–Corrosion

In this work we have limited ourselves to two-phase flow systems, specifically liquid/solid erosion–corrosion. Many of the concepts discussed and especially the models developed can be used to simulate multi–phase erosion–corrosion. However, even erosion–corrosion in two–phase systems is not understood completely at the present time, especially in disturbed flow. One can get a good idea of the complexity of the problem encountered just by realizing that all concepts previously mentioned for two–phase turbulent flow and single–phase erosion–corrosion are here coupled. For example: the turbulent flow affects particle motion; the particles in turn erode the surface films which changes the conditions for mass transfer; this affects the rates of corrosion; corrosion changes the shape of the flow geometry, affecting the flow pattern ....

Postlethwaite et.al. [59] have determined the rates of erosion–corrosion in straight pipes carrying slurries. They concluded that erosion-corrosion in straight pipes is under oxygen mass transfer control with the erosion of the base metal playing a minor role. Successful quantification of the process was possible with the assumption that only the two thirds of the oxygen transferred to the corroding surface accounts for the primary corrosion, with the rest being used in the oxidation of Fe^{2+} to Fe^{3+}. Finally in case of a rough surface produced by erosion–corrosion, oxygen mass transfer was approximately doubled in both single and two-phase flow [91].

Very few papers treat the problem of erosion-corrosion in case of *disturbed* two–phase flow. Lotz and Postlethwaite [60] have measured local erosion-corrosion rates in a segmented tubular flow cell under disturbed turbulent flow conditions at a sudden contraction and a sudden expansion in a pipe. They have determined variations along the length of the test cell with maxima in the constriction and downstream of the expansion. Corrosion of the carbon steel pipe was under oxygen mass transfer control with the rate controlled by the presence of the rust film. Small amounts of suspended solids reduced the thickness of the film thus increasing the rates of metal loss by corrosion. On the other hand the major mode of metal loss for stainless steel pipe specimens was erosion.

In a paper by Blatt et.al. [44] an experimental study of the effect of

disturbed flow conditions of single and two-phase flow systems on erosion-corrosion of ferrous materials in CO_2, was done. LDV was used to determine the hydrodynamical conditions, and weight loss measurements to determine the rates of metal loss. In case of single-phase flow maxima of mass loss corresponded to turbulent fluctuations of the radial flow component near the wall. For the case of slurry flow mass loss measurements corresponded to the radial component of the kinetic energy of particles.

Lotz [61] in a review article on erosion-corrosion in single–, two– and three–phase flow systems, attempted to determine a universal power law of the type:

$$CR = c \times U^a$$

that can cover all modes of metal loss (CR is the corrosion rate, c is a constant and U stands for velocity). Lotz in the end arrived at the values for his constant "a" for: activation control corrosion, mass transfer control corrosion, mixed control corrosion, solid particle activation/repassivation erosion-corrosion, scale removal determined erosion-corrosion, solid particle erosion, liquid droplet impingement erosion and flow cavitation erosion. This work contains a lot of useful information and was probably aimed at helping engineers to understand the role of velocity in metal loss for all mentioned cases. However, the attempt to cover all of them with a simple power law has lead the author to make such simplifications, that the applicability of proposed

correlations is seriously limited. No firm physical argument is given that such a universal law should exist for all mentioned modes of metal loss even for very simple flow geometries.

Zeisel and Durst [57] have presented a complex model for erosion–corrosion in disturbed two–phase flow. They have used a similar $k-\epsilon$ fluid flow model as the one used in the present work but coupled with an Eulerian model for the particles. For erosion they used Finnie's [62] cutting wear equations in addition to Sundararajan and Shewmon's [63] equations for impacts at high angles. Since Zeisel and Durst [57] studied CO_2 corrosion, for activation control they have used the rate equations proposed by DeWaard and Milliams [64]. For validation of their model experimental results of Blatt et al. [44] were used for flow through a sudden constriction and expansion and for flow over a fence in a pipe, and reported reasonable agreement. This paper is very important in a sense that it has shown the right approach for modelling erosion–corrosion in two–phase flow systems. However, it is lacking a lot of details on the actual implementation of the model. Nothing is mentioned about the boundary conditions, it is unclear what mass transfer equation were solved and finally it is unclear how the authors applied an erosion model derived for cutting wear of metals to erosion of surface scales or films of corrosion products.

At the end of this brief literature survey on topics related to erosion–corrosion in disturbed flow one could conclude that the level of knowledge

is quite uneven in different areas. In the field of turbulent single–phase flow the existing theories and models are complicated but give satisfactory predictions compared to accurate LDV measurements. The situation in the two–phase flow area is not as advanced although better models and more accurate measurements are appearing over the past few years. The picture in the erosion–corrosion field is clear only for simple flow geometries and more so for two–phase flow where the solids remove the protective films completely. However, the interaction between the three phenomena, required for study of erosion–corrosion in disturbed two–phase flow, has hardly been explored except for the previously mentioned study of Zeisel and Durst [57]. Thus, that is where the thrust of this work is going to be.

Chapter 3

Two–Phase Flow Model

Following the initial ideas of Migdal and Agosta [65] and the later developments of Milojević [29], [30] a model of two–phase fluid/particle flow has been adopted, where the standard single–phase flow equations are solved by an Eulerian approach, while the particles are treated as sources or sinks of momentum, mass and energy in the fluid. It is assumed that particles have a total volume negligible compared to the total volume of the flow domain.

3.1 Instantaneous Flow Equations

In a Cartesian tensor notation the general 3-D instantaneous equations for flow of fluid/particle mixtures can be obtained by applying a general conservation principle to a continous flow domain:

$$\frac{D\Phi}{D\tau} + \Phi\frac{\partial \tilde{u}_j}{\partial x_j} = \psi \tag{3.1}$$

or

$$\underbrace{\frac{\partial \Phi}{\partial \tau}}_{\text{local change}} = \underbrace{-\frac{\partial}{\partial x_j}(\Phi \tilde{u}_j)}_{\text{convection}} + \underbrace{\psi}_{\text{source}} \tag{3.2}$$

This principle states that change of an arbitrary quantity Φ at any point in the flow domain is a result of the convection and the source or sink of that variable. Now by substituting $\Phi = \rho$ the mass balance or the continuity equation is obtained:

$$\frac{\partial \rho}{\partial \tau} + \frac{\partial}{\partial x_j}(\rho \tilde{u}_j) = \tilde{s}^p_m \tag{3.3}$$

By substituting $\Phi = \rho\tilde{u}_i$ in equation (3.2), a momentum balance is obtained:

$$\frac{\partial}{\partial \tau}(\rho \tilde{u}_i) + \frac{\partial}{\partial x_j}(\rho \tilde{u}_i \tilde{u}_j) = F_j + \frac{\partial \tilde{\sigma}_{ij}}{\partial x_j} + \tilde{s}^p_{u_i} \tag{3.4}$$

In a similar fashion the conservation equation for any scalar quantity can be obtained. For example the balance of a species "s" can be obtained from (3.2) by the substitution $\Phi = \rho\tilde{m}^s$:

$$\frac{\partial}{\partial \tau}(\rho \tilde{m}^s) + \frac{\partial}{\partial x_j}(\rho \tilde{u}_j \tilde{m}^s) = -\frac{\partial \tilde{q}^s_j}{\partial x_j} + \tilde{s}^p_{m^s} \tag{3.5}$$

This equation is also called the convective–diffusion equation. In the same way a heat transport equation can be obtained by writing the conservation equation for thermal energy ($\Phi = \rho h$).

In the previous three conservation equations (3.3),(3.4) and (3.5) the terms on the left hand side (lhs) denote the local and the convective changes respectively, while the right hand side (rhs) contains the source terms. The source terms are split into two parts. The first part of the source terms is inherent to the fluid and is the same as for single–phase flow[1]. The second part of the source terms in equations (3.3),(3.4) and (3.5) arises from the presence of particles and is denoted by $\tilde{s}^p_m, \tilde{s}^p_{u_i}$ and $\tilde{s}^p_m$, which are instantaneous source terms of mass, momentum and species respectively.

The instantaneous stress tensor $\tilde{\sigma}_{ij}$ in the momentum balance (3.4) is:

$$\begin{aligned} \tilde{\sigma}_{ij} &= \tfrac{1}{3}\delta_{ij}\tilde{\sigma}_{kk} + \tilde{\sigma}^d_{ij} \\ &= \underbrace{-\tilde{p}\delta_{ij}}_{\text{mean normal stress}} + \underbrace{\mu\left(\frac{\partial \tilde{u}_j}{\partial x_i} + \frac{\partial \tilde{u}_i}{\partial x_j}\right) - \frac{2}{3}\mu\delta_{ij}\frac{\partial \tilde{u}_k}{\partial x_k}}_{\text{deviatoric stress}} \end{aligned} \tag{3.6}$$

The first term on the rhs of equation (3.6) is the isotropic part of the stress tensor – the mean normal stress and is often called the instantaneous static pressure[2]. The remaining non-isotropic part of the stress tensor $\tilde{\sigma}^d_{ij}$, called the deviatoric stress tensor, has been written by using its linear relationship with

[1]This can be assumed as the total volume of the particles is negligible and the flow domain can be assumed continous.

[2]The value of $\tilde{p}$ of a moving fluid does not have to be the same as in the same fluid at rest.

the non-isotropic part of the strain rate $\tilde{e}^d_{ij}$:

$$\tilde{e}^d_{ij} = \frac{1}{2}\left(\frac{\partial \tilde{u}_j}{\partial x_i} + \frac{\partial \tilde{u}_i}{\partial x_j}\right) - \frac{1}{3}\delta_{ij}\frac{\partial \tilde{u}_k}{\partial x_k} \tag{3.7}$$

which is valid for so called Newtonian fluids:

$$\tilde{\sigma}^d_{ij} = 2\mu\tilde{e}^d_{ij} \tag{3.8}$$

When the expression for $\tilde{\sigma}_{ij}$ is substituted from (3.6) into the momentum balance (3.4), we obtain after some simple manipulations the general instantaneous equation of motion for a compressible Newtonian fluid with particles:

$$\frac{\partial(\rho\tilde{u}_i)}{\partial\tau} + \frac{\partial}{\partial x_j}(\rho\tilde{u}_i\tilde{u}_j) = F_j - \frac{\partial\tilde{p}}{\partial x_i} + \frac{\partial}{\partial x_j}\left[\mu\left(\frac{\partial\tilde{u}_i}{\partial x_j} + \frac{\partial\tilde{u}_j}{\partial x_i}\right)\right] - \frac{2}{3}\frac{\partial}{\partial x_i}\left(\mu\frac{\partial\tilde{u}_k}{\partial x_k}\right) + \tilde{s}^p_{u_i} \tag{3.9}$$

In a similar way the instantaneous mass flux $\tilde{q}^s_j$ of species "s" in the mass balance (3.5) is

$$\tilde{q}^s_j = -D^s_m\frac{\partial\tilde{m}^s}{\partial x_j} \tag{3.10}$$

which is Fick's first law of diffusion. When $\tilde{q}^s_j$ is substituted from equation (3.10) into the mass balance (3.5) a general instantaneous mass transport equation is obtained:

$$\frac{\partial}{\partial \tau}(\rho \tilde{m}^s) + \frac{\partial}{\partial x_j}(\rho \tilde{u}_j \tilde{m}^s) = \frac{\partial}{\partial x_j}\left(D_m^s \frac{\partial \tilde{m}^s}{\partial x_j}\right) + \tilde{s}_{m^s}^p \tag{3.11}$$

Equations (3.3),(3.9) and (3.11) can be used to predict both laminar and turbulent flow and mass transfer[3]. In laminar flow there are no turbulent fluctuations so all instantaneous values can be substituted with mean and the equations solved numerically, which is not an easy task but can be done. However, in turbulent flow the time and length scales of the formed eddies are spread over such a large range that resolving all of them requires an extremely fine grid and small time steps. These problems can be solved only with todays fastest computers. We are forced to simplify the problem.

3.2 Mean Flow Equations

One way to avoid solving the instantaneous flow equations is to solve their time averaged form. Averaging is performed by separating all the instantaneous values on the mean part and the fluctuation (variation) part.

$$\underbrace{\tilde{x}}_{instantaneous} = \underbrace{X}_{mean} + \underbrace{x}_{fluctuation} \tag{3.12}$$

The mean value X is a local value averaged[4] over a time interval $\Delta\tau$:

[3]Here we are assuming that the source terms arising from the presence of the particles are known.

[4]Note that generally X can be a function of time.

$$X = X(\tau) = \frac{1}{\Delta\tau}\int_{\tau-\frac{\Delta\tau}{2}}^{\tau+\frac{\Delta\tau}{2}} \tilde{x}\,d\tau \tag{3.13}$$

while the mean fluctuation is zero:

$$\frac{1}{\Delta\tau}\int_{\tau-\frac{\Delta\tau}{2}}^{\tau+\frac{\Delta\tau}{2}} x\,d\tau = 0 \tag{3.14}$$

Adoption of such an averaging procedure enables all instantaneous values to be divided into the mean and fluctuating component:

$$\tilde{u}_j = U_j + u_j \tag{3.15}$$

$$\tilde{p} = P + p \tag{3.16}$$

$$\tilde{e}_{ij} = E_{ij} + e_{ij} \tag{3.17}$$

$$\tilde{s}^p = S^p + s^p \tag{3.18}$$

$$\tilde{m}^s = M^s + m^s \tag{3.19}$$

By substituting into the instantaneous continuity equation (3.3) we obtain the time averaged continuity equation:

$$\frac{\partial\rho}{\partial\tau} + \frac{\partial}{\partial x_j}(\rho U_j) = S_m^p \tag{3.20}$$

If we limit our discussion to incompressible flow (ρ =const.) and temporarily assume that there is no mass exchange between the fluid and the particles[5]

[5]This is done for the sake of clarity of some of the derivations that follow. We will return to this term in

($S_m^p = 0$), then the continuity equation reduces to:

$$\frac{\partial U_j}{\partial x_j} = 0 \tag{3.21}$$

The momentum equation (3.9) after averaging becomes:

$$\frac{\partial}{\partial \tau}(\rho U_i) + \frac{\partial}{\partial x_j}(\rho U_i U_j) = F_j - \frac{\partial P}{\partial x_i} + \frac{\partial}{\partial x_j}\left[\mu\left(\frac{\partial U_i}{\partial x_j} + \frac{\partial U_i}{\partial x_j}\right) - \rho\overline{u_i u_j}\right] + S_{u_i}^p \tag{3.22}$$

often called the Reynolds equation. Here the incompressibility criterion (3.21) was used. The term $-\rho\overline{u_i u_j}$ is usually denoted as the "turbulent stress" or "Reynolds stress". The momentum source term arising from the particles $S_{u_i}^p$ is equal to the drag force exerted by all the particles present in a control volume and is computed directly in the Lagrangian particle motion model, presented in Chapter 5.

From this point onward we will limit our analysis to a steady state problem. This means that all derivatives with respect to time are zero so first terms of all transport equations can be dropped. Benefits are that the flow analysis becomes simpler as well as the computer time and memory requirements become significantly smaller.

For a three dimensional flow situation the continuity equation (3.20) and the Reynolds equation (3.22) form a set of four scalar equations, with the

the section on discretization of the flow equations.

unknowns being the pressure, three mean velocity components, six components of the turbulent stress and the three source terms that arise from the presence of the particles. Source terms can be determined by solving the particle motion equations (Section 5.6) so they can be considered as known in the fluid flow equations. If there were no turbulent stresses the set of equations would be closed and soluble. In order to solve the system, additional equations are needed for the turbulent stresses which is the problem of so called *turbulence closure* described in the following section.

To continue with our momentum–mass transfer analogy, the instantaneous mass transport equation (3.11) after averaging becomes:

$$\frac{\partial}{\partial \tau}\left(\rho M^s\right)+\frac{\partial}{\partial x_j}\left(\rho U_j M^s\right)=\frac{\partial}{\partial x_j}\left(D_m^s \frac{\partial M^s}{\partial x_j}-\overline{\rho m^s u_j}\right)+S_{m^s}^p \qquad (3.23)$$

The new term on the rhs $-\overline{\rho m^s u_j}$ is the turbulent contribution to mass transport and is an unknown. It requires additional modelling in order to close the system of equations. Here we will temporarily stop the analogy of mass and momentum transfer to make the presentation of the forthcoming derivations less cumbersome. Mass transfer will be considered again in Chapter 4.

3.3 Model of Turbulence

The task of the turbulence models is to provide equations that will enable calculation of the turbulent stresses. This challenging task has not yet been resolved completely although a wide variety of models exist, ranging from very simple ones to very sophisticated. We have adopted a so called Eddy Viscosity Model (EVM) which assumes that the effect of turbulence on the mean flow can be taken into account through viscosity. The turbulent stress is modelled through so called *turbulent* or *eddy viscosity* μ_t:

$$-\rho\overline{u_i u_j} = 2\mu_t \tilde{e}_{ij}^d \tag{3.24}$$

This concept was proposed by Boussinesq [66] in 1877. The effective viscosity can be calculated as a sum of the molecular and turbulent contributions[6].

$$\mu_{eff} = \mu + \mu_t \tag{3.25}$$

The calculation of the turbulent viscosity μ_t is a problem of its own. The first ideas of Prandtl [1] involved the mixing length L:

$$\mu_t = \rho L^2 \left|\frac{\partial U}{\partial y}\right| \tag{3.26}$$

[6]Note that the molecular viscosity μ is a fluid property while the turbulent viscosity μ_t is related to turbulence and is a property of the flow.

which could be determined from some flow geometry parameter such as the distance from the wall.

Kolmogorov [67] and Prandtl [68] have proposed independently that μ_t can be related to the kinetic energy of turbulence $k = \frac{1}{2}\overline{u_i u_j}$ by the expression $\mu_t = C_\mu \rho k^{0.5} L$. The value of k can be determined from a transport equation for the kinetic energy of turbulence and the length scale of turbulence L has to be somehow prescribed. This model can be considered as a one–equation turbulence model. Later two-equation models appeared. The most popular of the two–equation models of turbulence is the $k-\epsilon$ model, where the turbulent viscosity μ_t is determined from the kinetic energy of turbulence k and its dissipation rate ϵ according to the relation:

$$\mu_t = C_\mu f_\mu \rho \frac{k^2}{\epsilon} \tag{3.27}$$

The constant f_μ is equal to one in a fully turbulent flow region. Only in the near–wall region where the flow is directly affected by molecular viscosity is $f_\mu < 1$ as defined in Section 3.5.2.

The dissipation ϵ is:

$$\epsilon = 2\frac{\mu}{\rho}\overline{e_{ij} e_{ij}} \tag{3.28}$$

To obtain k and ϵ the respective transport equations have to be solved.

As mentioned in the literature review, a more elaborate model for turbu-

lence closure is that which solves the transport equation for the turbulent stress $-\rho\overline{u_i u_j}$ directly without requiring Boussinesq's assumption. This approach is often called the Reynolds Stress Transport Model (RSTM). Its shortcomings are: increased computer resources requirements and the problem of prescription of boundary conditions for all stresses along various boundaries, which is a very complex task. One way of removing these disadvantages was found in simplifying the stress transport equation by relating the transport of turbulent stresses to that of the kinetic energy of turbulence k to obtain the so called Algebraic Stress Model (ASM).

In this work we have used the $k-\epsilon$ model for two main reasons. First, this method has been extensively tested over the past two decades and has performed well in most of the test cases. Second, the primary goal of this project was not to develop the most sophisticated model of turbulence but to be able to have a reasonably accurate model of turbulent flow that can be used in the study of erosion–corrosion.

As mentioned earlier, to obtain values for the kinetic energy of turbulence k, the corresponding transport equation has to be derived. This is done by first deriving the equation for the transport of *total* kinetic energy of the flow (which includes the contributions from both the mean flow and the turbulence) either by setting $\Phi = \frac{1}{2}\tilde{u}_i\tilde{u}_i$ in the general transport equation (3.2) and averaging it or by multiplying the instantaneous momentum equation (3.9) with $\tilde{u}_i$ and

averaging it.

The second step is the development of a transport equation for the kinetic energy of the *mean* flow by setting $\Phi = \frac{1}{2}U_iU_i$ in the general transport equation (3.2) and averaging it or by multiplying the averaged momentum equation (3.22) with U_i.

Finally to obtain the transport equation for the kinetic energy of turbulence, the equation for kinetic energy of the *mean* flow is subtracted from the equation for the *total* kinetic energy of the flow. This cumbersome derivation is omitted and can be found in most advanced fluid dynamics textbooks. The final equation has the form:

$$\frac{\partial}{\partial x_j}(\rho U_j k) = -\frac{\partial}{\partial x_j}\left(\overline{u_j p} + \frac{1}{2}\rho\overline{u_i u_i u_j} - 2\mu\overline{u_i e_{ij}}\right) - \rho\overline{u_i u_j}E_{ij} - \rho\epsilon + \overline{s_{u_i}^p u_i} \quad (3.29)$$

The last term denotes the source or sink of kinetic energy of turbulence arising from the presence of the particles and is treated in the way that is well established for other body forces (e.g. buoyancy [69]). In our model it is directly calculated in the Lagrangian particle motion model presented in Chapter 5.

Derivation of the transport equation for the turbulent kinetic energy dissipation rate ϵ is a lengthy procedure and is omitted. First the averaged momentum equation (3.22) is subtracted from the instantaneous momentum

equation (3.9), the result differentiated by x_l, multiplied with $2\nu\frac{\partial u_i}{\partial x_l}$ and finally averaged to yield:

$$\frac{\partial}{\partial x_j}(\rho U_j \epsilon) = -2\mu\overline{\frac{\partial u_i}{\partial x_j}\frac{\partial u_i}{\partial x_l}\frac{\partial u_j}{\partial x_l}} - 2\mu\overline{\left(\frac{\partial^2 u_i}{\partial x_j \partial x_l}\right)^2} - \frac{\partial}{\partial x_j}\left(\overline{\rho U_j \epsilon'} + 2\nu\overline{\frac{\partial u_j}{\partial x_l}\frac{\partial p}{\partial x_i}} - \rho\overline{\frac{\partial \epsilon}{\partial x_j}}\right)$$
$$- 2\mu\left(\overline{\frac{\partial u_i}{\partial x_l}\frac{\partial u_j}{\partial x_l}} + \overline{\frac{\partial u_l}{\partial x_i}\frac{\partial u_l}{\partial x_j}}\right)\frac{\partial U_i}{\partial x_j} - 2\mu u_j\overline{\frac{\partial u_i}{\partial x_l}\frac{\partial^2 U_i}{\partial x_j \partial x_l}} + \mu\overline{\frac{\partial s_{u_i}^2}{\partial x_l}\frac{\partial u_i}{\partial x_l}} \qquad (3.30)$$

The physical meaning of individual terms of this equation is well described in many studies (e.g. Hanjalić et al. [69]). The last term on the rhs is the dissipation source term arising from the particles and is treated in the same way as the effect of other body forces [30].

3.4 Two-Dimensional Fluid/Particle Flow Model

From this point we will further limit our discussion to a two-dimensional[7] (2-D) turbulent flow model that allows for recirculation, thus the corresponding equations are elliptic. In an axisymmetric coordinate system the averaged fluid flow equations have the form:

[7] 2-D models include plane and axisymmetric flows. Two-dimensionality of the model refers to the fact that all variables in the flow domain change in two directions only. However, we can have all three components of the velocity in a 2-D model. 2-D only means that the gradient of all the variables (including all three components of the velocity) is zero in the third direction. Thus, 2-D mathematical models do not have to be associated with 2-D physical space. Further, in a 2-D model the third component of the velocity can change throughout the flow domain but only in two directions.

Continuity equation:

$$\frac{\partial}{\partial x}(\rho U) + \frac{1}{r}\frac{\partial}{\partial r}(r\rho V) = S_m^p \tag{3.31}$$

Momentum equation in axial direction:

$$\begin{aligned}\frac{\partial}{\partial x}(\rho U^2) + \frac{1}{r}\frac{\partial}{\partial r}(r\rho UV) = \frac{\partial}{\partial x}\left(\mu_{eff}\frac{\partial U}{\partial x}\right) + \frac{1}{r}\frac{\partial}{\partial r}\left(r\mu_{eff}\frac{\partial U}{\partial r}\right) \\ + \frac{\partial}{\partial x}\left(\mu_{eff}\frac{\partial U}{\partial x}\right) + \frac{1}{r}\frac{\partial}{\partial r}\left(r\mu_{eff}\frac{\partial V}{\partial x}\right) - \frac{\partial p}{\partial x} + S_U^p\end{aligned} \tag{3.32}$$

Momentum equation in radial direction:

$$\begin{aligned}\frac{\partial}{\partial x}(\rho UV) + \frac{1}{r}\frac{\partial}{\partial r}(r\rho V^2) = \frac{\partial}{\partial x}\left(\mu_{eff}\frac{\partial V}{\partial x}\right) + \frac{1}{r}\frac{\partial}{\partial r}\left(r\mu_{eff}\frac{\partial V}{\partial r}\right) \\ + \frac{\partial}{\partial x}\left(\mu_{eff}\frac{\partial U}{\partial r}\right) + \frac{1}{r}\frac{\partial}{\partial r}\left(r\mu_{eff}\frac{\partial V}{\partial r}\right) - 2\mu_{eff}\frac{V}{r^2} + \rho\frac{W^2}{r} - \frac{\partial P}{\partial r} + S_V^p\end{aligned} \tag{3.33}$$

Momentum equation in tangential direction:

$$\begin{aligned}\frac{\partial}{\partial x}(\rho UW) + \frac{1}{r}\frac{\partial}{\partial r}(r\rho VW) = \frac{\partial}{\partial x}\left(\mu_{eff}\frac{\partial W}{\partial x}\right) + \frac{1}{r}\frac{\partial}{\partial r}\left(r\mu_{eff}\frac{\partial W}{\partial r}\right) \\ - \left(\frac{\mu_{eff}}{r^2} + \frac{\rho V}{r} + \frac{1}{r}\frac{\partial \mu_{eff}}{\partial r}\right)W + S_W^p\end{aligned} \tag{3.34}$$

When in equations for kinetic energy of turbulence (3.29) and its dissipation rate (3.30) all unknown double and triple velocity correlations on the rhs are modelled[8] the final form of the respective equations is:

Equation for kinetic energy of turbulence:

$$\frac{\partial}{\partial x}(\rho U k) + \frac{1}{r}\frac{\partial}{\partial r}(r\rho V k) = \frac{\partial}{\partial x}\left(\frac{\mu_{eff}}{\sigma_k}\frac{\partial k}{\partial x}\right) + \frac{1}{r}\frac{\partial}{\partial r}\left(r\frac{\mu_{eff}}{\sigma_k}\frac{\partial k}{\partial r}\right) + G_{k1} - \rho\epsilon + S_k^p \tag{3.35}$$

Equation for dissipation rate of kinetic energy of turbulence

$$\frac{\partial}{\partial x}(\rho U \epsilon) + \frac{1}{r}\frac{\partial}{\partial r}(r\rho V \epsilon) = \frac{\partial}{\partial x}\left(\frac{\mu_{eff}}{\sigma_\epsilon}\frac{\partial \epsilon}{\partial x}\right) + \frac{1}{r}\frac{\partial}{\partial r}\left(r\frac{\mu_{eff}}{\sigma_\epsilon}\frac{\partial \epsilon}{\partial r}\right) + \frac{\epsilon}{k}(C_{\epsilon 1}G_{k1} - C_{\epsilon 2}\rho\epsilon) + S_\epsilon^p \tag{3.36}$$

[8] It is interesting to notice how in an attempt to solve for the double velocity correlation $-\rho\overline{u_i u_j}$ (turbulent stress) that appears in the averaged momentum equation (3.22) we wrote the transport equations for k (3.29) and ϵ (3.30) in which new unknown double and triple velocity correlations appeared. Thus in an attempt to solve for one unknown we got a few more new ones. We could continue with this process infinitely without being able to close the set of equations. The remedy is to express some of the unknown velocity correlations in terms of known parameters like mean velocities, pressures and their gradients. This is exactly what is done in the approach adopted in the present work, which is common for single–phase flow [69].

In equations (3.35) and (3.36) generation of kinetic energy of turbulence G_{k1} is:

$$G_{k1} = \mu_{eff}\left\{2\left[\left(\frac{\partial U}{\partial x}\right)^2 + \left(\frac{\partial V}{\partial r}\right)^2 + \left(\frac{V}{r}\right)^2\right] + \left(\frac{\partial W}{\partial x}\right)^2 + \left[r\frac{\partial}{\partial r}\left(\frac{W}{r}\right)^2\right] + \left(\frac{\partial U}{\partial r} + \frac{\partial V}{\partial x}\right)^2\right\} \tag{3.37}$$

All terms in the flow equations (3.31)–(3.37) are nearly the same as for the single–phase flow except for the particle–source terms S_U^p, S_V^p, S_W^p, S_k^p and S_ϵ^p that are determined in the Lagrangian model of particle motion (Section 5.6). All of them can be computed directly[9] except the dissipation rate source term S_ϵ^p.

If we assume that particle concentrations are low and that their effect on the flow can be taken into account completely through the source terms, then constants in the turbulence model used are the same as for single–phase flow[10]:

$$C_\mu = 0.09 \qquad C_{\epsilon 1} = 1.44 f_1$$

$$C_{\epsilon 2} = 1.92 f_2 \qquad C_{\epsilon 3} = 0.7$$

$$\sigma_k = 1.0 \qquad \sigma_\epsilon = 1.3$$

[9]This is an advantage over the Eulerian particle-flow models where none of the particle-source terms can be directly computed but have to be modelled which means introduction of few more experimental constants.

[10]The constants f_1 and f_2 are equal to one for fully turbulent flow. In the near–wall region they are modified to account for the direct effect of viscosity as defined in Section 3.5.2.

Equations for the fluid flow (3.31-3.37) are very similar in the Cartesian $x-y$ coordinate system and can be readily derived from above, by setting:

$$\frac{\partial}{\partial r} = \frac{\partial}{\partial y}, \qquad r = 1, \qquad \frac{1}{r^2} = 0 \tag{3.38}$$

which is very convenient for programming purposes.

3.5 Boundary Conditions

Since the set of partial differential flow equations (3.31)–(3.37) is elliptic, it is necessary to define boundary conditions for all variables on all boundaries of the flow domain: inlet, exit, walls and symmetry axis.

At the inlet, the mean and fluctuating velocities, can be taken from measurements or from known velocity profiles for flow in straight pipes [70]. When presenting experimental results in literature, it is common for the turbulence parameters to be expressed via the turbulence intensity ($T_u = \frac{u'}{U}$). Thus for the turbulence inlet boundary condition we can convert T_u data into the k and ϵ values by assuming the turbulence length scale L_ϵ according to Schlichting [70] and writing[11]:

$$k = \frac{3}{2} T_u^2 U^2, \qquad \epsilon = C_\mu^{0.75} \frac{k^{1.5}}{L_\epsilon} \tag{3.39}$$

[11] In case of swirling flow where $W \neq 0$, kinetic energy of turbulence at the inlet is $k = \frac{3}{2} T_u^2 (U^2 + W^2)$

At the exit of the flow domain we can assume that changes of the flow parameters are small or constant[12]. Depending on the problem we can set for the exit:

$$\frac{\partial \Phi}{\partial x} = 0 \qquad \text{or} \qquad \frac{\partial^2 \Phi}{\partial x^2} = 0 \tag{3.40}$$

where $\Phi = U, V, W, k, \epsilon$.

In case of axisymmetric flow we can assume that on the axis the mean radial velocity is zero and gradients of other variables are zero:

$$V = 0 \qquad \text{and} \qquad \frac{\partial \Phi}{\partial y} = 0 \tag{3.41}$$

where $\Phi = U, W, k, \epsilon$.

On the wall all velocities are zero:

$$U = V = W = 0 \tag{3.42}$$

The turbulence model presented is generally valid for high Reynolds number flows. In the vicinity of the walls this model as it is, cannot be applied without modification. The reason is that in the near wall region the effect of viscous forces complicates the picture of turbulence presented. Thus, in the near-wall region there are two basic approaches that have been widely used: universal

[12] This is realistic because we can select the exit of the flow domain far downstream where this is satisfied.

wall functions (WF) model and Low Reynolds Number (LRN) model (e.g. Jones and Launder [7]) Both approaches were used in this work at different stages and both will be described below.

3.5.1 The Wall Function Model

In order to avoid direct modelling of turbulent flow very near solid boundaries (in the viscous sublayer) and the direct influence of viscosity, findings about a universal profile of velocity in the law–of–the–wall region can be used. It has been known for a long time that the profile of velocity in the law–of–the–wall region has a logarithmic character and follows the equation:

$$U^+ = \frac{1}{\kappa}\ln(Ey^+) \tag{3.43}$$

where

$$U^+ = \frac{U_c}{U_\tau}, \qquad U_\tau = \left(\frac{\tau_w}{\rho}\right)^{0.5} \tag{3.44}$$

$$30 < y^+ = \frac{\rho y_c U_\tau}{\mu} < 150$$

Tangential shear stress τ_w at the wall is[13]:

[13] In case of swirling flow there are two non–zero components of the velocity in node "c" closest to the wall: U_c and W_c and two components of the wall shear stress $\tau_{rx\,w}$ and $\tau_{r\theta\,w}$. If ψ is the angle of the velocity vector in respect to the axis in node "c" and we assume that for both velocity components U and W the logarithmic law-of-the wall is valid, then the wall shear stress components are:

$$\tau_w = -\rho C_\mu^{0.25} k_c^{0.5} \frac{\kappa U_c}{\ln(Ey^+)} \tag{3.47}$$

This can be used by placing the first computational node "c" into the law–of–the–wall region $30 < y^+ < 150$ and by assuming that kinetic energy of turbulence k and its dissipation ϵ, in this node, can be obtained from local equilibrium (production of turbulence = dissipation):

$$k_c = \frac{\tau_w}{\rho C_\mu^{0.5}} \tag{3.48}$$

$$\epsilon_c = \frac{C_\mu^{0.75} k_c^{1.5}}{\kappa y_c} \tag{3.49}$$

Constants for the logarithmic boundary layer velocity profile are:

$$\kappa = 0.433, \qquad E = 9.5$$

3.5.2 Low Reynolds Number Model

The WF approach, although less demanding than the LRN model, from the aspects of required memory and CPU time, is known to perform worse than

$$\tau_{rx\,w} = -\rho C_\mu^{0.25} k_c^{0.5} \sqrt{\cos\psi} \frac{\kappa U_c}{\ln(E\sqrt{\cos\psi}y^+)} \tag{3.45}$$

$$\tau_{r\theta\,w} = -\rho C_\mu^{0.25} k_c^{0.5} \sqrt{\sin\psi} \frac{\kappa W_c}{\ln(E\sqrt{\sin\psi}y^+)} \tag{3.46}$$

the LRN approach for recirculating flows [12]. The "universal" velocity profile determined for simple near-wall shear flows, which is employed in the WF approach, is inappropriate when separation or flow reversal are present.

For the purposes of this study it is even more important that for aqueous flows where the Schmidt numbers are of the order of 1000, one can expect the thickness of the mass transfer diffusion controlled boundary sublayer to be an order of magnitude smaller than the thickness of the hydrodynamic viscous sublayer [71]. Thus the WF approach which bridges over the viscous sublayer with a universal velocity profile misses important features of the mass transfer boundary layer deeply embedded within it. Instead, a turbulence model is required which can penetrate deep into the hydrodynamic boundary layer, at the same time accounting for the changes in the turbulence structure due to the wall. This suggests that a LRN approach, which enables the extension of the $k-\epsilon$ turbulence model all the way to the wall, should be used in the case of modelling mass transfer in aqueous flow. The main idea behind the LRN approach is to solve the $k-\epsilon$ equations throughout the flow field, including the viscous sublayer, and then modify turbulence in the near–wall region (by modifying the turbulent viscosity and dissipation). This modification is done by using correction factors, here called "damping functions",which gradually fade out turbulence as the wall is approached.

LRN models were developed in an attempt to reproduce the observed be-

haviour of near-wall turbulence. The constants in the $k-\epsilon$ model of turbulence originally developed for high Reynolds number flows had to be modified in the region near the walls where the effect of molecular viscosity is significant . The correlations obtained were tested for some simple flows such as flow over a flat plate and straight pipe flow [7].

Patel et al. [72] have made a comparative test of seven different low Reynolds number models. Only three models emerged as "successful" when tested against experimental data for flows dominated by proximity to the wall. The model of Lam and Bremhorst [73] was one of the successful ones and has been adopted in the present study. From a physical point of view it is more appealing than the other two recommended models since it operates with the dissipation rate ϵ itself rather than with a "dissipation variable" selected for the sake of computational convenience. More recently, other studies, e.g. [74] have proposed improved LRN models. These models are essentially similar to that of Lam and Bremhorst [73] except for the specific choice of the damping functions f_μ, f_1 and f_2. The model of Lam and Bremhorst [73] was selected for this study, since it contains the essential features of a successful LRN model and has been used in a number of other studies.

In the model of Lam and Bremhorst [73], the damping functions, which are responsible for the modification of the turbulence field in the near-wall region, are given by:

$$f_\mu = [1 - \exp(-0.0165 Re_y)]^2 \left(1 + \frac{20.5}{Re_T}\right)$$

$$f_1 = 1 + \left(\frac{0.05}{f_\mu}\right)^3$$

$$f_2 = 1 - \exp(-Re_T^2) \tag{3.50}$$

where $Re_y = \frac{\rho y \sqrt{k}}{\mu}$ and $Re_T = \frac{\rho k^2}{\mu \epsilon}$.

At the wall the boundary conditions used for k and ϵ are:

$$k = 0, \qquad \frac{\partial \epsilon}{\partial r} = 0$$

3.6 Discretization of the Differential Equations

The numerical method used in this work is based on the control volume approach for discretization of the partial differential equations as proposed by Patankar[14] [75]. The calculation domain is divided into a finite number of control volumes each one containing one grid point.The differential equation is integrated over each control volume resulting in a discretization equation

[14] In his book Patankar [75] has presented in a clear way the whole philosophy underlying the control volume approach for solving the fluid flow and heat and mass transport equations. For many steps in the procedure he presented and explained different options. In this section we will only reiterate some of Patankar's [75] main arguments, describe the chosen path in the present work and outline where the present model diverges from the approach presented in his book.

containing the values of the unknown variable Φ for a group of grid points. In this manner the discretization equation expresses the conservation principle for Φ for a finite (control) volume in the same way that the parent differential equation does for an infinitesimal control volume. For this reason the physical interpretation of the discretized equations in the control volume approach is relatively straightforward.

To simplify the explanation, the discretization procedure will be explained for the case of an orthogonal Cartesian $x-y$ coordinate system. An arbitrary control volume is shown in Fig. 3.1. The corresponding grid point is marked with the letter "P" with the neighbours in the x direction being "E" and "W" (denoting East and West) and in the y direction "N" and "S" (denoting North and South). The dimensions of the control volume are Δx, Δy and the third dimension is unity.

The transport equation for a general variable Φ in a Cartesian coordinate system is:

$$\frac{\partial}{\partial x}(\rho U\Phi)+\frac{\partial}{\partial y}(\rho V\Phi)=\frac{\partial}{\partial x}\left(\Gamma_\Phi\frac{\partial\Phi}{\partial x}\right)+\frac{\partial}{\partial y}\left(\Gamma_\Phi\frac{\partial\Phi}{\partial y}\right)+S_\Phi \qquad (3.51)$$

The lhs represents the convection term. The first two terms on the rhs are the diffusion terms. All other modes of transport of the general variable Φ are contained in the source term S_Φ including the production and destruction

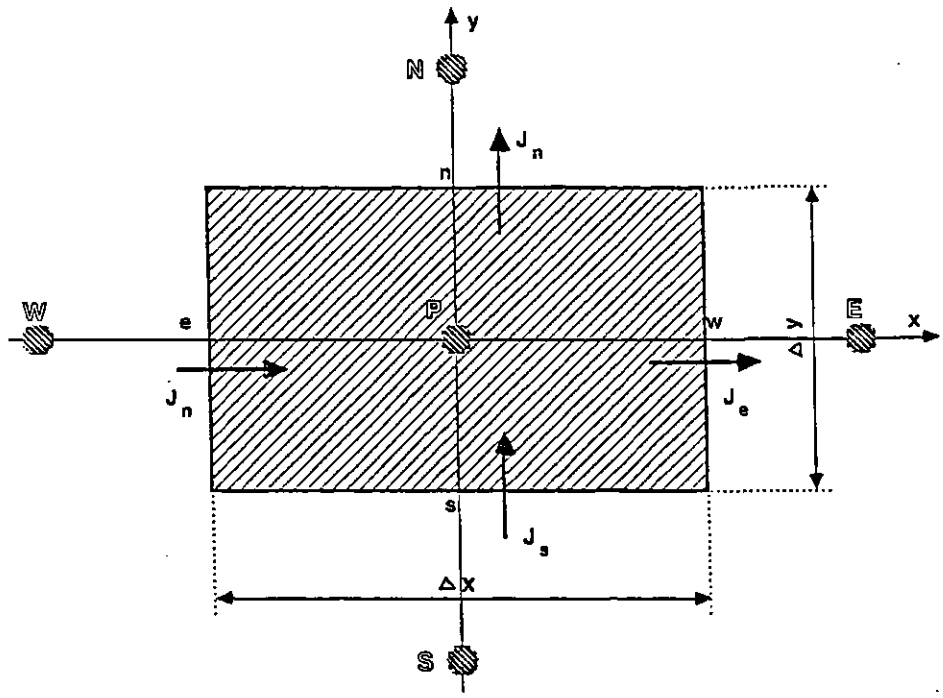

Figure 3.1: Control volume for a general variable ϕ

of Φ.

For the continuity equation $\Phi = 1$ and $\Gamma_\Phi = 0$. When discretized for the control volume "P" shown in Fig. 3.1 the continuity equation becomes:

$$\rho_n V_n A_n - \rho_s V_s A_s + \rho_e U_e A_e - \rho_w U_w A_w = S_m^p \tag{3.52}$$

All terms on lhs are mass fluxes across control volume faces. They express the mass conservation principle for an incompressible fluid stating that any discrepancy between the inlet and outlet flow rates for the control volume is caused by a source or a sink of mass S_m^p in that control volume (since the fluid is incompressible there cannot be any accumulation). In our case S_m^p arises from the particles and it is different from zero only when there is mass transfer between the fluid and the particles as a result of a chemical or a phase

transformation reaction. If we denote the mass flow rate with G then the discretized continuity equation (3.52) becomes:

$$G_n - G_s + G_e - G_w = S_m^p \tag{3.53}$$

Note that in the discretization procedure so far it has been implicitly assumed that the velocity is constant over the face of the control volume (e.g. V_n is constant over the north face of the control volume "P"). This can introduce errors on coarse grids but is inevitable in this discretization method.

Now we return to the general transport equation (3.51). The total flux of a variable Φ through an arbitrary control face is equal to the sum of convection and diffusion:

$$\begin{aligned} J_x^\Phi &= \rho U \Phi - \Gamma_\Phi \frac{\partial \Phi}{\partial x} \\ J_y^\Phi &= \rho V \Phi - \Gamma_\Phi \frac{\partial \Phi}{\partial y} \end{aligned} \tag{3.54}$$

so the general transport equation (3.51) can be written as:

$$\frac{J_x^\Phi}{\partial x} + \frac{J_y^\Phi}{\partial y} = S_\Phi \tag{3.55}$$

When discretized for the same control volume "P" on Fig. 3.1 it becomes:

$$J_n - J_s + J_e - J_w = S_\Phi \tag{3.56}$$

As mentioned, all terms in the transport equation other than convection and diffusion are stored in the source term S_Φ. It can be expected that this term will very often be significant compared to the convective and diffusion terms. Further, S_Φ is usually a function of Φ or its derivatives making equation (3.56) nonlinear, unstable and complicated for numerical solution.

Patankar [75] suggests that a simple and effective way to overcome this problem is to linearize the source term:

$$S_\Phi = S_C + S_P \Phi_P \tag{3.57}$$

The coefficients S_C and S_P can themselves be a function of Φ. Clearly there is a large number of ways that the source term can be linearized with the aid of equation (3.57). Patankar [75] provides guidelines as to how this is to be done in order to maintain stability of the solution procedure.

Now we are ready to proceed with the discretization procedure. If the discretized continuity equation (3.53) is multiplied by the value of Φ in point "P" (Φ_P) and subtracted from the discretized general transport equation (3.56) we obtain[15]:

[15] This manipulation is done for reasons of numerical stability of the solution procedure. When the solution is reached and the continuity equation is satisfied this manipulation does not have an effect. However, during convergence of the solution algorithm the continuity equation is typically not exactly satisfied and the proposed manipulation adds to the numerical stability [75]. This step is equivalent to using the incompressibility criterion in deriving the general differential momentum equation shown on page 41

$$(J_n - G_n\Phi_p) - (J_s - G_s\Phi_p) + (J_e - G_e\Phi_p) - (J_w - G_w\Phi_p) = S_C + S_P\Phi_P - S_m^p\Phi_p \tag{3.58}$$

The last term on the rhs comes from the particles (source of mass) and can be included into the linearized source term (S_C or S_P) in the same way as any other source term. All the "convective–diffusion" fluxes in brackets can be, according to Patankar [75], expressed as:

$$\begin{aligned} J_n - G_n\Phi_p &= a_N(\Phi_P - \Phi_N) \\ J_s - G_s\Phi_p &= a_S(\Phi_S - \Phi_P) \\ J_e - G_e\Phi_p &= a_E(\Phi_P - \Phi_E) \\ J_w - G_w\Phi_p &= a_W(\Phi_W - \Phi_P) \end{aligned} \tag{3.59}$$

where the coefficients a_N,a_S,a_E and a_W are functions of convection and diffusion between the two grid points. In this generalized formulation the choice of the transport coefficient a_N,a_S,a_E and a_W transforms the equations (3.59) into a central difference, upwind, power law or some other discretization scheme. In this work we have used the hybrid scheme which is a combination of a central-difference scheme for low Peclet numbers ($-2 \leq Pe \leq 2$) and an upwind finite difference scheme outside this range. The main criterion for a choice of a

discretization scheme is that it always yields a physically realistic solution[16]. This is achieved by a suitable choice of the transport coefficients a_N, a_S, a_E and a_W; they have always to be positive as Patankar [75] argues. The selected hybrid scheme satisfies this criterion. Further, the S_P part of the linearized source term has to be less or equal to zero.

Finally, when the fluxes are substituted from equation (3.59) into equation (3.58) we get the discretized equation for a general variable Φ in its final form:

$$a_P\Phi_P = a_N\Phi_N + a_S\Phi_S + a_E\Phi_E + a_W\Phi_W + S_C \tag{3.60}$$

where

$$a_P = a_N + a_S + a_E + a_W - S_P$$

The discretized equation (3.60) for each variable Φ is written for everyone of the n_{ij} control volumes in the flow domain. The final step is the solution of the resulting set of algebraic equations, and is described in Section 3.7.

3.6.1 The Momentum Equation

We have so far presented a discretization method that enables solution of a general transport equation. But in case of the momentum equation there is a

[16] On a coarse grid the solution may be inaccurate but still has to be physically realistic. Further, the discretization procedure has to be relatively simple and easy to implement as this has an important effect on the total computing time.

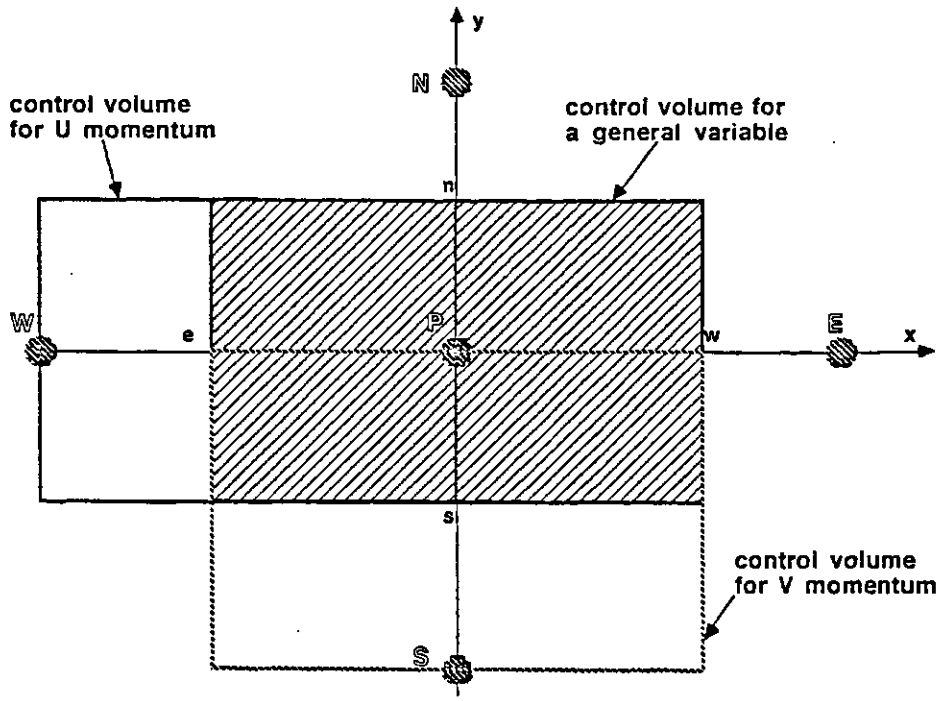

Figure 3.2: Staggered control volumes

difficulty. Its name is pressure.

The problem with the pressure as well as with the continuity equation lies in the way that the first derivatives are discretized. If pressure and velocities are calculated for the same point this will require interpolation of the fluxes on the control volume faces which can yield completely unrealistic wavy pressure and velocity fields. A remedy for this was found in a staggered grid.

In a staggered grid the control volumes used for the momentum equations to obtain velocity are slightly different from the ones used for discretization of the other equations (continuity, k, ϵ, concentration ...). In fact they are staggered as shown on Fig. 3.2 with the control volumes for the U momentum staggered in x direction and the control volumes for the V equation staggered in the y direction only. Pressure, k, ϵ, and concentration are calculated at the point "P"

of the control volume while the velocity components are actually calculated for the points that lie on the faces of the control volume ("n","s","e" and "w" shown in Fig. 3.2). This ensures that the pressure difference calculated between two points becomes the natural driving force for flow between the two points. Unrealistic pressure and velocity fields are avoided as well as the cumbersome interpolation at the control volume faces.

The other problem is that pressure appears in the momentum equations but not in the continuity equation. On the other hand if the pressure field is correct the momentum equations will yield a velocity field that satisfies the continuity equation. This means that pressure is somehow implicitly involved with the continuity equation. But this still does not help us resolve the problem that there is no specific equation that we could solve for obtaining the pressure field. It does not help to dump pressure into the source term as the pressure field is an important and often needed result of the flow simulation. One remedy is eliminating pressure by transforming the momentum equations into vorticity transport equations where pressure terms disappear due to cross differentiation. However, this is avoiding the problem rather than solving it and does not work for three dimensional flows.

The best way is to introduce the pressure into the continuity equation and in that way link it with the momentum equation. Patankar and Spalding [76] have proposed an algorithm for doing exactly that, called SIMPLE (Semi-

Implicit Method for Pressure Linked Equations). In this work we have used the SIMPLE procedure exactly as described by the authors, thus it will not be described in great detail. The main idea is that the continuity equation is modified to include a pressure correction term p' which is, as its name states, a correction of the guessed pressure field p^*.

$$p = p^* + p' \tag{3.61}$$

This is done by eliminating the velocity gradients that appear in the discretized continuity equation by using the discretized momentum equations and a few simple approximations [75]. The resulting equation can be written in the same form (3.60) as all other discretized transport equations. Actually, the modified continuity equation is now called the *pressure–correction equation* as it is used to calculate the new values of pressure correction p' in the iterative process.

The algorithm goes as follows:

1. Start with a guess for the pressure field.
2. Solve the momentum equations for the velocity.
3. Solve the pressure–correction equation to obtain the new values of the pressure–correction p'.
4. Add the pressure–correction to the old (guessed) values of pressure to

obtain an updated pressure field.

5. Treat this updated pressure field as a new guess and return to step 2. Stop when the pressure correction is zero or a sufficiently small number, meaning that the guessed pressure field is the correct one and so is the velocity field.

The boundary condition for the pressure–correction equation are simple and stem from the definition of the pressure–correction itself. On surfaces where the velocity is known (walls, inlet, exit, axis) Patankar [75] shows that there is no change of the pressure–correction:

$$\frac{\partial p'}{\partial x} = 0 \qquad \text{or} \qquad \frac{\partial p'}{\partial y} = 0 \tag{3.62}$$

3.7 Solution of Discretized Equations

By discretizing the flow equations we obtain a set of $n_\Phi \times n_{ij}$ algebraic equations all having the form of the general equation (3.60), where n_Φ is the number of variables and n_{ij} is the number of grid points. Apart from the size of the set of equations, which is in itself a problem, the coefficients of the algebraic equations are generally a function of Φ, which makes them nonlinear and renders simultaneous solution virtually impossible. An iterative sequential method has to be adopted.

In one iteration all equations are solved in a sequence, with the terms that couple them being taken from the latest available iteration. Thus in one iteration the solution of each equation is moved a bit closer to convergence. The alternative way – separate iteration of only one equation for a particular variable at a time until convergence is reached, would be useless as the coefficients in that particular equation are a function of the other variables, and thus are wrong unless the fields of those other variables are correct. In fact we are always solving a set of equations with slightly "wrong" coefficients until we reach convergence for all variables.

For the two dimensional flow domain, the actual solution of the algebraic equations in one iteration is performed line by line. The solution within one line is reached in essence by successive substitution, although the actual procedure is also called the Thomas algorithm or TDMA (Tri–Diagonal Matrix Algorithm) because of the shape of the coefficient matix.

3.8 Convergence of the Solution

Achieving stable convergence of the complex and large set of coupled equations is not an easy task. On one hand there is need to achieve convergence in the shortest possible way and save computing time and on the other there is a need to damp the unavoidable oscillations in the solution procedure by slowing

down the convergence. Both accelerating and decelerating of the convergence procedure can conveniently be achieved with the use of a relaxation factor ξ. If the superscripts $n-1$ and n denote the guessed and computed values of Φ in two successive iterations then the new guess for Φ can be computed as:

$$\Phi = \Phi^{(n-1)} + \xi\left(\Phi^{(n)} - \Phi^{(n-1)}\right)$$

or

$$\Phi = \xi\Phi^{(n)} + (1-\xi)\Phi^{(n-1)} \tag{3.63}$$

By setting $\xi = 1$ the system will converge "naturally" with $\Phi = \Phi^{(n)}$. If ξ is between 0 and 1, Φ will be somewhere in between the guessed value $\Phi^{(n-1)}$ and computed value $\Phi^{(n)}$ and the convergence is slowed down. This is called *underrelaxation.* For $\xi > 1$ the change in Φ will be actually larger than one suggested by the computed value $\Phi^{(n)}$. Thus the convergence is accelerated, but unfortunately so are the oscillations. This is called *overrelaxation.* For a complex nonlinear system, the main concern is to keep it from "falling apart" during iteration. So we perform underrelaxation. Effective viscosity and the pressure correction are underrelaxed directly by using equation (3.63). The other variables are not directly underrelaxed but rather we can underrelax the coefficients in the discretized equations. Patankar [75] shows that the new underrelaxed coefficients are related to the old ones (denoted with a *) by the equations:

$$a_P = \frac{a_P^*}{\xi} \qquad \text{and} \qquad S_C = S_C^* + (1-\xi)\frac{a_P^*}{\xi}\Phi_P^* \tag{3.64}$$

Using underrelaxation of the coefficients rather than direct underrelaxation by means of equation (3.63) saves computer memory space as it is not necessary to store both old and new values of Φ at all times.

The second big problem related to iterative solution algorithms is: when to declare that the system has reached the final solution – convergence. Among many alternatives, we have selected to check how well the discretized transport equations are satisfied for each control volume with the values of the variables in the current iteration. In other words, the balance of each variable for each control volume is checked in every iteration. In that sense the measure of convergence is the so called residual:

$$R = \Sigma a_i \Phi_i + S_C - a_P \Phi_P \tag{3.65}$$

which is determined with the values of the coefficients and variables in the current iteration[17]. In case of a final solution the discretized equation (3.60) is satisfied, so the residual R is equal to zero. In practise it is sufficient to require that R becomes smaller than some given criterion. However, in our implementation the sum of absolute values of residuals for all control volumes

[17] The rhs of equation (3.65) is in effect the discretized transport equation (3.60) so the residual on the lhs shows how much it is in error.

is computed and then normalized. This normalized residual is then monitored and required to be smaller 0.1%. The normalization for the continuity equation is done with the inlet fluid flow rate and for the momentum equation with the inlet momentum rate.

As a double check, one or more locations in the flow domain are monitored to make sure that there is no abrupt change in any variable during the iteration procedure. As final convergence is approached the changes of variables in the whole domain from iteration to iteration should be negligible.

3.9 Algorithm

It is now appropriate time to explain the algorithm of the two–phase flow model. Actually, the overall algorithm will be explained first. The program is based on the TEACH algorithm of Patankar and Spalding [76], it includes the LSD model of Milojević [29], [30] and the erosion and corrosion models developed for this study.

3.9.1 Overall Algorithm

The block diagram of the overall algorithm is shown in Fig. 3.3. The main steps are as follows:

1. Setting the input parameters, preliminary calculations, first guesses for the pressure, velocity, k, ϵ and concentration fields. In the INIT subprogram all necessary geometrical parameters are calculated as well as the initial values fields of other parameters and coefficients. All particle source terms are set to zero (as in single–phase flow).

2. Based on the guessed pressure, velocity and particle source terms fields, the momentum equations (3.32, 3.33, 3.34) are solved by calling the subroutines CALCU, CALCV, CALCW.

3. The continuity equation (3.31) is solved to obtain the pressure correction. The pressure and velocities are corrected, all in subroutine CALCP.

4. The kinetic energy of turbulence equation (3.35) (subroutine CALCTE) and dissipation rate equation (3.36) (subroutine CALCED) are solved as well as the mass transfer equation (4.6) (subroutine CALCMH).

5. The new fields of effective viscosity, diffusivity and other physical parameters are computed in the subroutine PROPS.

6. The residuals are checked according to equation (3.65) for convergence. If not close to the final solution go to step 2.

7. If near the final solution the particle trajectories are solved. Then the new particle source terms, particle-wall interaction including erosion and the other particle parameters are obtained, all in subroutine CALPMM.

8. If convergence is not reached, treat the calculated fields of velocity, pressure, concentration, particle source terms, effective viscosity and diffusivity as a new guess and return to step 2.

9. In case of convergence calculate the final erosion and corrosion rates, wall shear stress, stream function and other output parameters and print fields of all relevant parameters.

3.9.2 Algorithm of the Fluid Flow Subroutines

Since all transport equations for the fluid have a similar structure and so do the discretized equations, it is natural to expect that the structure of all the subroutines for fluid flow and mass transfer(CALCU, CALCV, CALCW, CALCP, CALCTE, CALCED, CALCMH) are very similar. They all have the following characteristic steps in common:

1. Calculation of the actual *volume* of the control volumes and the *area* of the control volume faces.

2. Calculation of flow rates through the control volume faces and the convective coefficients.

3. Interpolation of the effective viscosity on the control volume faces and calculation of the diffusion coefficients.

4. Calculation of the S_C and S_P parts of the linearized source term.

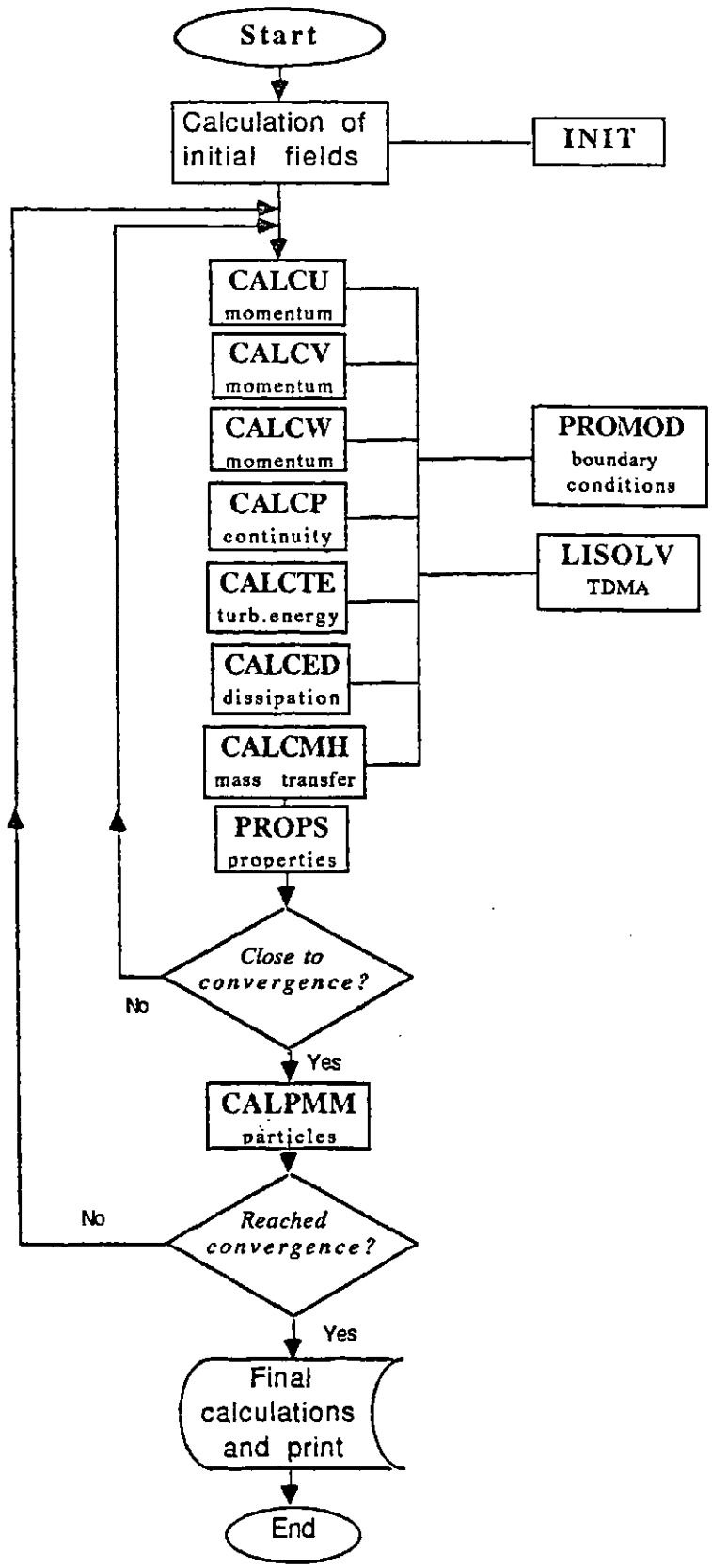

Figure 3.3: The block diagram of the overall algorithm

5. Calculation of the main discretization coefficients a_N,a_S,a_E and a_W according to the adopted hybrid scheme.

6. Repeat steps 1 to 5 for all control volumes in the flow domain.

7. Modification of the main coefficients and source terms for the boundary control volumes as defined in Section 3.5.

8. A new loop for all the control volumes where the a_P coefficient is calculated as well as the residuals. Underrelaxation of the coefficients is done to ensure stability of the solution.

9. Solution of the set of discretized equations in the subroutines LISOLV and LJSOLV in which the TDMA algorithm is used. Since all coefficients are temporary and will be changed in the next overall iteration, only a few TDMA iterations are done with the calculated coefficients to optimize the computing time.

Chapter 4

Model of Corrosion

4.1 Basics of Corrosion Kinetics

Metallic corrosion can be defined as the surface wastage that occurs when metals are exposed to reactive environments. The wastage occurs by an electrochemical reaction – anodic dissolution. An overall corrosion (electrochemical) reaction is composed of two or more elementary electrochemical reactions. In a simple case there is one anodic and one cathodic electrochemical reaction that are in balance. A typical anodic reaction is metal oxidation:

$$M \rightarrow M^{z+} + ze^{-} \tag{4.1}$$

The two major cathodic reactions are: reduction of hydrogen:

$$2H^+ + 2e^- \rightarrow H_2 \tag{4.2}$$

and reduction of oxygen:

$$O_2 + 4H^+ + 4e^- \rightarrow 2H_2O \tag{4.3}$$

In a corrosion process the anodic reaction (metal oxidation) and the cathodic reaction (e.g. hydrogen reduction) are in balance and both occur at the same potential called the corrosion potential E_{corr} (Fig. 4.1a). The corrosion current i_{corr} shows the rate of the corrosion reaction.

In a general case both reactions affect the rate of the overall reaction (mixed control – Fig. 4.1a) However, we might encounter a situation when one or the other reaction is controlling (cathodic, anodic and diffusion control shown on Fig. 4.1b,c and d).

The *diffusion control* case shown in Fig. 4.1d is of specific interest for this study as it denotes a situation where the rate of the overall reaction is controlled by the rate of mass transport of a particular species involved in the electrochemical reaction (e.g. oxygen) and is readily affected by the hydrodynamic conditions.

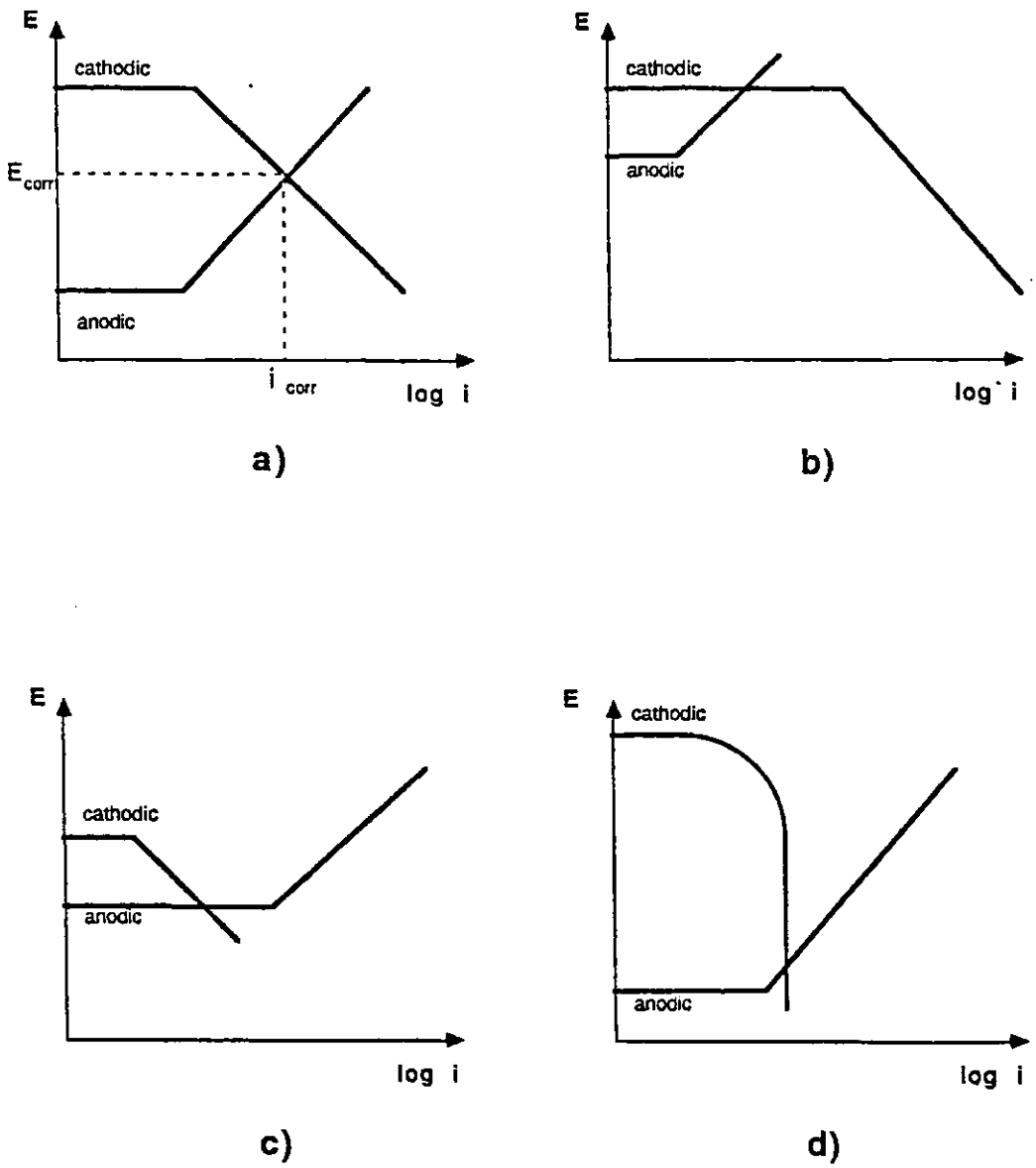

Figure 4.1: Corrosion kinetics diagram a) mixed control b) anodic control c) cathodic control d) diffusion control

4.2 The Mass Transfer Model

In many practical situations the corrosion rate is under mass transfer control. One of the best known examples is oxygen–mass-transfer controlled corrosion of carbon steel. Oxygen–mass transfer controlled corrosion in straight pipelines can be modelled by the application of appropriate mass transfer correlations which relate the Sherwood, Schmidt and Reynolds numbers [59]. This simple approach cannot be applied to corrosion in many practical situations, where the metal loss occurs under conditions of disturbed flow at geometrical iregularities, such as grooves, weld beads, valves and fittings, where the flow separates and/or impinges on the walls. A knowledge of the local flow structure and related mass transfer is required in order to predict the corrosion rate.

Knowledge about the structure of the flow can be obtained by solving the flow equations presented in Chapter 3. Related mass transfer is obtained by solving the full mass transport equation simultaneously with the flow equations. In limiting conditions the concentration of the diffusing species at the wall is set to zero. Local corrosion rates are obtained directly from the calculated local mass fluxes to the wall and the reaction scheme. One such example for the case of oxygen–mass transfer is presented later in Section 7.6.2.

Development of a mass transport equation has been described along with the derivation of the other transport equations in Chapter 3. The last mass

transport equation we have discussed there is the time–averaged convective diffusion equation (3.23):

$$\frac{\partial}{\partial \tau}(\rho M^s) + \frac{\partial}{\partial x_j}(\rho U_j M^s) = \frac{\partial}{\partial x_j}\left(D_m^s \frac{\partial M^s}{\partial x_j} - \rho\overline{m^s u_j}\right) + S_{m^s}^p \qquad (4.4)$$

Here again, we will limit ourselves to a steady state problem, thus the first term on the lhs disappears. Further, we will assume that particles do not directly interfere with transport of our species (there is no chemical or phase transformation reaction between the particles and the fluid) so $S_{m^s}^p = 0$. The terms remaining in equation (4.4) are the convection term, the diffusion term, and the turbulent–mass–transport term. Assuming that the velocities are provided by the flow model, the only unknown term is the turbulent–mass–transport term $-\rho\overline{m^s u_j}$.

Turbulent contribution to mass transport is modelled by an analogy with momentum transfer. Similar to the effective viscosity μ_{eff}, the effective diffusivity D_{eff} can be determined as the sum of the molecular and turbulent contributions, i.e.

$$\begin{aligned} \mu_{eff} &= \mu + \mu_t \\ \underbrace{D_{eff}}_{effective} &= \underbrace{\frac{\mu}{\rho Sc}}_{molecular} + \underbrace{\frac{\mu_t}{\rho\sigma_m}}_{turbulent} \end{aligned} \qquad (4.5)$$

The value of the turbulent Schmidt number $\sigma_m = 0.9$ is according to Kays

and Crawford [77], constant throughout the bulk of the fluid, especially for fluids with high molecular Sc numbers.

With the above assumptions the mass transport equation (4.4) written in an axisymmetric coordinate system becomes:

$$\frac{\partial}{\partial x}(\rho U M^s) + \frac{1}{r}\frac{\partial}{\partial r}(r\rho V M^s) = \frac{\partial}{\partial x}\left(D^s_{eff}\frac{\partial M^s}{\partial x}\right) + \frac{1}{r}\frac{\partial}{\partial r}\left(rD^s_{eff}\frac{\partial M^s}{\partial r}\right) \quad (4.6)$$

As this equation has the same general form as all other transport equations discussed in Chapter 3, everything that has been said about the discretization and solution procedures applies. Even the boundary conditions can be defined in a similar way.

4.2.1 Boundary Conditions

At the inlet the concentration can be considered known from experiments or just given. At the exit and the axis, gradients of concentration are zero. The only problem arises at and close to the walls. In the case of mass-transfer-controlled corrosion the surface concentration can be set to zero.

In the near–wall region two approaches are possible. One can use some universal concentration profile which is an analogy to the WF approach in momentum transfer. This approach is not readily applicable in flows with recirculation. Even more important, for aqueous flows which are characterized with high Sc numbers the mass transfer boundary layer is deeply embedded

in the viscous sublayer which renders the WF approach inappropriate. We would require two different grids for the hydrodynamics and mass transfer.

A far more appealing approach in the near–wall region is to use the LRN approach coupled with the effective diffusivity concept. It can be expected that as turbulent viscosity μ_t defined by equation (3.27) is scaled down in the near–wall region (in a LRN model), so is the turbulent diffusivity $D_t = \frac{\mu_t}{\rho\sigma_m}$. Measurements have indicated that very close to the wall (in the viscous sublayer) the value of σ_m approximately doubles [77], however the exact variation remains to be definitively determined.

Chapter 5

Model of Particle Motion

The motion of a dispersed particulate phase within a turbulent flow field can be modelled by either Lagrangian or Eulerian methods. In Eulerian methods particles are treated as a "second fluid". This is very convenient from a mathematical and numerical standpoint [37] as the resulting equations for the particulate phase are very similar to the ones for the fluid and so is the solution procedure. However, to think about the particles as of a continous quasi–fluid requires a leap of imagination and a number of mathematical and numerical tricks that bridge the gap between the model and reality. Further, the picture of interaction between the fluid and the particles is somewhat fuzzy especially when there is a number of ways that the two phases are coupled. The effect that particles have on the fluid flow, in our two-phase flow model, is accounted for through the source terms. If we applied an Eulerian approach

for the particles all these source terms would have to be additionally "modelled" which means a few more new assumptions and several new empirical constants. These new constants very often do not lend themselves to comprehensive physical interpretation. However, for the purposes of this study it is even more important to be able to determine accurately the interaction of the particles with the walls (impact angles, velocities, frequencies). Here again, the Eulerian models fail to deliver an explicit answer and require new hypotheses and constants. To conclude, Eulerian particle flow models, although easier to implement, prove to be less informative about the specific aspects of the particulate flow, than their Lagrangian counterparts one of which is adopted in this study[1].

In Lagrangian models a large number of individual particle trajectories are calculated in the flow domain. Calculation of the particle–fluid and particle–wall interactions is straightforward and requires no new constants (except for turbulent dissipation). Information about the specific particle parameters (e.g. velocities, concentrations, mass) are easy to extract. This is a special advantage in the case of poly–disperse particulate flows. This all stems from the

[1]It is fair to point out that these arguments are strictly valid only for low particle concentrations (up to 1%vol.). When high particle concentration flows are modelled Lagrangian models become increasingly complicated and most of their advantages are lost. Further, it is much easier to accept that for a 40% particle/fluid mixture the particlulate phase behaves as the *second fluid*. The problematical assumption on the continuity of the particulate phase is much closer to reality. Thus for high particle concentrations Eulerian models should be used.

simplicity of the physical and mathematical models which are basically the ones determined for behaviour of a single particle and those have been well established. However, a price is paid through a more complex numerical model that has to be employed and longer computational times needed to reach the final solution.

5.1 The Lagrangian Stochastic–Deterministic Model

In this work we have adopted the Lagrangian Stochastic–Deterministic (LSD) model of particle motion as proposed by Milojević [29], [30]. The assumptions underlying this model are:

- Particles have a negligibly small volume compared to the total volume of the flow domain thus in every instant they are so far apart from each other that they can be treated as noninterfering;
- Direct particle-particle interactions are negligible, but fluid-particle interactions lead to a two-way coupling;
- External fluxes and stresses act directly on the fluid only;
- Brownian movement of the particles or movement due to pressure gradients and particle rotation is neglected;
- Particles are spherical.

Some of the most important phenomena that will be accounted for are: the momentum exchange between the particles and the fluid, the effect of fluid turbulence on particle dispersion, the effect of particles on turbulence and the interaction between the particles and solid boundaries of the flow domain (walls).

The rather peculiar name " Lagrangian Stochastic–Deterministic Model" was invented by Milojević [29], [30] denoting that the encounter between an eddy and a particle, in the model, is *stochastic* as are the eddy parameters such as instantaneous velocity, lifetime and length. On the other hand the way that the eddy and the particle interact is precisely *determined* by the laws of hydrodynamics.

A large number of particle trajectories are calculated one at a time. Particles are introduced into the flow domain with a discrete number of fractions n_i, from n_j starting locations distributed across the particle inlet cross section. From each starting location, n_k individual trajectories are calculated so the total number of calculated trajectories is $n_i \times n_j \times n_k$.

5.2 Instantaneous Equations of Particle Motion

The motion of a single particle in the flow field is calculated by solution of a instantaneous particle momentum equation:

$$m^p \frac{d\vec{\tilde{V}}^p}{dt} = \frac{1}{2}\rho \tilde{C}_D A^p (\vec{\tilde{V}} - \vec{\tilde{V}}^p)|\vec{\tilde{V}} - \vec{\tilde{V}}^p| + \vec{\tilde{F}} \tag{5.1}$$

where $\vec{\tilde{V}}^p$ and $\vec{\tilde{V}}$ are vectors of instantaneous particle and fluid velocity respectively and $\tilde{C}_D$ is the instantaneous drag coefficient:

$$\tilde{C}_D = \frac{24}{\tilde{Re}^p} \tilde{f}^p \tag{5.2}$$

The instantaneous particle Reynolds number is calculated on the basis of the relative velocity between the particle and the fluid:

$$\tilde{Re}^p = \frac{\rho d^p |\vec{\tilde{V}} - \vec{\tilde{V}}^p|}{\mu} \tag{5.3}$$

The coefficient $\tilde{f}^p$ is:

$$\tilde{f}^p = 1 + 0.15 \tilde{Re}^{p^{0.687}} \text{ for } \quad \tilde{Re}^p \leq 10^3 \tag{5.4}$$

For higher Reynolds numbers the drag coefficient is a constant:

$$\tilde{C}_D = 0.44 \quad \text{for} \quad 10^3 \leq \tilde{Re}^p \leq 2 \times 10^5$$

$$\tilde{C}_D = 0.1 \quad \text{for} \quad \tilde{Re}^p > 2 \times 10^5 \tag{5.5}$$

The equation (5.1) is a form of Newton's second law of mechanics, where the term on lhs is particle acceleration while the rhs represents the acting forces. The first term on rhs is the drag force – the most significant of the

surface forces. $\vec{\tilde{F}}$ denotes all body forces; in this work gravity is the only one taken into account.

In a general case particle motion is three dimensional. In case of an axisymmetric flow with the gravitation acting in the axial direction only, the particle motion equation (5.1) becomes:

$$\frac{d\tilde{u}^p}{d\tau} = \frac{1}{\tilde{\tau}^p}(\tilde{u} - \tilde{u}^p) \pm g(1 - \frac{\rho}{\rho^p}) \tag{5.6}$$

$$\frac{d\tilde{v}^p}{d\tau} = \frac{1}{\tilde{\tau}^p}(\tilde{v} - \tilde{v}^p) + \frac{\tilde{w}^{p^2}}{r} \tag{5.7}$$

$$\frac{d\tilde{w}^p}{d\tau} = \frac{1}{\tilde{\tau}^p}(\tilde{w} - \tilde{w}^p) + \frac{\tilde{w}^p\tilde{v}^p}{r} \tag{5.8}$$

where the particle characteristic (relaxation) time is

$$\tilde{\tau}^p = \frac{m^p}{3\pi\mu\tilde{f}^p d^p} \tag{5.9}$$

This parameter can be interpreted as the time needed for the particle to reach the velocity of the fluid if it kept the current acceleration and nothing else changed.

In the axial momentum equation (5.6) the $\pm$ sign distinguishes between upward (–) and downward (+) orientation of the x axis. The last terms on the rhs of equations (5.7) and (5.8) are the centrifugal and Corriolis acceleration

respectively. Milojević [30] shows that omitting either of these terms can introduce large errors in the prediction of particle dispersion in turbulent pipe flow.

The set of equations (5.6)–(5.8) can be solved numerically (e.g. fourth order Runge–Kutta method). However, it has been shown [30], [37] that from the computer–time standpoint it is more economical to use a recurrence formula obtained by an analytical solution of linearized equation (5.1) for short time intervals $\Delta\tau$. In the vector notation the particle velocity is:

$$\vec{\tilde{V}}^p = \vec{\tilde{V}} - (\vec{\tilde{V}} - \vec{\tilde{V}}^p_o)\exp\left(-\frac{\Delta\tau}{\tilde{\tau}^p}\right) + \frac{\vec{\tilde{F}}}{m^p}\tilde{\tau}^p\left[1 - \exp\left(-\frac{\Delta\tau}{\tilde{\tau}^p}\right)\right] \qquad (5.10)$$

where the subscript "o" denotes the values at the beginning of the time interval $\Delta\tau$. The location of the particle at the end of the time interval $\Delta\tau$ is :

$$\vec{l}^p = \vec{l}^p_o + \Delta\tau\frac{\vec{\tilde{V}}^p_o + \vec{\tilde{V}}^p}{2} \qquad (5.11)$$

5.3 Calculation Procedure

The particle equation (5.10) is made instantaneous (stochastic) by generating a random fluid velocity field around the particle ($\vec{\tilde{V}}$) on the basis of known local turbulence energy and time and length scales. The numerical solution of fluid flow equations provides the fields of mean fluid velocity components

and kinetic energy of turbulence k and its rate of dissipation ϵ. Knowing local k and ϵ values, it is possible to estimate the fluctuating component of the velocity and turbulence time and length scales, corresponding to the large, energy containing eddies.

Fluid velocity fluctuations (u, v, w) are generated independently as random numbers from a Gaussian distribution with a mean of zero and a standard deviation (u', v', w'), which can be determined from the local value of kinetic energy of turbulence:

$$u' = v' = w' = (2k/3)^{0.5} \tag{5.12}$$

Here it is assumed that turbulence is isotropic which is in agreement with the $k - \epsilon$ model of turbulence[2].

The fluctuating components of fluid velocity (u, v, w) are then added to the determined mean fluid velocity components (U, V, W) to obtain the "instantaneous" components $(\tilde{u}, \tilde{v}, \tilde{w})$ of the fluid velocity $(\vec{\tilde{V}})$, which is needed in the equation (5.10) for particle motion.

A particle is in interaction with a particular eddy for a period of time which

[2]In the regions near the walls there is redistribution of turbulence energy from the radial into the axial direction and the isotropy assumption is in error. Here the model allows for calculation of the individual fluctuation velocities (u, v, w) according to an algebraic turbulent stress model [78], [79]. Milojević [30] has shown that this extension of the $k - \epsilon$ model of turbulence did not prove significant for the predictions of the particle motion.

corresponds to a "lifetime" of an eddy (for small particles which follow the fluid motions closely). For larger particles with more inertia the interaction time is shorter and corresponds to the time needed for the particle to "cross" the eddy. So, estimates of the turbulence local time and length scales are needed. As an estimate of the turbulence time scale the local Lagrangian integral time scale T_L is used. T_L can be calculated from local values of kinetic energy of turbulence and its rate of dissipation[3]:

$$T_L = 0.3k/\epsilon \tag{5.13}$$

The "size" of an eddy estimated from local length scale of turbulence L_L is:

$$L_L = u'T_L \tag{5.14}$$

The time that the particle needs to cross the eddy t_t can be determined from the relative velocity between the particle and the fluid[4]:

$$\tau_t = \frac{L_L}{\left|\vec{V} - \vec{V}^p\right|} \tag{5.15}$$

[3]There are a large number of expressions for calculation of T_L. We have used the one that according to Milojević [29], [30] gave best results for predictions of dispersion of particles in a turbulent flow field.

[4]If the estimated size of the eddy is smaller then the particle it is assumed that it does not affect the particle.

This model enables direct accounting for the relative motion between the eddy and the particles, hence enables determination of the effect of "crossing trajectories". Particle–eddy interaction is stopped when either the eddy lifetime is over, or when a particle crosses the eddy. Then a new fluctuation velocity component is generated.

For the accuracy of the solution, choice of the time step $\Delta\tau$ is of great importance. It has to be smaller then the relaxation time $\tilde{\tau}^p$, but also small enough so that we can register the moment the particle crosses the boundaries of the control volume as well as its relative position with respect to the eddies. Milojević [30] suggests that time step $\Delta\tau$ should not be larger than 10% of any of these characteristic times:

$$\Delta\tau = 0.1 \min\left[\tilde{\tau}^p, \frac{\Delta x}{|\tilde{u}^p|}, \frac{\Delta y}{|\tilde{v}^p|}, T_L, \tau_t\right] \tag{5.16}$$

In this way the effect of fluid turbulence on the motion of particles is taken into account. However, so far it has been assumed that the particles sense just the local conditions of the fluid as if the fluid was in a steady state. In reality the turbulent eddies are in vigorous motion as well. Thus a particle caught up in an eddy will travel with it. The particle will sense the conditions of that particular eddy but will also be affected by the local conditions where both the particle and the eddy had moved. This is taken into account through adjusting the fluctuating component of the velocity and the turbulence time and length

scale in accordance with the local conditions as suggested by Milojević [29], [30]. The instantaneous velocity of the fluid that the particle is sensing is constantly adjusted through the fluctuating component according to the local turbulence conditions. The time and length scales of the eddy are adjusted to the local conditions only for the portion that is still remaining in the particle–eddy interaction.

5.4 Boundary Conditions

The boundary conditions for the particles have to be defined on the inlet, the walls and the axis. The inlet conditions for the particles are taken from the experiments: mean velocity and concentration. If the particle fluctuation velocity is not available at the inlet we can assume that it is the same as the fluid counterpart. This assumption is not crucial for liquid/solid flows where the densities are of the same order, as adjustment of particles to the local fluid conditions is reached quickly. In a typical simulation 100–250 starting locations are used across the inlet cross–section.

At the walls a model of simple reflection is used.

$$(\tilde{u}^p_\perp)_R = -\psi_R \tilde{u}^p_\perp \tag{5.17}$$

where

$$\psi_R = \begin{cases} 0-1 & \text{on the wall} \\ 1 & \text{on the axis} \end{cases} \tag{5.18}$$

The reflection coefficient is equal to 1 for a completely elastic impact. For an elastic–plastic impact it is smaller than 1.

On the axis, it can be assumed because of symmetry, that whenever a particle passes the axis there is (effectively) an equivalent one coming from the other side, so the boundary condition is the same as for the elastic reflection of the walls.

5.5 Averaging Procedures

To make the calculation of particle motion compatible with the control volume approach applied for the fluid flow, averaging of particle parameters such as: velocity components and concentration, is performed for the same control volumes as for the fluid[5]. The averaging is done by using the actual number of particles in the particular control volume[6] n^p. If we recall that particles are introduced into the flow domain with a discrete number of size fractions n_i, from n_j starting locations with n_k individual trajectories assigned to each starting location, then f_i,f_j and f_k are the corresponding mass fractions in the

[5]For the whole procedure to make sense it is necessary that the size of the control volume is larger than the size of the largest fraction of the particles simulated.

[6]This makes it analogous to the way it is done in LDV measurements making the comparisons relatively straightforward.

overall particle mass flow rate $\dot{m}^p$. The number of particles $\dot{N}^p_{ijk}$ moving along a particular trajectory "ijk" can be determined as:

$$\dot{N}^p_{ijk} = \frac{\dot{m}^p}{m^p_i} f_i f_j f_k \tag{5.19}$$

where m^p_i is the mass of a single particle of the i-th fraction.

The particle enters the control volume at time τ_1 and leaves it at time τ_2. In the trajectory computation, the residence time $\tau_2 - \tau_1$ is divided into at least 10 shorter time intervals $\Delta\tau$ according to equation (5.16). The average number of particles in a control volume n^p is:

$$n^p = \sum_{i,j,k} \sum_{\tau_1}^{\tau_2} \dot{N}^p_{ijk} \Delta\tau = \sum_{i,j,k} \dot{N}^p_{ijk} (\tau_2 - \tau_1) \tag{5.20}$$

The volume concentration of particles α^p in control volume ΔV is:

$$\alpha^p = \frac{1}{\Delta V} \sum_{i,j,k} \sum_{\tau_1}^{\tau_2} \frac{m^p_i}{\rho^p_i} \dot{N}^p_{ijk} \Delta\tau \tag{5.21}$$

where ρ^p_i is the density of the particles in the i-th fraction.

The average velocity components are determined in the same way as for the fluid, by decomposition on the mean and fluctuating part:

$$\tilde{u}^p = U^p + u^p \tag{5.22}$$

The mean particle velocity in the x direction can be determined as:

$$U^p = \frac{1}{n^p} \sum_{i,j,k} \tilde{u}^p_{ijk} \dot{N}^p_{ijk} \Delta\tau \tag{5.23}$$

In a similar way the other components of the velocity are determined.

By an analogy with the fluid, the particle kinetic energy of turbulence can be defined as:

$$k^p = \frac{1}{2}\overline{(u^{p^2} + v^{p^2} + w^{p^2})} \tag{5.24}$$

and is determined by subtracting the mean kinetic energy of the particles from the total (instantaneous) kinetic energy of the particles,

$$k^p = \frac{1}{2}\frac{1}{n^p} \sum_{i,j,k} \sum_{\tau_1}^{\tau_2} \left[\left(\tilde{u}^{p^2} + \tilde{v}^{p^2} + \tilde{w}^{p^2} \right) \dot{N}^p_{ijk} \Delta\tau \right] - \frac{1}{2} \left(U^{p^2} + V^{p^2} + W^{p^2} \right) \tag{5.25}$$

5.6 The Source Terms

In the model of fluid flow the contribution of particles is accounted for through the source terms. The source terms are calculated after all particle trajectories are computed. For the continuity equation the contribution of particles for a control volume is the amount of mass exchanged between the particles and the fluid by a chemical reaction or a phase transformation.

$$S^p_m = \sum_{i,j,k} (m^p_1 - m^p_2)_{ijk} \dot{N}^p_{ijk} \tag{5.26}$$

In the present study S_m^p is always equal to zero.

The source term for momentum is equal to the total resistance (drag) of all particles in the control volume. In the vector notation it is:

$$\vec{S}_v^p = \sum_{i,j,k} \sum_{\tau_1}^{\tau_2} 3\pi\mu d_i^p \tilde{f}_{ijk}^p \left(\vec{\tilde{V}}_{ijk}^p - \vec{\tilde{V}}\right) \dot{N}_{ijk}^p \Delta\tau \tag{5.27}$$

The source term for the kinetic energy of turbulence as defined in equation (3.29) $S_k^p = \overline{s_{u_i}^p u_i}$, can be directly calculated as:

$$S_k^p = \sum_{i,j,k} \sum_{\tau_1}^{\tau_2} 3\pi\mu d_i^p \tilde{f}_{ijk}^p \left[\left(\tilde{u}_{ijk}^p - \tilde{u}\right)\tilde{u} + \left(\tilde{v}_{ijk}^p - \tilde{v}\right)\tilde{v} + \left(\tilde{w}_{ijk}^p - \tilde{w}\right)\tilde{w}\right] \dot{N}_{ijk}^p \Delta\tau$$
$$- \left(S_U^p U + S_V^p V + S_W^p W\right) \tag{5.28}$$

Finally the source term of dissipation which is the only one modelled, can be related to the source of kinetic energy of turbulence S_k^p:

$$S_\epsilon^p = C_{\epsilon 3} \frac{\epsilon}{k} S_k^p \tag{5.29}$$

The proportionality constant was chosen according to Milojević [29], [30] to be $C_{\epsilon 3} = 0.7$ although very little is known about this term.

5.7 Algorithm of the Particle Motion Subroutine

The algorithm of the subroutine for particle motion based on LSD model of Milojević [29], [30] is sketched on Fig. 5.1. The main steps are:

1. Initial calculations of particle parameters such as particle starting locations and mass fractions and calculation of the time and length scales of turbulence.

2. Start of the loops for n_j starting locations and n_k trajectories on each starting location for n_i particle size fractions.

3. Calculation of the initial particle fluctuation parameters and generation of the first eddy.

4. Calculation of the time step $\Delta\tau$ (equation 5.16) and calculation of the new particle velocity (equation 5.10), coordinate (equation 5.11), as well as increments of the source terms and mean parameters for the time step.

5. Check if the lifetime of the eddy is over or if the particle has crossed the eddy. If yes generate a new eddy by sampling a new fluctuating velocity and computing new time and length scales.

6. If the particle did not cross a control volume boundary go to step 4. Otherwise proceed with the next step.

7. Calculate the contribution of the current trajectory to the source terms for the visited control volume. Update the mean particle parameters for the control volume and adjust the local eddy characteristics.

8. If a boundary of the flow domain is reached, apply the boundary conditions (equation 5.18). If the boundary is the wall calculate the contribution of the current trajectory to the mean particle–wall–impact statistics and erosion rate. If it is not the exit boundary return to step 4. Otherwise proceed with the next step.

9. Return to step 2 and calculate the next particle size fraction. When all particle fractions are computed for the given trajectory move to the next trajectory. When all trajectories are calculated for a given starting location go to a new starting location.

10. When all particle size fractions are calculated, along all trajectories, from all starting locations, the new particle source terms and particle mean parameters are obtained.

11. Final computations and return to the main program.

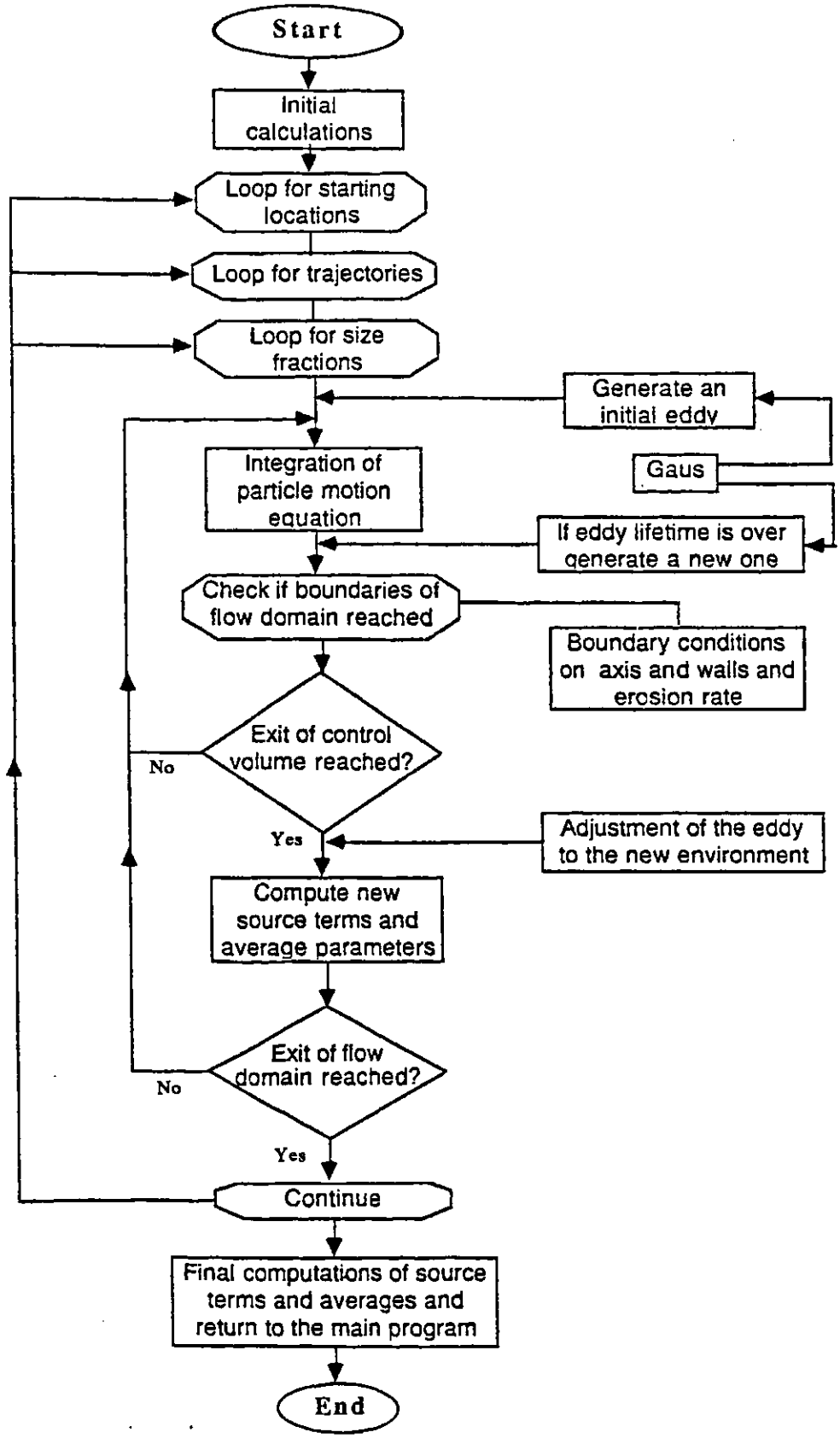

Figure 5.1: Block diagram of the particle motion algorithm

Chapter 6

Model of Erosion

An integral part of the erosion–corrosion process is the erosion component. It is nearly always the protective film that is eroded by the impacting particles. However, if the particles have a high enough energy in some cases the underlying metal can be eroded as well. While erosion of metals has been extensively studied erosion of scales and protective oxide films is still an unknown to a large extent.

For erosion of metals a few competing theories exist starting with the simple and practical Finnie's [62] "cutting" theory to the largely qualitative Levy's [80] "platelet" theory. For our modelling purposes only the quantitative theories can be used and a few, in our opinion the most promising ones, are presented in the sections to follow.

6.1 Definition

When a stream of hard solid particles impacts a surface of a metal, material is removed. This phenomenon, called generally erosion, has been a problem in many industrial operations throughout the years. The process of erosion involves the particles, the eroding surface and usually the fluid which entrains the particles. Accordingly we can divide the numerous factors which influence erosive wear into three main groups:

1. Flow and flow induced parameters
    - Angle of impact
    - Velocity of impact
    - Frequency of impact
    - Corrosive environment
2. Particle properties
    - Size
    - Shape
    - Density
    - Hardness
    - Strength or Friability

3. Eroding Surface Properties

- Geometry
- Hardness
- Elastic limit
- Strength
- Ductility
- Strain hardening
- Charpy impact strength
- Surface temperature

In this study the focus will be placed on the first group of parameters. Particle impact angles, velocity and frequency are in a general case a function of the fluid/particle flow parameters. In the present model particle impact parameters are determined in the part relating to particle motion (Chapter 5).

The erosion rate Q can be defined as mass of material lost per unit time. For most materials erosion rate has been correlated primarily with the impact angle α and impact velocity V, according to a relationship of the form:

$$Q = cV^n \mathcal{F}(\alpha) \tag{6.1}$$

The value of the velocity exponent n is usually found by most investigators to fall within the range 2.0 – 2.5 for metals.

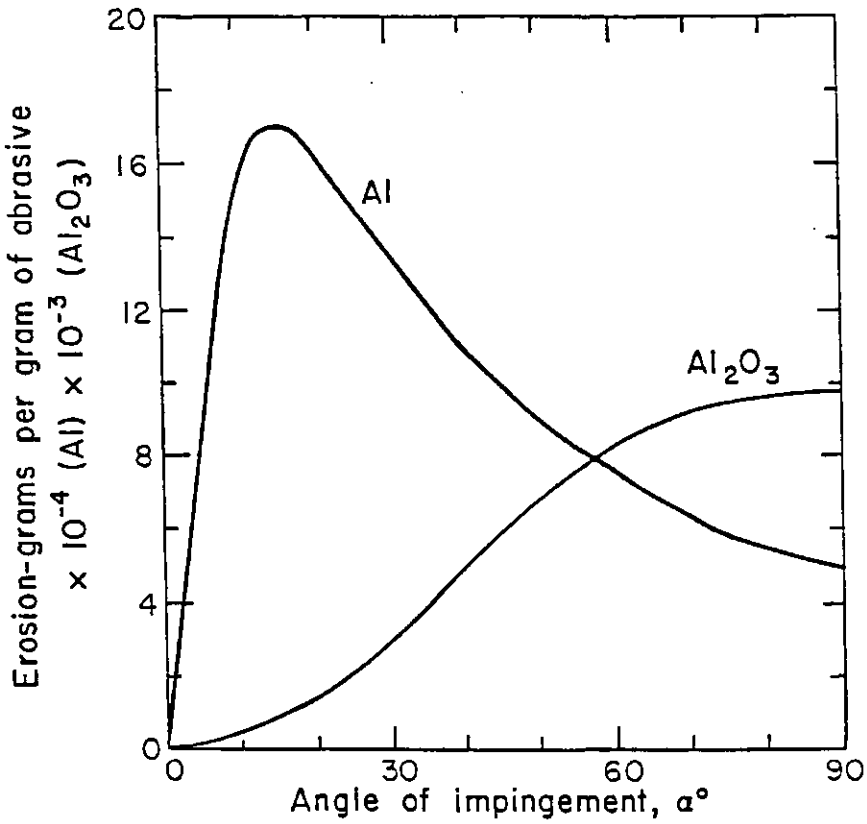

Figure 6.1: Comparison of 1100-0 *Al* and Al_2O_3 eroded by 127 μm *SiC* particles at 152 m/s, data taken from Finnie et al.

The variation of erosion with impact angle $\mathcal{F}(\alpha)$ depends critically on the nature of the materials being eroded. The behaviour observed by Finnie et al. [81] with aluminum (a typical ductile material) and alumina (a brittle ceramic) is shown in Fig. 6.1.

6.2 Cutting Theories of Erosion

In contrast to the relatively well developed theories of fluid/particle flow and corrosion, there is still much controversy as to how erosion actually occurs. A few theories will be presented briefly.

6.2.1 Finnie's Equations

In 1958 Finnie [62] developed an analytical model in an attempt to predict erosion rates, based on the assumption that the mechanism of erosion was cutting (micro–machining). He assumed that the eroding particles cut swaths of metal away as their tips translate along the eroding surface. In case of normal impacts this model predicted no metal removal, with maximum metal loss at low angles.

Finnie's [62] erosion equations have the form:

for $\alpha \leq 18.5^o$

$$Q = \frac{c\check{m}^p(\vec{V}^p)^2}{4\sigma_o}(\sin 2\alpha - 3\sin^2\alpha)$$

for $\alpha > 18.5^o$

$$Q = \frac{c\check{m}^p(\vec{V}^p)^2}{12\sigma_o}\cos^2\alpha \tag{6.2}$$

The major advantage of the above equations is that they are relatively simple and contain, apart from the particle impact parameters, only the material

yield strength, which is easy to obtain. However, equations (6.2) contain an arbitrary constant c, that takes into account the proportion of the particles which impact on the surface, that do the actual damage. Finnie [62] suggested that this constant could be $c \approx 0.5$. This is major shortcoming of his theory as there is little physical meaning that can be assigned to the constant c so it can be viewed as a factor that enables "tuning" of the model to the experimental results.

Further, it was shown recently by Zeisel and Durst [57] that these equations are not suitable for impact angles above 45°. They suggested that at higher angles, erosion rates obtained from Finnie's equations (6.2) should be increased to take into account the "destruction" process at angles close to 90°. Zeisel and Durst [57] have used the model of Sundararajan and Shewmon [63] for erosion at a 90°. This idea is not new. Actually, it had been proposed previously by Bitter [82], [83] in 1963.

6.2.2 Bitter's Equations

Bitter [82], [83] has presented a very elaborate model of erosion that states that total erosive wear can be obtained by addition of *cutting* wear which occurs at low angles and *deformation* wear at higher impact angles. Bitter's [82] equation for deformation wear is:

$$Q_D = \frac{1}{2}\frac{\check{m}^p \left(\vec{V}^p \sin\alpha - V_{cr}\right)^2}{\epsilon} \tag{6.3}$$

where ϵ is the amount of energy needed to remove a unit volume of material by deformation wear. Here a very important concept is involved. Bitter [82] assumes that only the particles that have the normal impact velocity ($V_\perp^p = \vec{V}^p \sin\alpha$) greater than some critical value, for the given material V_{cr}, create plastic deformation and erosion. The particles impacting with a velocity lower than the critical, will create only non–destructive elastic deformation.

For cutting wear Bitter [83] distinguishes between two cases. At lower angles ($\alpha < \alpha_o$) the particle still retains the fraction of the velocity component parallel to the wall $V_\parallel^p = \vec{V}^p \cos\alpha$ as it leaves the body surface. At higher impact angles $V_\parallel$ becomes zero during the impact. The corresponding equations are:

for $\alpha < \alpha_o$

$$Q_C = \frac{2\check{m}^p C_1 \left(\vec{V}^p \sin\alpha - V_{cr}\right)^2}{\sqrt{\vec{V}^p \sin\alpha}} \left(\vec{V}^p \cos\alpha - \frac{C_1 \left(\vec{V}^p \sin\alpha - V_{cr}\right)^2}{\sqrt{\vec{V}^p \sin\alpha}} \varrho\right)$$

for $\alpha \geq \alpha_o$

$$Q_C = \frac{\check{m}^p \left[\vec{V}^{p^2} \cos^2\alpha - C_2 \left(\vec{V}^p \sin\alpha - V_{cr}\right)^{\frac{3}{2}}\right]}{2\varrho} \tag{6.4}$$

where

$$C_1 = \frac{0.228}{\Upsilon}\sqrt[4]{\frac{\rho}{\Upsilon}}$$

$$C_2 = 0.82\Upsilon^2\sqrt[4]{\frac{\rho}{\Upsilon}}\left(\frac{1-\vartheta^{p2}}{\mathcal{E}^p}+\frac{1-\vartheta^{w2}}{\mathcal{E}^w}\right)^2$$

and ϱ is the amount of energy needed to "scratch" out a unit volume from the surface, Υ is the elastic load limit, ϑ is the Poisson's ratio and $\mathcal{E}$ is the Young's modulus.

At every instant the total wear is:

$$Q = Q_D + Q_C \tag{6.5}$$

Bitter's [82], [83] model is still one of the most complete models of erosion so far presented. However, the complexity of his equations prohibited their widespread use. Even more important, it contains a number of material-dependent constants such as: the deformation wear factor ϵ, cutting wear factor ϱ and the elastic limit Υ, which are not so easy to obtain.

6.2.3 Bergevin's Modification

Bergevin [84] suggested an approach that combined the simplicity of Finnie's [62] model and physical reality of Bitter's [82], [83] ideas. Like Bitter [82] he assumed that only the particles that have the normal impact velocity ($\vec{V}^p \sin\alpha$)

greater than some critical value, for the given material V_{cr}, create plastic deformation and erosion. Then he modified accordingly, Finnie's equations (6.2) by inserting $(\vec{V}^p \sin\alpha - V_{cr})$ instead of $\vec{V}^p \sin\alpha$.

for $\alpha \leq 18.5^o$

$$Q = \frac{m^p(\vec{V}^p \sin\alpha - V_{cr})}{2\sigma_o}\left[\vec{V}^p \cos\alpha - \frac{3}{2}(\vec{V}^p \sin\alpha - V_{cr})\right]$$

for $\alpha > 18.5^o$

$$Q = \frac{m^p(\vec{V}^p \sin\alpha - V_{cr})^2}{12\sigma_o}\frac{\cos^2\alpha}{\sin^2\alpha} \tag{6.6}$$

Here we have a set of relatively simple equations for cutting wear that take into account the elastic/plastic material behaviour. It would be theoretically appropriate to add to them the equations for deformation wear although the contribution of this mode of metal loss is usually small compared to the cutting mechanism.

Chapter 7

Predictions and Comparison with Experiments

As outlined in the literature survey, the body of work done in the area of flow–dependent corrosion did not offer any firm clues where exactly to search for connections between the flow and corrosion parameters. For single–phase flow a wide variety of propositions such as: breakaway velocity, critical Reynolds number, maximum shear stress and turbulence, were all in various studies related to onset of accelerated metal loss. In two–phase flow the picture was even more complicated as characterization of a liquid/solid flow with some universal parameter was next to impossible.

7.1 The Preliminary Study

In an attempt to resolve this problem before developing the full model of erosion-corrosion, as it was presented in previous chapters, a preliminary study was done where different flow parameters were compared with the erosion–corrosion parameters (Nešić and Postlethwaite [55]).

For comparison purposes an experimental investigation on the effect of wall geometry and resulting flow structure on erosion–corrosion was selected [60]. The form of the cell enabled two different geometries to be studied at the same time: a sudden constriction and a sudden expansion. The test cell was segmented in order to enable measurements of local weight loss. Some elements were electrically isolated for electrochemical measurements. To determine any effects of galvanic action between individual ring segments, local cell currents were measured and no significant galvanic effect was observed. The segmented test cell material was carbon steel (AISI MT - 1015). The test medium was 3 wt% $NaCl$ (technical grade in distilled water) with and without 2 vol% silica sand. The size distribution of sand particles was very narrow, with the average particle diameter of 430 μm. It has been found [85] that the size and the round shape of the particles are not noticeably affected during such experiments. Some of the important test conditions are listed in Table 7.1.

As no hydrodynamic experimental data were available, the flow was mod-

Table 7.1: Preliminary study test conditions

Velocity in the 42.5 mm pipe	3.3 m/s
Velocity in the 21.1 mm pipe	13.2 m/s
Reynolds number (42.5 mm)	170000
Reynolds number (21.1 mm)	340000
Average particle diameter	430μm
Particle concentration	0 and 2% (volume)
Temperature	$30°C$
Exposure time	up to $48h$
$NaCl$ concentration	$3wt\%$

elled with the two–phase flow model presented in Chapters 3 and 5. The wall function approach was used and no mass transfer (corrosion) or erosion computations were done at the time as these models were developed in later stages of the project.

7.1.1 Prediction Procedure

In order to cover the flow field, a computational grid 93×26 nodes was set up. Such a large number of computational points was a consequence of the long and narrow shape of the flow region (700×40 mm) and constraints related to suggested (reasonably small) control volume aspect ratio (1:10) and inter–

nodal distance expansion factor (1.25).

The criterion for convergence was the cumulative error over all the control volumes and was set to 0.1%. In the case of water flow the final solution was reached in about 700 iterations. In case of a 2% slurry flow, about 1100 iterations were needed to reach the converged solution. Numerical tests suggested that in order to get smooth convergence of the fluid flow equations and "stable" average particle parameters, 90 different starting locations and 2000 different particle trajectories had to be calculated, in every execution of the particle motion subroutine.

Since no fluid flow measurements were available, a fully developed turbulent flow velocity profile was assumed 12 diameters before the constriction. For the particles, a terminal velocity on the inlet was given. No particle turbulence was assumed at the inlet although numerical tests have shown that this condition, in our case, does not influence the results. A uniform particle size of 430 μm was used for predictions, thus neglecting the narrow particle size distribution present in the experiments.

7.1.2 Simulation vs. Experiments

Fluid flow results. Some of the most important features obtained by the simulations are given in Fig. 7.1–7.3. Predicted streamlines, representing the mean flow are shown, in the case of water flow (Fig. 7.1a) and 2% slurry flow

(Fig. 7.2a).

The streamlines show: (a) strong curvature of the flow in front of the constriction and associated with it a small recirculation eddy in the corner and (b) separation of the main flow stream at the expansion edge and reattachment further downstream resulting in a large recirculation zone in the corners.

Fig. 7.1b and Fig. 7.2b show the predicted field of turbulent fluctuations. Fluctuations are assumed isotropic and are calculated from the field of kinetic energy of turbulence. It is noticeable that the flow geometry creates two local sources of turbulence: one close to the constriction corner and a much larger one after the expansion. They are both a result of large gradients of mean velocity that exist at these points, causing significant shear stress and turbulence. In the case of slurry flow, the pattern of turbulent fluctuations (Fig. 7.2b) is similar to the one for water flow (Fig. 7.1b), except that the particles slightly distort the turbulence field by accepting some of the turbulence energy at peak points and redistributing it further downstream. This effect is not big due to the small particle volume concentration (2%) and small particle/fluid density ratio (2.65).

Single–phase flow erosion–corrosion. As we are primarily interested in the effect that the flow structure has on corrosion, it is important to determine the mean flow and turbulence parameters close to the walls, that are affecting the rate of oxygen-mass transfer controlled corrosion.

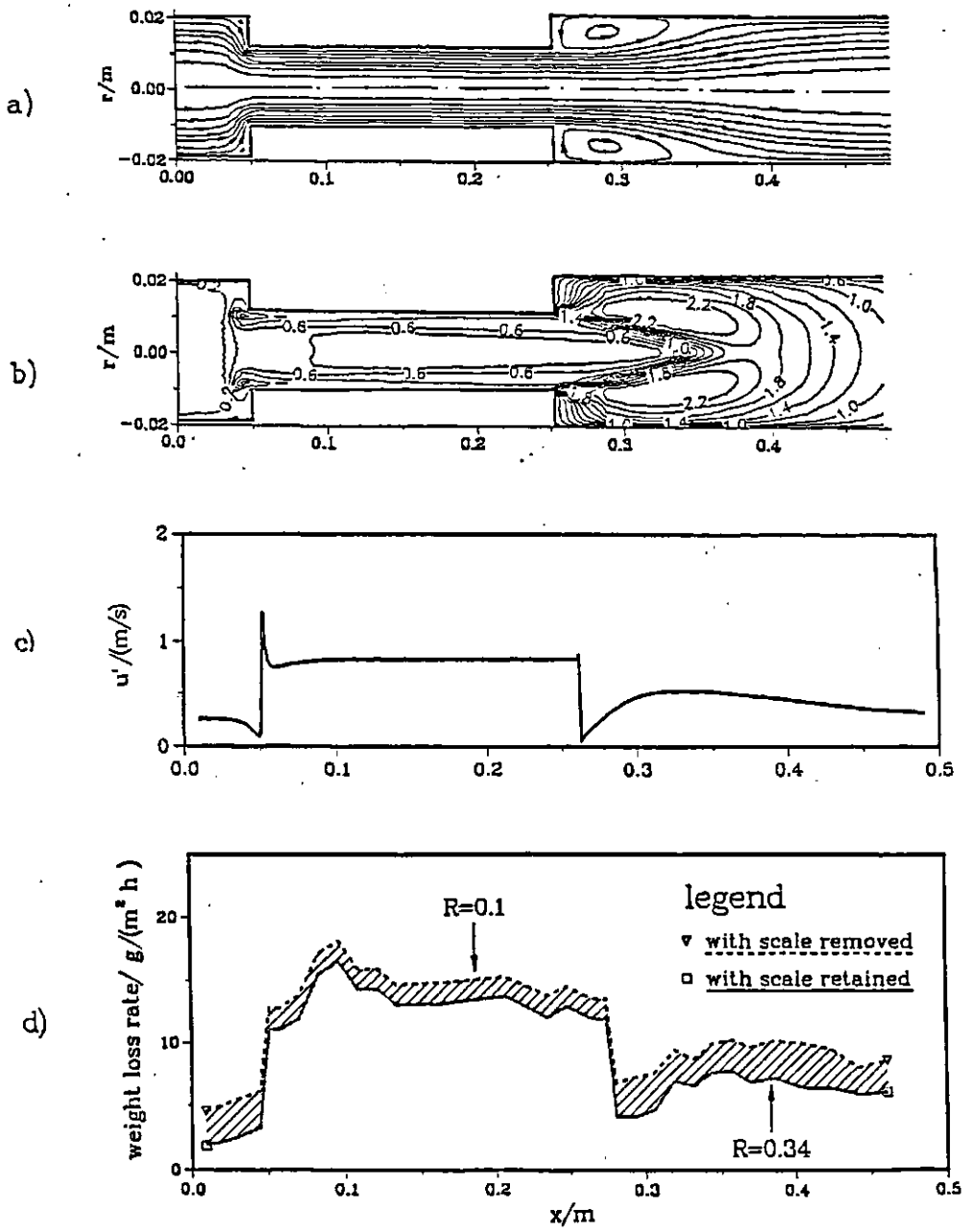

Figure 7.1: Water flow; $d_{small} = 21.1$ mm; $d_{large} = 42.5$ mm; $v_{small} = 13.2$ m/s; $v_{large} = 3.3$ m/s; Re_{large}=17.0×10^4; a) Predicted streamlines; b) Predicted turbulence field; c) Predicted near–wall turbulence (RMS); d) Measured weight loss by single–phase flow erosion–corrosion. Measurements taken from Lotz and Postlethwaite.

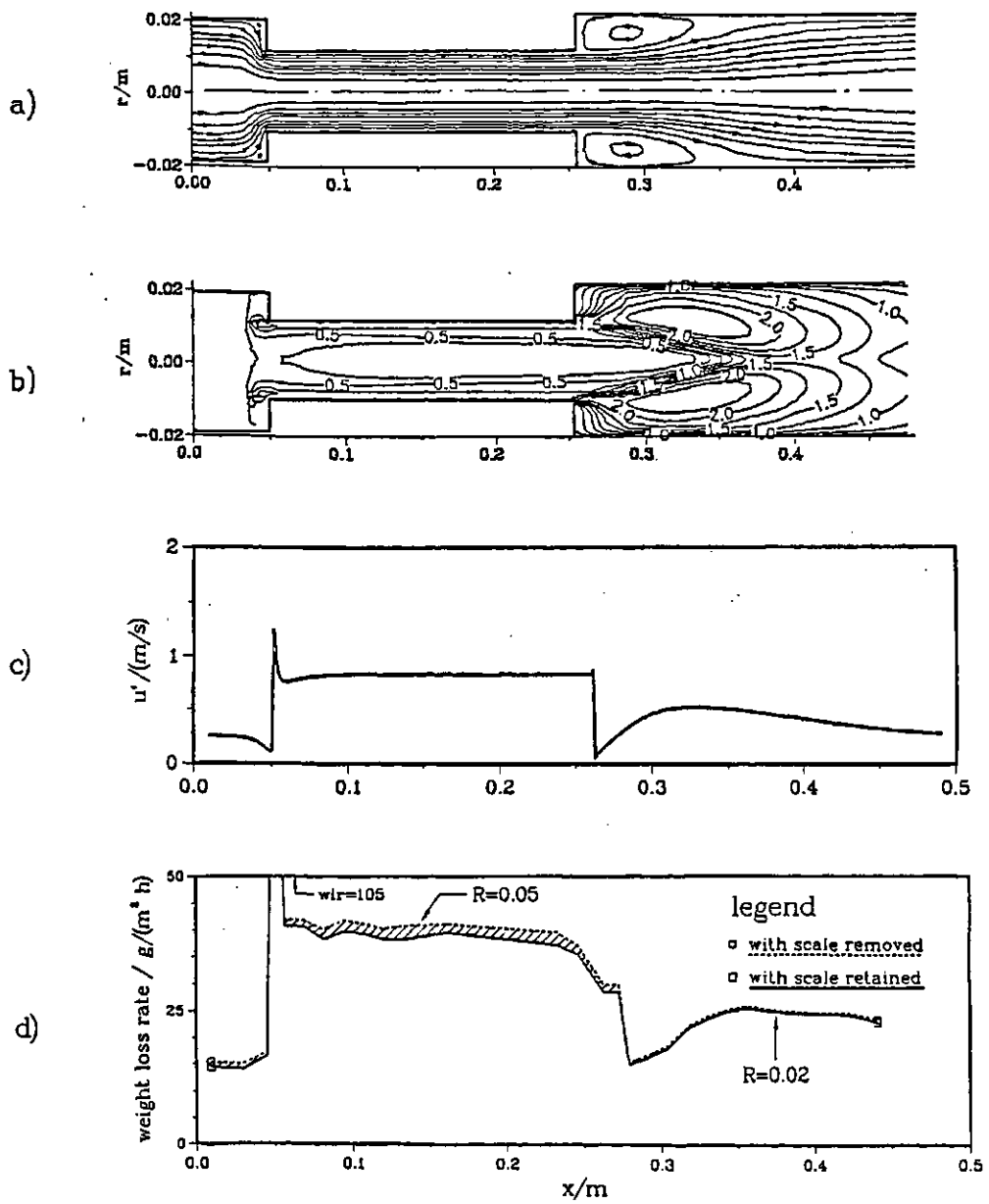

Figure 7.2: 2%vol Slurry flow; d_{small} = 21.1 mm; d_{large} = 42.5 mm; v_{small} = 13.2 m/s; v_{large} = 3.3 m/s Re_{large}=17.0×10^4. a) Predicted streamlines; b) Predicted turbulence field; c) Predicted near-wall turbulence (RMS); d) Measured weight loss by two-phase flow erosion-corrosion. Measurements taken from Lotz and Postlethwaite.

As it was indicated in the literature survey , it is quite clear that in case of disturbed flow, the mean velocity or a Reynolds number cannot be used as effective criteria to correlate mass transfer rates as it is impossible to select a universal velocity or a length scale as is done for simple geometries. However, for wall–shear stress this is not as obvious. Lately wall-shear stress has emerged in many studies as the prime candidate for correlating erosion–corrosion results. For our geometry, in Fig. 7.3 predicted variation of wall shear stress (Fig. 7.3b) along with the pattern of erosion–corrosion along the main pipe wall (Fig. 7.3c) are shown.

Predicted average levels of wall shear stress $50 - 300$ Pa are according to Efird [51], within the range of critical shear stresses needed for removal of protective films for copper based alloys in sea water. The pattern of wall shear stress is similar to the pattern of erosion–corrosion, except for the region after the expansion. According to the wall shear stress pattern, there should be a minimum of the corrosion rate somewhere close to the reattachment point ($x \approx 0.37$ m, where the shear stress is zero), but the measured rate of metal loss indicates actually the opposite: there is a local maximum in this region. This suggested that there is some other factor governing the enhanced rate of mass transfer controlled corrosion.

Fig. 7.1c shows predicted near–wall turbulence expressed in terms of turbulent fluctuations. When compared to the rates of metal loss measured in the

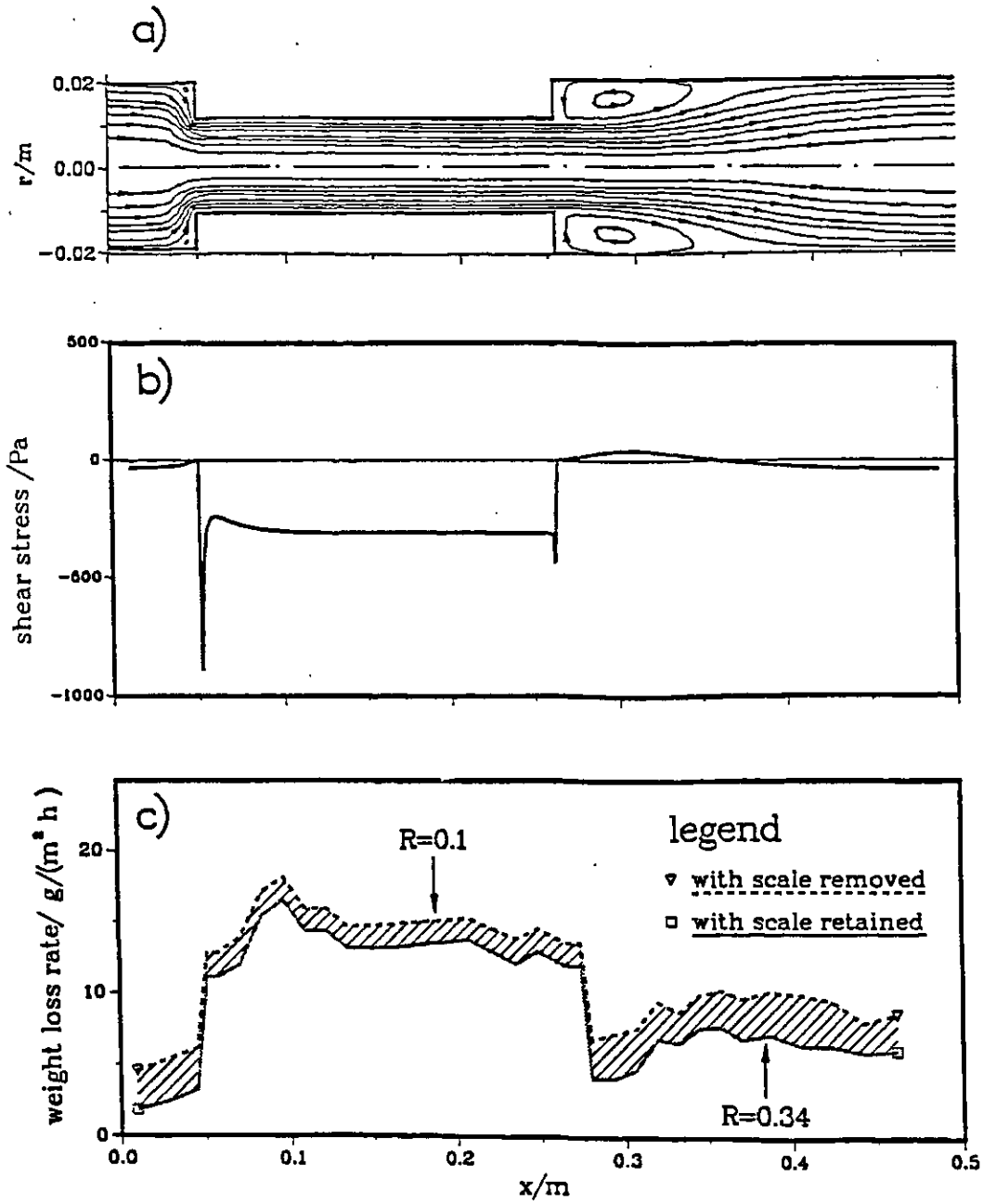

Figure 7.3: Water flow; $d_{small} = 21.1$ mm; $d_{large} = 42.5$ mm; $v_{small} = 13.2$ m/s; $v_{large} = 3.3$ m/s; Re_{large}=17.0×10^4. a) Predicted streamlines; b) Predicted shear stress along main pipe wall; c) Measured weight loss by single–phase flow erosion–corrosion. Measurements taken from Lotz and Postlethwaite.

segmented cell specimen (Fig. 7.1d) the overall similarities in profile shape are obvious including the region after the expansion. This suggested that *near–wall turbulence can be used as an effective criterion to be correlated with rates of mass transfer*, which is in agreement with the experimental findings of Blatt et al. [44].

It is now easy to explain why in cases of straight pipe flow or rotating cylinders values of shear stress can correlate the mass transfer rates. In those simple flow geometries the patterns of wall shear stress were the same as patterns of near–wall turbulence, because wall shear stress was the main generator of turbulence. The same argument can be used for the straight parts of the pipe in the present experimental results. But when there is separation and reattachment of flow there are other sources of turbulence such as: large gradients in the mean axial velocity in the bulk fluid after the expansion (Fig. 7.1b). In these cases the near–wall profiles of turbulence and shear stress do not have to correspond. Formed turbulent eddies are transported by convection from the regions where they form and if they reach the walls they alter the near–wall turbulent profile. Thus a local maximum of turbulence close to the wall after the expansion (Fig. 7.1c, $x \approx 0.33$ m) is a reflection of the overall maximum of turbulence in the bulk close by (Fig. 7.1b).

Fig. 7.1c shows the predicted peak of turbulence close to the constriction edge which was not recorded in the experiments as a peak in metal loss, but

low resolution and accuracy of measurements in this region prevents us from drawing any further conclusions. A much shorter specimen should be used at the leading edge of the constriction in future experiments.

The question to be answered now is: how does turbulence enhance local rates of mass transfer controlled corrosion? As a first approximation we can assume that the rate of mass transfer is controlled by the resistance in the protective corrosion film on the metal surface and the resistance in the boundary layer. Shemilt et al. [48] have found that the mass transfer coefficient in the boundary layer ("damped turbulence layer") controls the overall mass transfer rate. Lotz and Postlethwaite [60] in their experimental study have found the opposite: that the coefficient for mass transfer in the protective corrosion layer is much higher than the one for the boundary layer. Hence intensive turbulence close to the wall probably affects both: disturbs the mass transfer boundary layer, and thins the protective corrosion layer, but to what extent one of these two mechanisms is governing the overall mass transfer rate, was unclear at that point and needed further research.

Fig. 7.1d shows the amount of scale retained in the experiments, (as the shaded area), suggesting that actually the protective corrosion products were only partially removed from the metal surface by intensive turbulent fluctuations near the wall, to enable higher oxygen transfer rates to the surface and higher levels of corrosion. The scale retention ratio **R** is defined as:

$$\mathbf{R} = \frac{local\ mass\ of\ scale}{local\ metal\ mass\ loss} \tag{7.1}$$

with $\mathbf{R} = 1.59$ if all $Fe_2O_3 \cdot 3H_2O$ (red rust on iron) is retained on the surface.

Two-phase flow erosion-corrosion. For 2% slurry flow the profile of near–wall turbulence (Fig. 7.2c) differs very little from the one for water flow (Fig. 7.1c). Again it has a similar character as the erosion–corrosion profile recorded in the experiments with 2% slurry flow (Fig. 7.2d). But it is important to notice that the whole erosion–corrosion profile for slurry flow (Fig. 7.2d) has been elevated compared to the erosion–corrosion profile for water flow (Fig. 7.1d), while the predicted turbulence profile remained nearly unchanged. This suggests that particles have some other effect on accelerating metal loss other than altering the turbulence field. The high rate of metal loss at the front facing constriction wall and the very small amount of scale retained (Fig. 7.2d), suggest that *particle–wall impacts (erosion) are the important factor which causes further thinning of the protective layer on the surface* and even erosion of the base metal itself. Thus predicted particle–wall impact *statistics* (mean local values of impact frequency, velocity and angle, obtained from averaging over the large number of particle trajectories), were analyzed in an attempt to explain noticed differences. The predictions have indicated significant particle–wall impact rates only in the regions of strong curvature of the flow: at the

constriction and after the expansion. Predicted frequency of particle–wall impacts at the front facing constriction wall was about 200 /(mm^2 s) while downstream of the constriction it was an order of magnitude lower (5-20 /(mm^2 s)) The average particle impact velocities perpendicular to the wall were in the range of 0.2-1.1 m/s while the the average angles of impact varied from $10°-80°$ on the front facing wall and $0°-40°$ degrees after the expansion. These results explain the large peak in metal loss at the front facing constriction wall and the higher erosion–corrosion rates downstream from the expansion.

7.1.3 Conclusions

In this preliminary study it was shown that:

1. In order to predict rates of erosion–corrosion for the case of disturbed single or two-phase flow, it is necessary to determine the local, near–wall structure of the flow and particle–wall impact statistics. Knowledge of overall hydrodynamic and/or geometrical parameters is not sufficient. Thus, simulation of the flow structure is the right way to resolve this problem.

2. In disturbed flow, wall shear stress is not the governing factor for mass transfer controlled corrosion, but rather it is the local near–wall turbulence. In case of straight pipe flow the two coincide.

3. In case of single-phase flow, comparisons revealed a significant effect of local near–wall turbulence on corrosion rate of the base metal. It has been hypothesized that intensive near–wall turbulence contributed to disrupting the protective corrosion layer and disturbed the mass transfer boundary layer, thus enhancing oxygen transport and metal loss by corrosion.

4. In case of two-phase flow, maximum metal loss coincided with local maximums of particle–wall mean impact frequency (front facing wall and downstream from the expansion). A similar pattern of metal loss was observed as in case of single-phase flow, but at a higher level. Similarity of the pattern has been attributed partially to the pattern of turbulence that is only slightly different in case of 2% slurry flow compared to water flow. Large rates of metal loss at the front facing wall and overall higher level of erosion–corrosion have been assumed to be the consequence of particle–wall impacts.

This preliminary study also indicated some of the problems that needed further research:

- Fluid flow part of the model needed further development especially in the region near the walls where the wall function approach was used. This might lead into development of mass-transfer models that can be used to predict corrosion rates.

- The accuracy of the hydrodynamic model and the model for particle dispersion in the turbulent flow field had to be tested further.
- Quantification of the effect of near–wall turbulence and particle impacts had to be developed.

The first thing that was done was development and verification of different components of the overall erosion–corrosion model. As the fluid flow model is in many ways a base for all other models, the first step was to verify the flow model. Then the mass–transfer–controlled corrosion model had to be tested. Finally the particle motion model and the erosion model were tested. Only when every component of the model was tested separately was the overall model used for predictions.

7.2 Hydrodynamic Results

Flow through a sudden pipe expansion was chosen as a generic test case, to study the relationship between the hydrodynamic parameters of the flow and mass transfer controlled erosion–corrosion in disturbed flow conditions. This geometry, extensively studied in fluid dynamics, has a high level of hydrodynamic complexity with separation, reattachment and associated recirculation of the flow, which in turn have a significant effect on a large number of heat and mass transfer devices and processes. The sudden change of pipe diameter is the

most frequently encountered flow disturbance that has been associated with severe erosion–corrosion problems in practice (e.g. valves, fittings, grooves, weld beads).

For verification of our hydrodynamic model we have selected the measurements of Blatt et al. [44]. They have reported the LDV measurements for both single– and two–phase flow at the axis and in the near wall region, as well as erosion–corrosion measurements for flow through a sudden expansion. Also, recent LDV measurements of Stieglmeier et al. [18] were used as they provided very detailed measurements of mean and fluctuating velocity profiles.

Parameters for both test cases, relevant for this study, are given in Table 7.2. Some of the more important parameters of the numerical method used, like grid configuration, number of nodes, solution criteria, are also included. To simulate experimental results of Blatt et al. [44] the wall function approach was used to model flow near the solid boundaries. The experiments of Stieglmeier et al. [18] were simulated by using both the wall function and low Reynolds number approach.

7.2.1 Measurements of Blatt et al.

Blatt et al. [44] have reported axial profiles of the axial velocity at the centreline, as well as axial, radial and fluctuating velocity 2 mm from the wall. The comparison of the simulation and the measurements for the axial veloc-

Table 7.2: Test cases for the model of hydrodynamics – important geometric, hydrodynamic and numerical parameters

	Blatt et al.	Stieglmeier et al. (LRN)
Inlet diameter (mm)	26	50
Outlet diameter (mm)	40	80
Length (mm)	420	400
Inlet velocity (m/s)	1.14	2.51
Outlet velocity (m/s)	0.48	0.98
Inlet Reynolds number	37000	21000
Outlet Reynolds number	24000	15600
Number of x grid points	48	82
Number of y grid points	12	30
Number of iterations	252	983
Total error of prediction (%)	0.1	0.1
VAX 6320 CPU time (min)	2.12	71

ities, at the centreline and 2 mm from the wall are shown in Fig. 7.4a. The character of the curve for decay of the axial centreline velocity is captured by the predictions, although a discrepancy up to 10% exists in the first part of the calculated domain. This may be due to the inaccurately defined flow parameters at the entrance of the flow domain in the original paper, and/or due to the faster spreading of the confined jet in the predictions. This problem is also found with other $k-\epsilon$/wall–function models (Yap [12]).

The region close to the wall is of particular interest in this study, and Fig. 7.4b shows comparisons of predictions and measurements of the radial velocity components for the same geometry 2 mm from the wall. As the typical measuring volume for LDV is of the order of 1 mm, and the gradients in the near–wall region are large, predictions are shown as the shaded area, with the limits corresponding to predictions at 1.5 mm and 2.5 mm from the wall. The predicted profile of the fluctuation velocity shows a good agreement with the measured values, taking into account that the predictions show a space–averaged value while the measurements present the radial component of the fluctuating velocity near the wall. This explains different asymptotic values for the fluctuations further downstream, given by the predictions and the experiments. The predicted value is higher, as it is known that near the wall, the axial component of the fluctuating velocity is larger than the radial, so the space–averaged predicted value is expected to be larger than the mea-

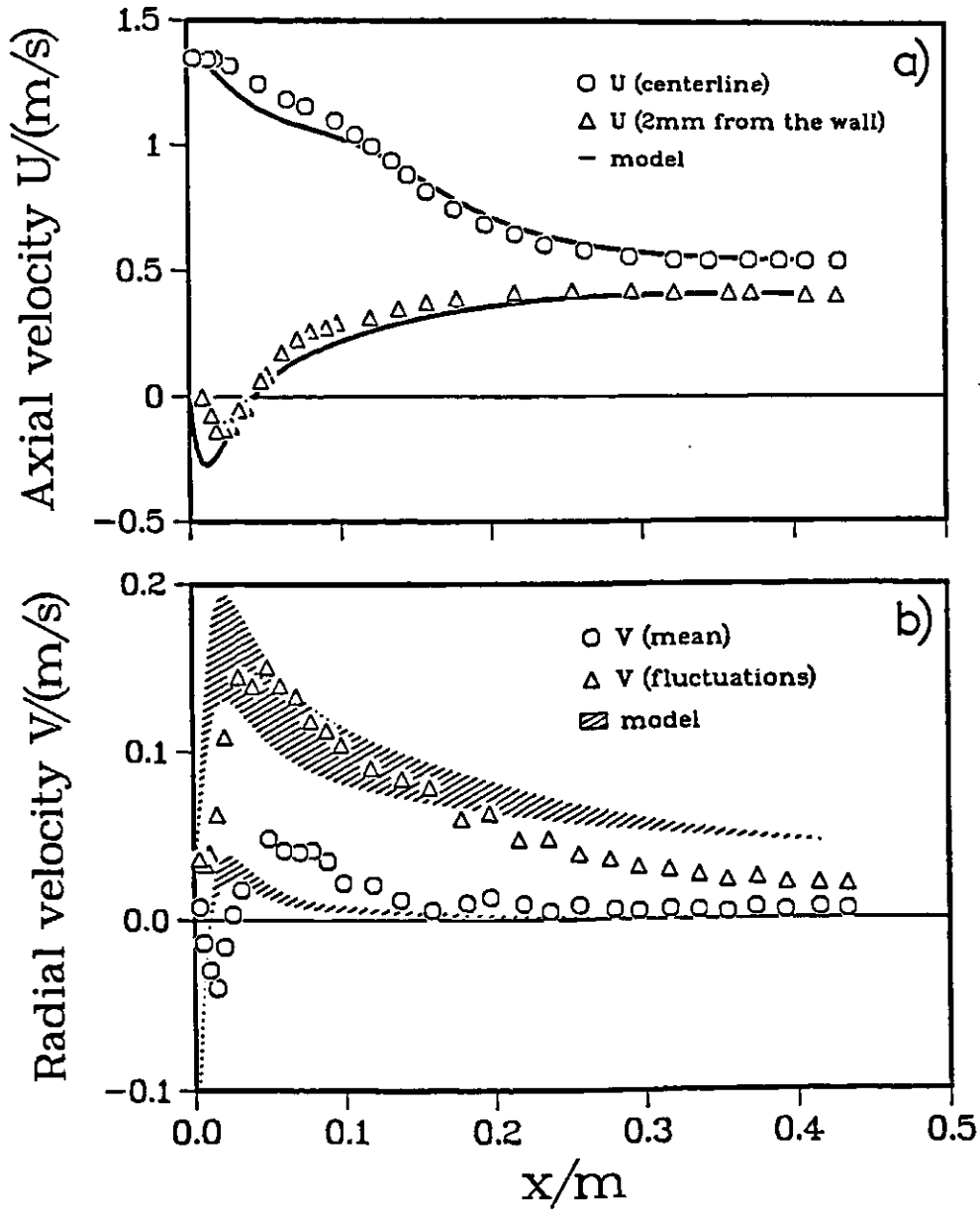

Figure 7.4: Water flow through a sudden pipe expansion; d_{in} = 26.0 mm; d_{out} = 40.0 mm; v_{in} = 1.14 m/s; v_{out} = 0.48 m/s; Re_{out}=2.4×10^4. a) Predictions and measurements of the mean axial fluid velocity; b) Predictions and measurements for the mean and fluctuating component of the radial fluid velocity, 2 mm from the wall. Measurements taken from Blatt et al.

sured radial component. Predictions of mean radial velocity show moderate agreement with the experiments. The maxima of both predicted curves are located somewhat before the measured values in the axial direction, which corresponds to the predicted faster spreading of the jet. In general, simulation of the hydrodynamic parameters for this test case have shown reasonable agreement with the measured values

7.2.2 Measurements of Stieglmeier et al.

Recent results of Stieglmeier et al. [18] were selected for additional validation of our flow model as they reported detailed radial profiles for axial, radial and tangential mean velocity, as well as the normal and shear turbulent stresses and the reattachment length. The profiles were shown for six locations downstream of the sudden expansion and measurements were taken as close as 1 mm from the wall. Their results can be considered as a benchmark for validation of computational models.

Simulations were done[1] by using first the WF model and then the LRN model for the boundary conditions (both described in Section 3.5). This was done to enable estimation of the benefits of the LRN number over WF model since the LRN model requires significantly more computational computer time and memory for the same simulated flow geometry.

[1]Simulations for this particular test case were done with the assistance of a fellow graduate student George Adamopoulos.

The profiles of mean axial velocity are shown in Fig. 7.5. It is clear that both models performed very well with the maximum discrepancy being less than 5 %. The LRN model gave somewhat better results in the near–wall region especially before the reattachment point ($x = 40$ mm). This could be anticipated as the universal velocity profile used in WF functions cannot be expected to be valid near the reattachment point. On the other hand in the redeveloped flow region ($x = 200$ mm) near the centreline the WF performed slightly better. Overall, the agreement for the mean axial velocity profiles can be considered very good for both models as the maximum discrepancy between the predictions and the measurements being less than 5 % is within the maximum overall error of measurement as reported by Stieglmeier et al. [18].

The radial velocity profiles are shown in Fig. 7.6. The LRN model performed consistently better than the WF model although the discrepancy between the predictions and measurements was larger than for the axial velocity. This is particularly obvious in the profile ($x = 40$ mm). The predicted velocities are consistently higher then measurements and there are no negative values. This means that the shape of the recirculating region is not accurately predicted. However, the measured negative radial velocities near and at the axis are open to suspicion ($x = 40$, $x = 200$ mm). Similar problems in predicting the radial velocity profiles especially in the recirculation region

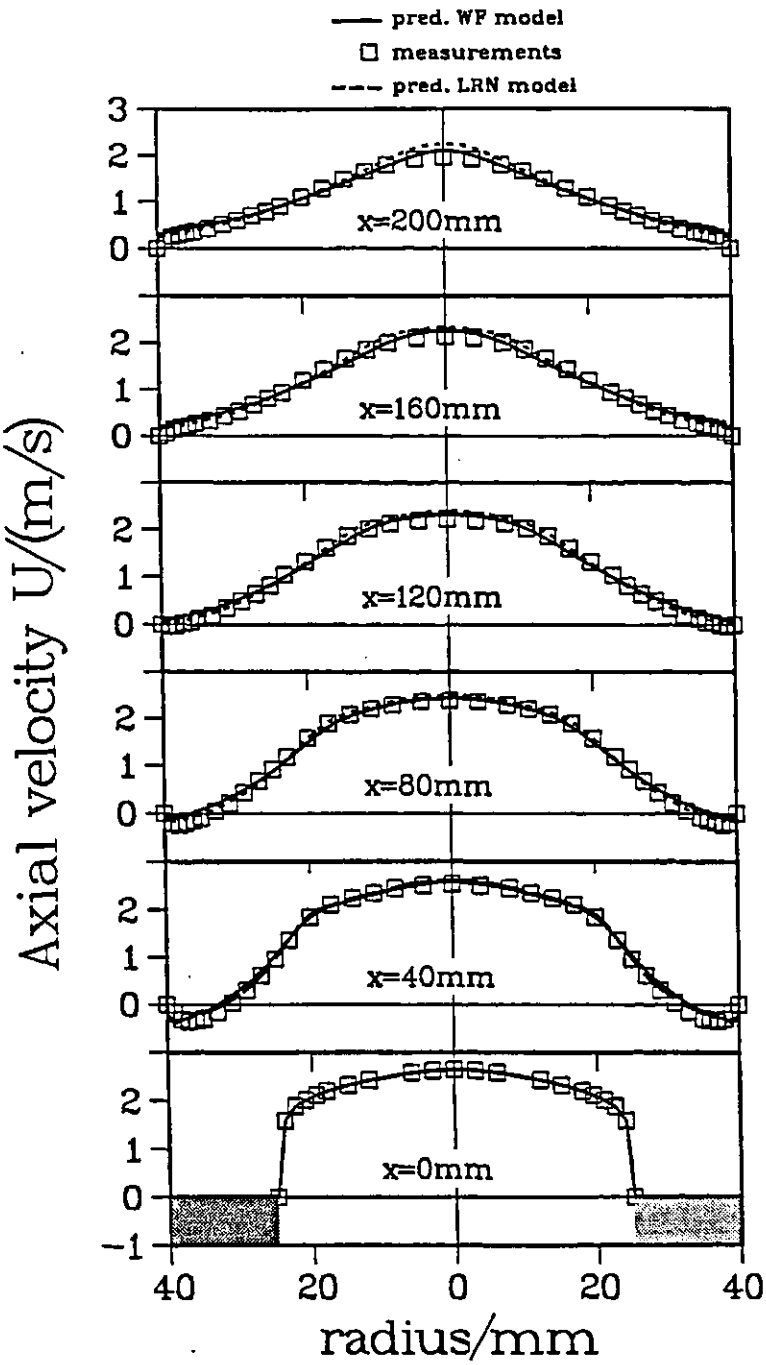

Figure 7.5: Flow through a sudden pipe expansion; d_{in} = 50.0 mm; d_{out} = 80.0 mm; v_{in} = 2.51 m/s; v_{out} = 0.98 m/s; Re = 1.56 x 10^4. Predictions and measurements of the radial profiles of mean axial velocity. Measurements taken from Stieglmeier et al.

were encountered by other researchers [57], [17] and this is probably related to inadequate modelling of turbulent transport in this region. Apart from the first profile ($x = 40$ mm) it can be concluded that the inaccuracy of the predictions was not much larger then the scattering of the measured values for radial velocity.

Stieglmeier et al. [18] measured all three components of the normal turbulent stress (u^2, v^2, w^2). However, in our $k - \epsilon$ model isotropic turbulence is assumed. For comparison purposes the kinetic energy of turbulence k was computed from the measured values of normal turbulent stresses by a formula: $k = \frac{1}{2}(u^2 + v^2 + w^2)$. Keeping this simplification in mind predictions of kinetic energy of turbulence k shown in Fig. 7.7 are in good agreement with the measured values. Overall, both models performed reasonably well, with the LRN model being significantly better in the near–wall region of the recirculation region ($x = 40$ mm). In this region the WF model predicted twice the measured value of k while the LRN model overpredicted turbulence by some 30–50 %. Further, downstream both models were closer to measured values (within 10 %), except at the axis where somewhat larger discrepancy can be attributed to the inaccuracy of the inlet condition for k.

The measured reattachment length ($x_r \approx 140$ mm) was underpredicted by both models (WF: $x_r \approx 100$ mm; LRN: $x_r \approx 120$ mm). Overall, it can be concluded that both models performed reasonably well in predicting the

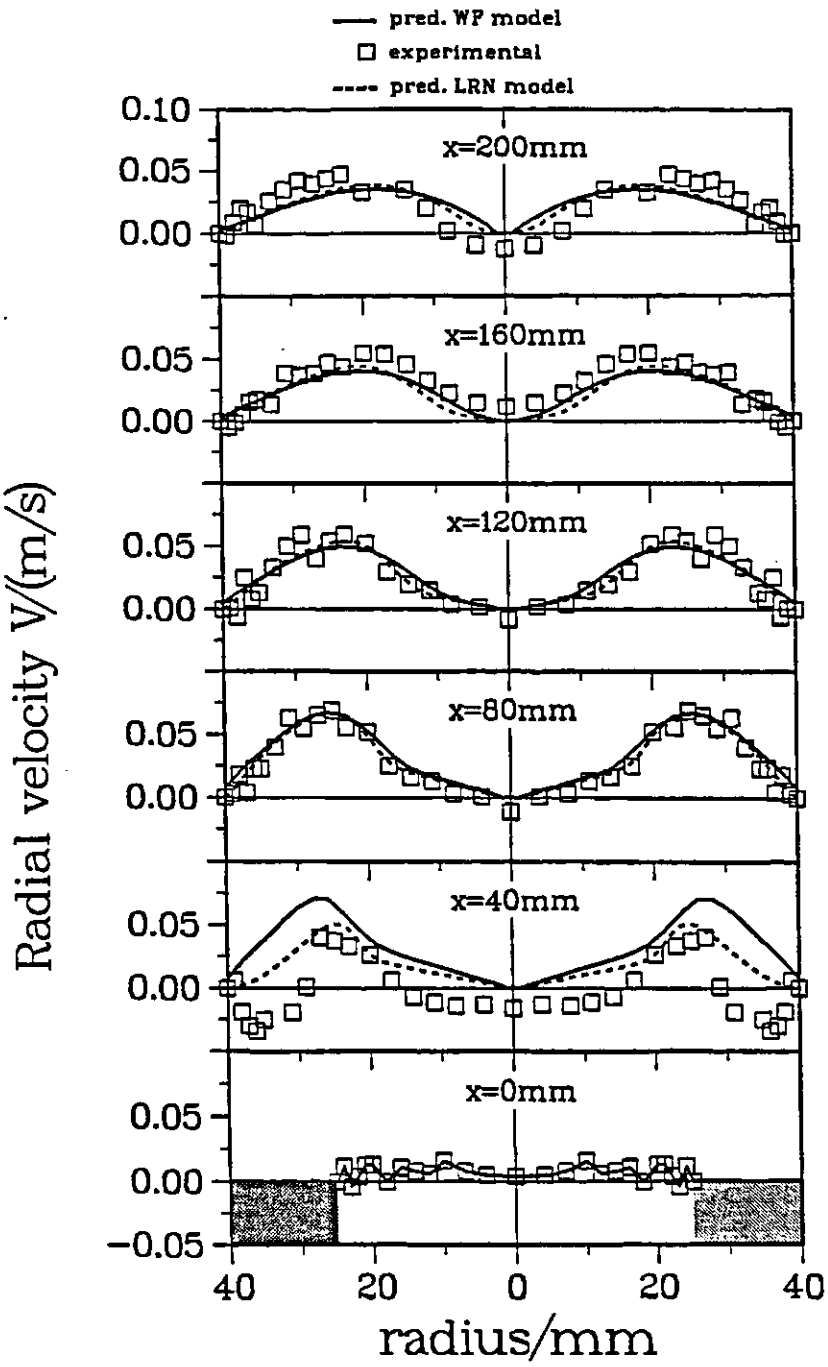

Figure 7.6: Flow through a sudden pipe expansion; d_{in} = 50.0 mm; d_{out} = 80.0 mm; v_{in} = 2.51 m/s; v_{out} = 0.98 m/s; Re = 1.56 x 10^4. Predictions and measurements of the radial profiles of mean radial velocity. Measurements taken from Stieglmeier et al.

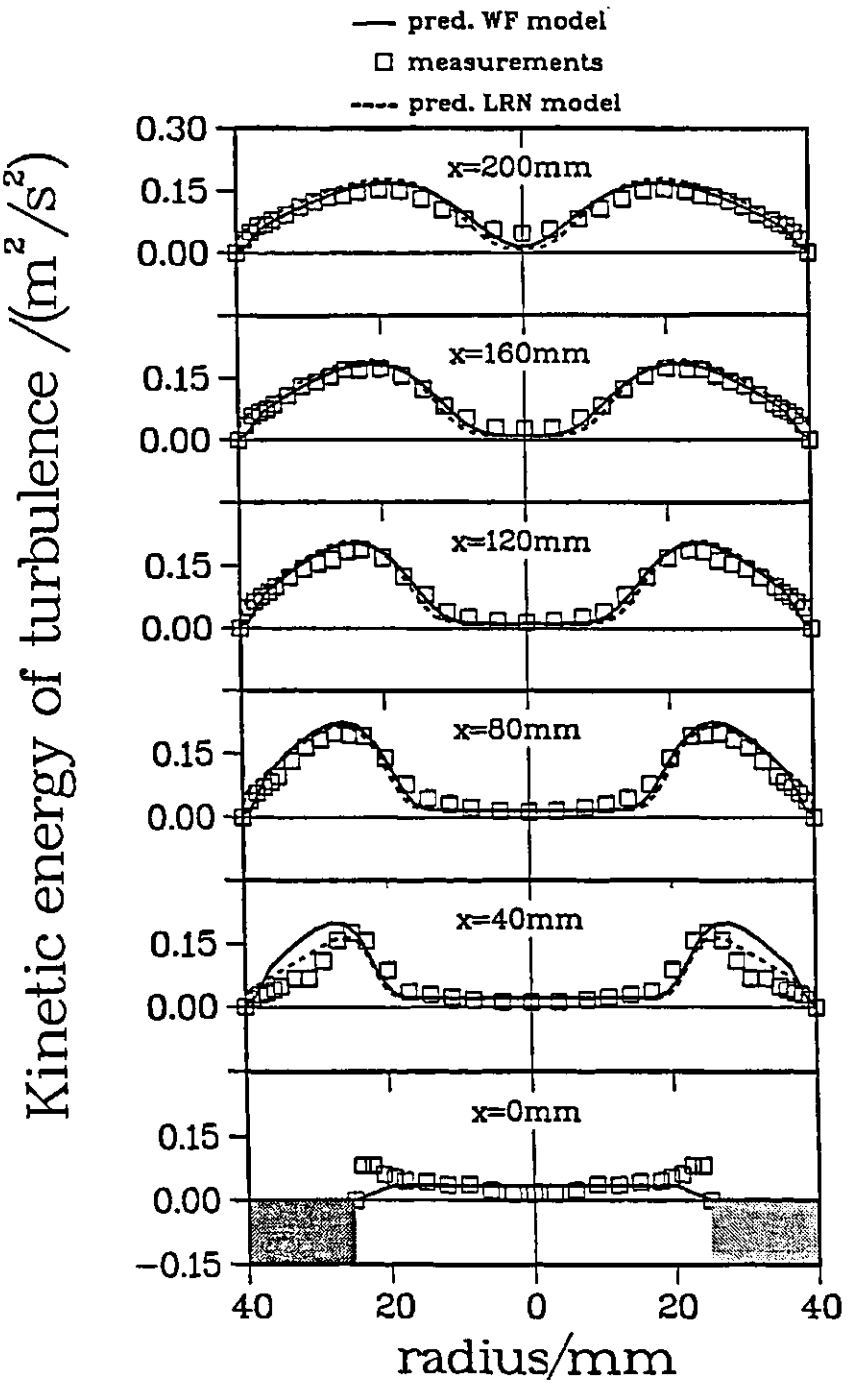

Figure 7.7: Flow through a sudden pipe expansion; d_{in} = 50.0 mm; d_{out} = 80.0 mm; v_{in} = 2.51 m/s; v_{out} = 0.98 m/s; Re = 1.56 × 10^4. Predictions and measurements of the radial profiles of kinetic energy of turbulence. Measurements taken from Stieglmeier et al.

flow through a sudden expansion. The largest discrepancies were found in the recirculation region where the model of turbulence is inappropriate. The LRN model performed somewhat better in this region especially near the wall. From an engineering point of view the large increase in computing time and storage required for the LRN model is not warranted by a significantly better performance. However, this is true only for the hydrodynamic parameters, while for mass transfer it is not the case as will be shown in the following section.

7.3 Corrosion Results

Since the test of the hydrodynamic model gave encouraging results the next component of the overall model to be tested was the corrosion model. Let us recall that the corrosion model applies to mass–transfer–controlled corrosion and that our corrosion rates are obtained from the wall–mass–transfer rates. Thus to test the corrosion model we have simulated the effect of disturbed flow on the mass transfer to the wall. The experimental study of Sydberger and Lotz [47], on the effect of separated, turbulent, aqueous flow on wall-mass transfer rates, was numerically simulated. They used electrochemical measurements to determine wall-mass transfer rates for a system with a Schmidt number of 1460. Among the variety of geometries that they investigated, we

have selected the sudden pipe expansion flow geometry. The numerical parameters, as well as the geometrical and hydrodynamical parameters of the flows simulated, are given in Table 7.3.

7.3.1 First Attempt – Correlation

As the preliminary study has indicated, in case of single–phase flow there appeared to be a definite connection between near wall turbulence levels and rates of mass-transfer–controlled erosion–corrosion. This correlation needed to be investigated in more detail.

Initially, turbulent mass transport in the flow domain has not been directly modelled. The reasons is that the Schmidt number in liquid systems is of the order $10^2 - 10^3$ and consequently the mass transfer boundary layer is much thinner than the viscous sublayer. Application of wall functions for mass transfer is then not suitable as a much finer mesh, that goes closer to the wall than the one used for hydrodynamics, would be required. Thus the mass transfer could not be modelled by using the WF approach. However, WF approach initially developed (Nešić and Postlethwaite [86]) could give us more information on the relationship between the near–wall turbulence and mass transfer.

The flow geometry and predicted streamlines, with the recirculation region are shown in Fig. 7.8a. The measured increase in mass transfer coefficient

Table 7.3: Test cases for the mass transfer model – important geometric, hydrodynamic and numerical parameters

Outlet Reynolds number	21000	42000	84000	130000
Inlet diameter/mm	20	20	20	20
Outlet diameter/mm	40	40	40	40
Length/mm	400	400	400	400
Inlet velocity/m/s	1.71	3.38	6.75	10.45
Outlet velocity/m/s	0.42	0.84	1.68	2.62
Number of x grid-points	80	81	83	86
Number of y grid-points	26	28	29	30
Last grid-point wall distance (μm)	5	3	2	1
Number of iterations	757	870	863	1146
VAX 6320 CPU time/min	62	82	89	117
Total error of prediction/%	0.1	0.1	0.1	0.1

downstream from the expansion for Re=84000 is shown in Fig. 7.8b. Since there were no surface films, this increase is a result of smaller effective thickness of the mass transfer boundary layer, caused by increased turbulent transport in this region. Predictions show that the shape of the curve and its maximum qualitatively coincide with the predicted profile of turbulence near the wall (Fig. 7.8b). Identical conclusions were reached when flow at Reynolds numbers of 21000, 42000 and 130000 was simulated. Thus increased turbulence caused by separation and reattachment of the flow, creates turbulent eddies that reach very close to the wall, increasing the rate of wall–mass transfer.

To see if a general effect of turbulence on mass transfer can be detected over this wide range of Reynolds numbers, measured Sherwood numbers were plotted against predicted near–wall turbulence velocity fluctuations in Fig. 7.9. In this correlation the values of the velocity fluctuations at the node closest to the wall, which is in the law–of–the–wall region, were used. The Sherwood number was divided by the $Sc^{0.33}$ for generality. The very pronounced correlation obtained suggests that rates of mass transfer are directly related to the levels of turbulence near the wall, and can be predicted by using the present flow model. Open symbols that do not follow the general correlation are typical for the region before the reattachment, where the model of turbulence used is strictly not correct.

The correlation obtained could be used as a predictive tool. It is sufficient

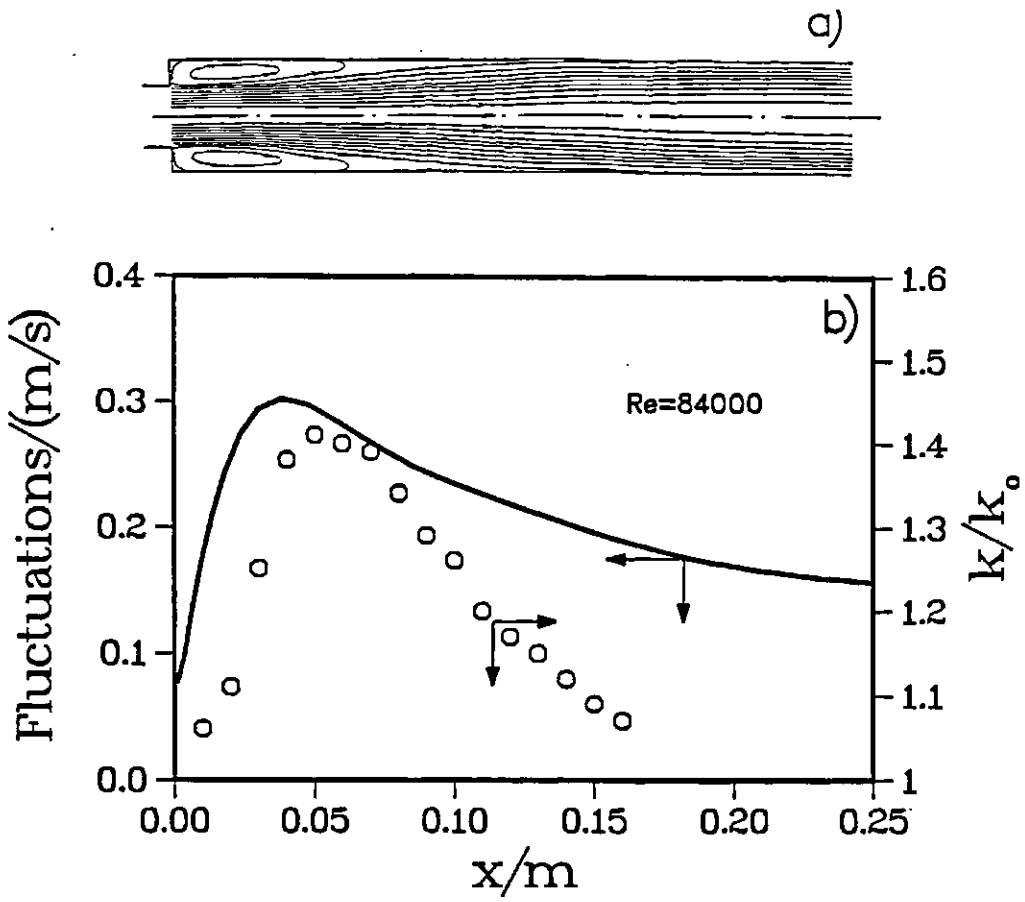

Figure 7.8: Water flow through a sudden pipe expansion; d_{in} = 20.0 mm; d_{out} = 40.0 mm; v_{in} = 6.75 m/s; v_{out} = 1.68 m/s; Re_{out} = 8.4 x 10^4. a) Predicted fluid flow streamlines; b) Profiles of measured increase in the mass transfer coefficient (Sydberger and Lotz) and predicted near-wall turbulence.

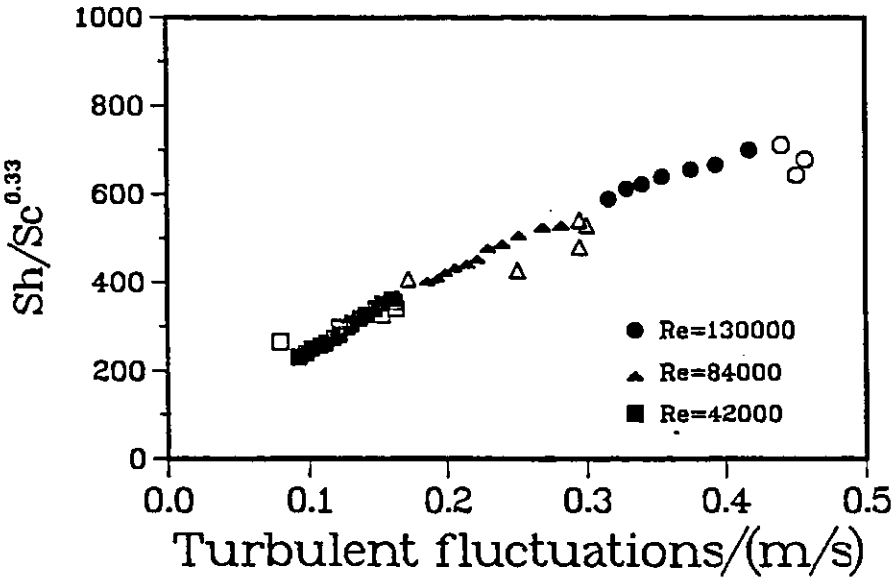

Figure 7.9: Measured Sherwood number (Sydberger and Lotz) vs. predicted turbulent fluctuations in the law–of–the–wall region.

to use the flow model to predict the mean flow and turbulence field. Then use the predicted values for the turbulent fluctuations in the law–of–the–wall region along with the correlation on Fig. 7.9 to obtain rates of local wall-mass transfer. Converting these into corrosion rates is straightforward.

7.3.2 The Full Predictive Model

The correlation obtained from this set of experimental results (Fig. 7.9), was successfully used to predict the measured corrosion rates of Lotz and Postlethwaite [60] (flow geometry described in Section 7.1). Although the specific results obtained appeared encouraging (Nešić and Postlethwaite [87]), there was some concern regarding the generality of the hydrodynamic model and the

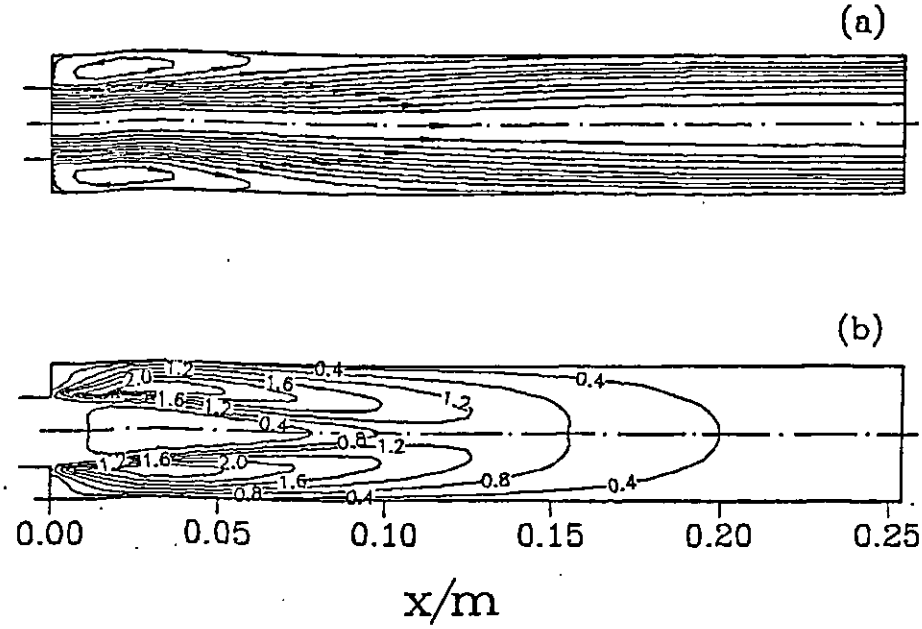

Figure 7.10: Water flow through a sudden pipe expansion; $d_{in} = 20.0$ mm; $d_{out} = 40.0$ mm; $v_{in} = 1.71$ m/s; $v_{out} = 0.42$ m/s; $Re_{out} = 2.1 \times 10^4$. Predictions for the (a) flow streamlines; (b) corresponding turbulence kinetic energy field.

correlation obtained. In an attempt to obtain a more general model for prediction of wall-mass transfer rates in separated flow, the hydrodynamic code was revised to include a low Reynolds number (LRN) $k - \epsilon$ model (Nešić and Postlethwaite [88]). Unlike the WF approach, a LRN closure attempts to model the turbulent transport across the entire near-wall region. This is especially important for predicting mass transfer at the wall. The following predictions were made with the LRN model for the boundary conditions.

Predictions for the flow streamlines and the corresponding turbulence kinetic energy field, are shown in Fig. 7.10 for the Reynolds number $Re = 2.1 \times 10^4$.

From the turbulence kinetic energy field (Fig. 7.10b), the major source of turbulence can be clearly identified downstream of the expansion in the

bulk flow at the point of maximum shear. The turbulence thus created is transported by convection and reaches the proximity of the wall, creating a local maximum in near wall turbulence in the region near the reattachment point.

Fig. 7.11–7.14 compare the measured and predicted wall–mass transfer rates expressed in terms of the local mass transfer coefficient[2], for four different Reynolds numbers. The predicted profiles follow the shape of the measured curves.

The discrepancy is largest for the highest Reynolds numbers, where the smallest effect of separated flow conditions is expected. Furthermore, the predictions are closer to the measured values in the region after the reattachment. This can be explained by the fact that the model of turbulence adopted is not strictly valid in the recirculation zone of the flow. Both the measured and predicted profiles far downstream asymptotically approach the value obtained from the widely accepted straight pipe mass–transfer correlation of Berger and Hau [89]. When the higher value of the turbulent Schmidt number was used in the predictions for the viscous sublayer, $\sigma_m = 1.7$ [77], the maximum discrepancy between the measured and predicted values in the region after the reattachment was reduced from 80% to 10%, while the discrepancy for

[2]Predicted local wall–mass fluxes were converted into the local mass transfer coefficients based on the overall concentration difference between the bulk solution and the wall.

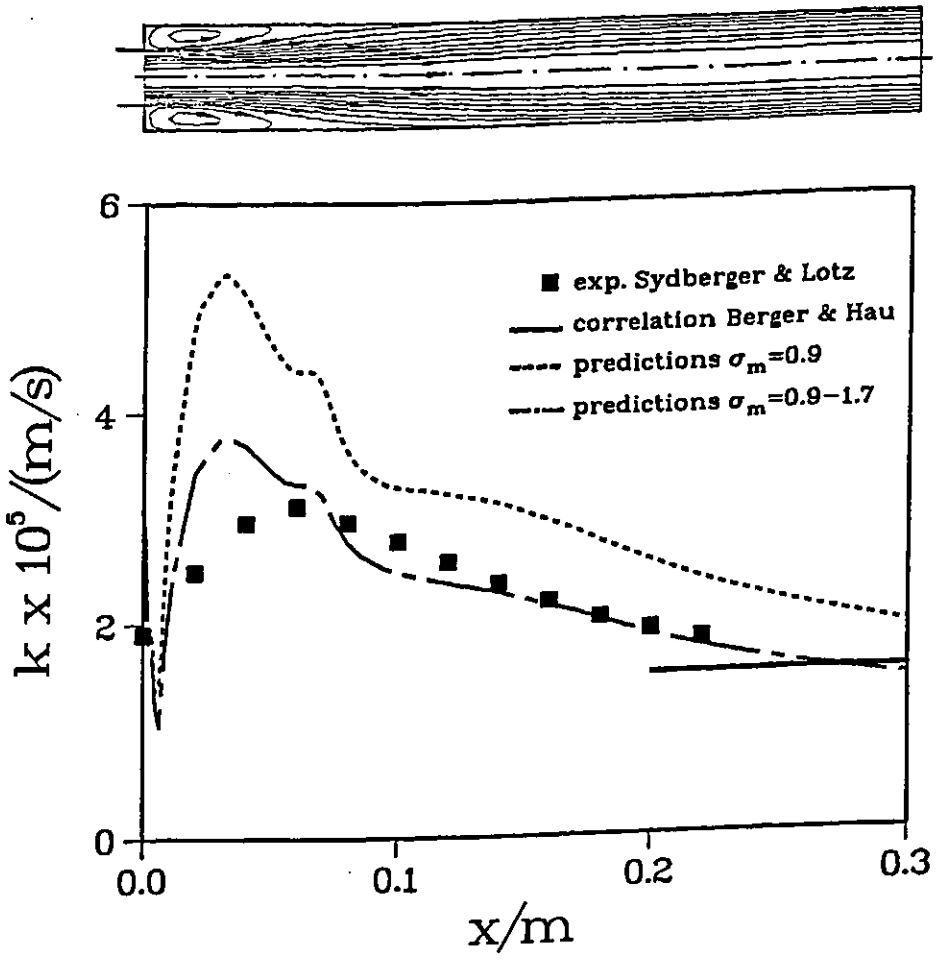

Figure 7.11: Water flow through a sudden pipe expansion; $d_{in} = 20.0$ mm; $d_{out} = 40.0$ mm; $v_{in} = 1.71$ m/s; $v_{out} = 0.42$ m/s; $Re_{out} = 2.1 \times 10^4$. Predictions and measurements for the mass transfer coefficients.

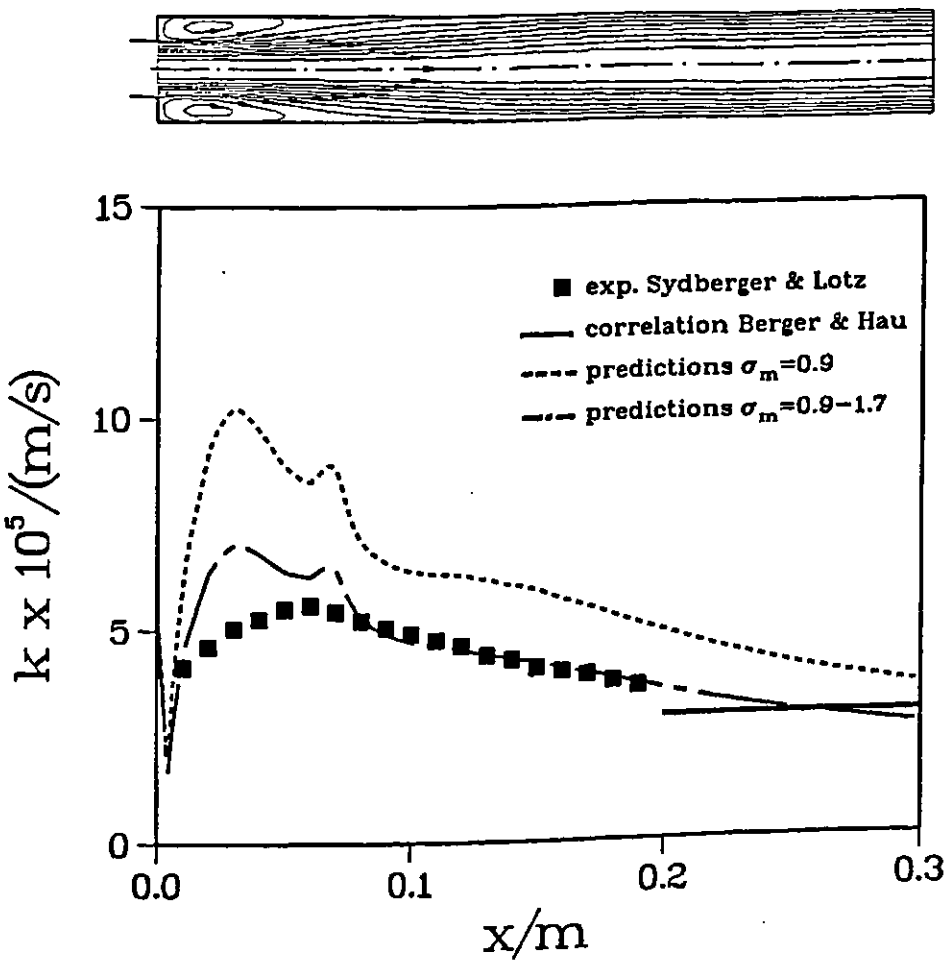

Figure 7.12: Water flow through a sudden pipe expansion; $d_{in} = 20.0$ mm; $d_{out} = 40.0$ mm; $v_{in} = 3.38$ m/s; $v_{out} = 0.84$ m/s; $Re_{out} = 4.2 \times 10^4$. Predictions and measurements for the mass transfer coefficients.

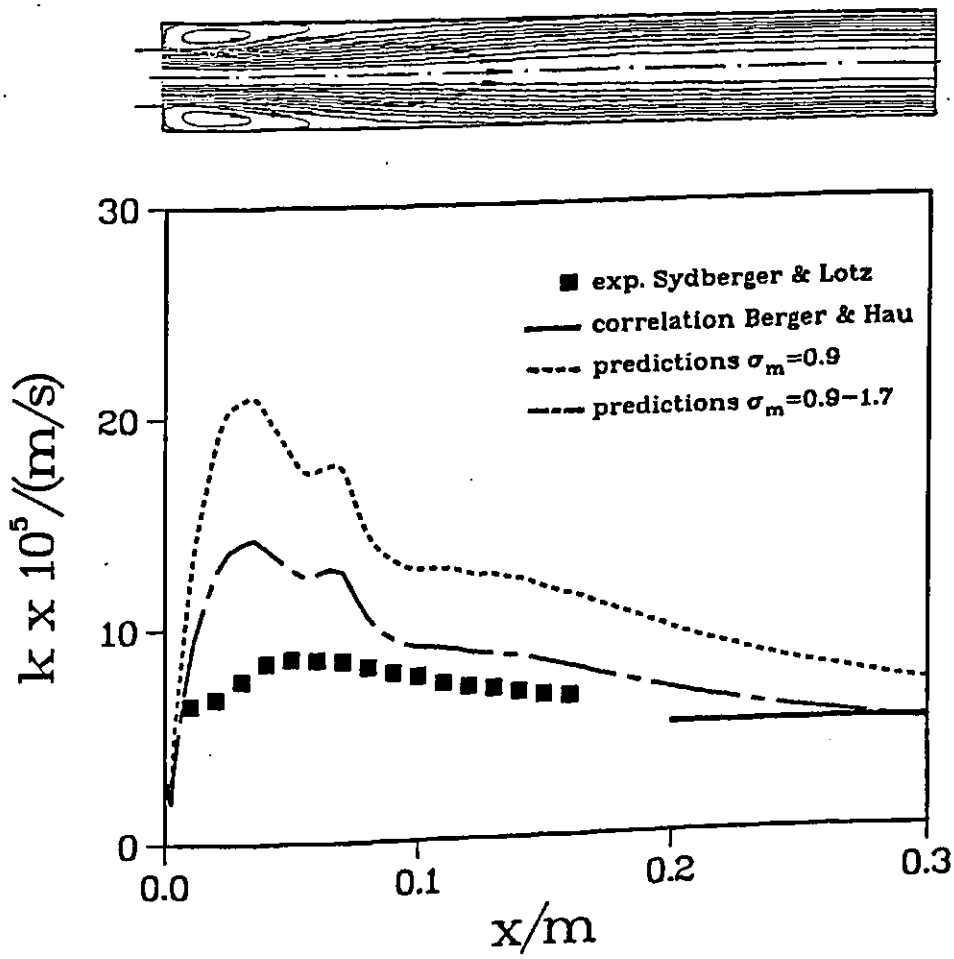

Figure 7.13: Water flow through a sudden pipe expansion; d_{in} = 20.0 mm; d_{out} = 40.0 mm; v_{in} = 6.75 m/s; v_{out} = 1.68 m/s; $Re_{out} = 8.4 \times 10^4$. Predictions and measurements for the mass transfer coefficients.

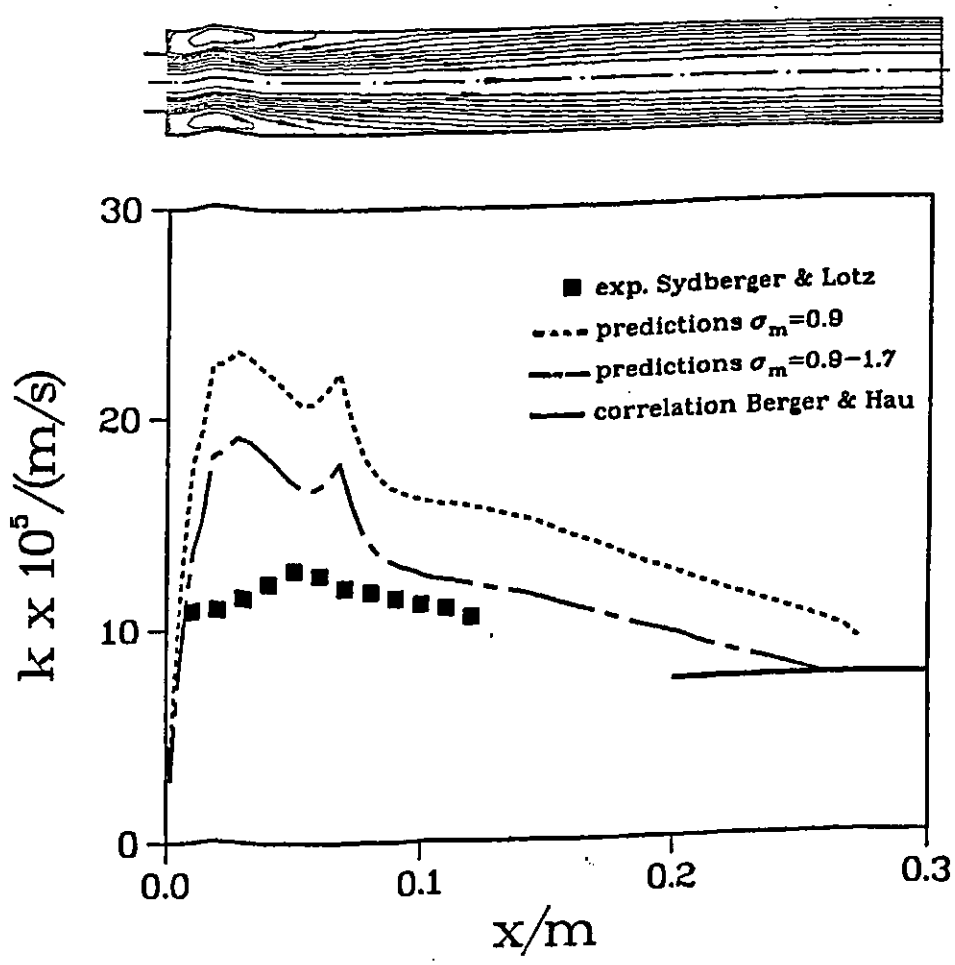

Figure 7.14: Water flow through a sudden pipe expansion; $d_{in} = 20.0$ mm; $d_{out} = 40.0$ mm; $v_{in} = 10.45$ m/s; $v_{out} = 2.62$ m/s; $Re_{out} = 13.0 \times 10^4$. Predictions and measurements for the mass transfer coefficients.

the maximum mass transfer coefficient was reduced from 120% to 50%. The maximum wall–mass transfer rates occur close to the reattachment point and coincide with the local maximum in turbulent momentum and mass transport. The location of the predicted maximum was upstream from the measured values, which can be attributed to the overprediction of turbulent transport in the recirculation zone.

Turbulent transport overrides the diffusional transport of mass in the bulk flow by several orders of magnitude. It is only very close to the wall in the viscous sublayer, where the turbulent transport is damped, that the two mechanisms have comparable effects. This can be seen in Fig. 7.15 and Fig. 7.16 which show the predicted momentum and mass transfer transport coefficients μ_{eff} and D_{eff}, and the corresponding variables U and m, in the near wall region for $Re = 2.1 \times 10^4$, at two locations: in the redeveloped flow region (Fig. 7.15) and just before the reattachment point (Fig. 7.16).

The transport coefficients (Fig. 7.15a and Fig. 7.16a) are shown on a log-log scale, because of the large range involved. Predictions downstream of the expansion where fully redeveloped turbulent flow can be assumed is shown in Fig. 7.15 . Far away from the wall (y$\geq$ 1 mm) the value of the effective viscosity is 100 times larger than the molecular value (Fig. 7.15a); thus the flow is dominated by turbulent transport. As we approach closer to the wall (y$\approx$ 200μm) the magnitude of the effective viscosity approaches the value

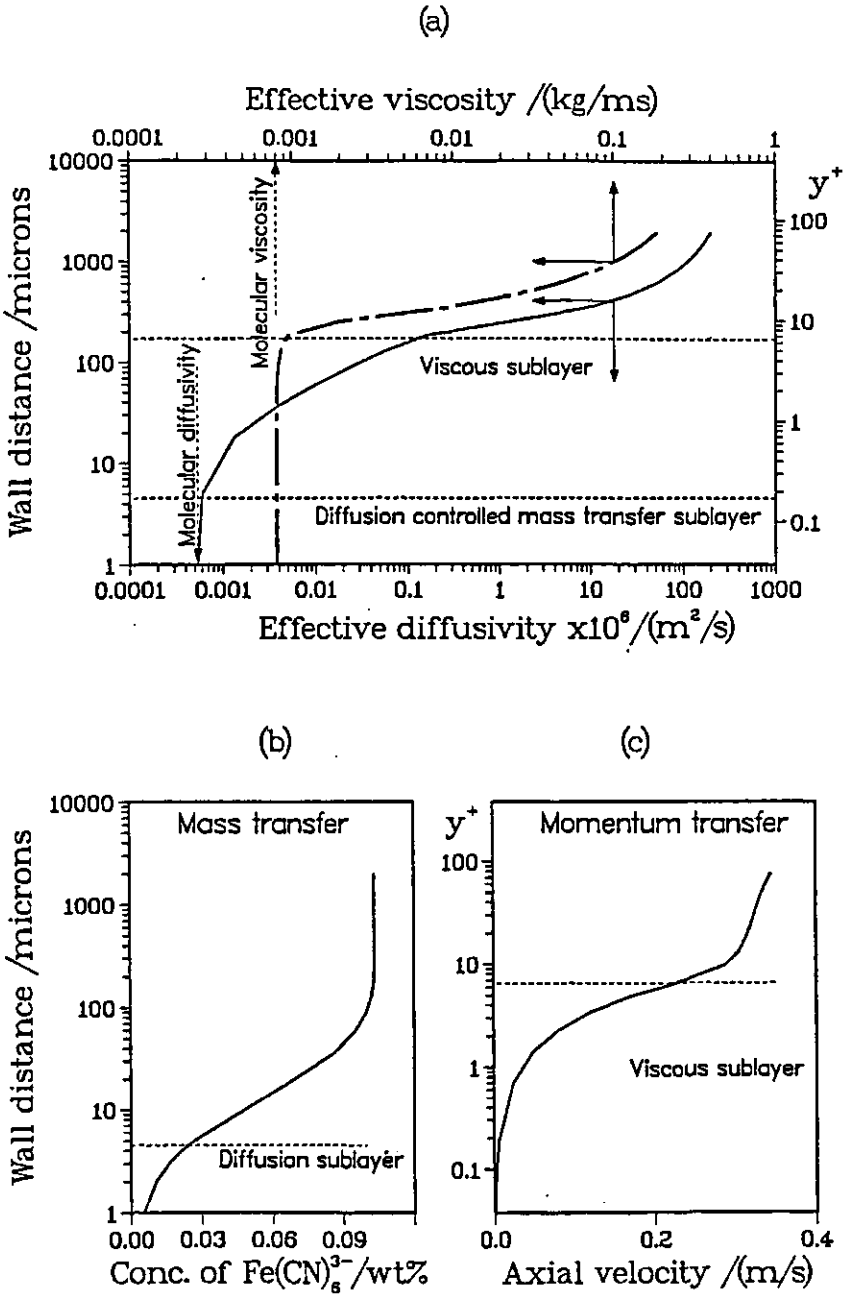

Figure 7.15: Water flow through a sudden pipe expansion; $d_{in} = 20.0$ mm; $d_{out} = 40.0$ mm; $v_{in} = 1.71$ m/s; $v_{out} = 0.42$ m/s; $Re_{out} = 2.1 \times 10^4$. Predictions for the (a) transport coefficients; (b) concentration; (c) axial velocity profiles vs. wall distance. Location: redeveloped flow downstream of the reattachment point.

of the molecular viscosity, indicating that the turbulence is gradually being damped. Consequently a line can be drawn (y$\approx$ 150μm) that denotes the edge of the viscous sublayer, in which region the flow is controlled by viscous forces. In terms of the standard wall coordinates, this is very close to $y^+ = 5$ as expected [90]. Fig. 7.15c shows the predicted axial velocity profile on a semi-log scale. The profile has the well known universal shape: in the viscous sublayer $u^+ = y^+$ and in the law–of–the–wall region $u^+ = \frac{1}{\kappa} \log Ey^+$.

Similar conclusions may be reached for mass transfer. The effective diffusivity in the bulk flow is 5 orders of magnitude higher than molecular diffusivity (Fig. 7.15a), indicating that turbulent mixing is very intense. Concentration profiles obtained for the bulk are flat; changes are only noticed when the viscous sublayer is approached (Fig. 7.15b). In the outer part of the viscous sublayer the turbulent viscosity is less than 1% of the effective viscosity, indicating that very little turbulence is retained. Nevertheless, the effective diffusivity is still 100 times larger than the molecular diffusivity. This suggests that the residual turbulence, which is not significant from the momentum transport point of view, is very significant from the mass transfer point of view. This behaviour is to be expected for fluids with large Schmidt numbers. Turbulent mass transport is reduced as the wall is approached, becoming insignificant some 5μm from the wall ($y^+ \approx 0.2$) when mass is transported exclusively by molecular diffusion. The thickness of the molecular diffusion controlled

mass transfer sublayer $\delta_m \approx 5\mu$m, compared to the thickness of the viscous sublayer $\delta \approx 150\mu$m, is very close to the ratio suggested by Levich [71] i.e. $\delta_m = \delta/Sc^{0.33}$. Fig. 7.15b shows the predicted concentration profile, which in analogous fashion to the velocity profile exhibits a diffusion sublayer.

Fig. 7.16 contains similar information to Fig. 7.15, but for the region of the wall just before the reattachment point. Because of the increased turbulence in this region, both the hydrodynamic and mass transfer boundary layers are thinner, but still retain a similar ratio. The velocity profile, in the region above the viscous sublayer reflects the flow reversal associated with the recirculation.

It can be concluded that computations have confirmed that for flows with high Schmidt numbers, the mass transfer boundary layer is completely embedded within the viscous sublayer. Low levels of turbulent transport in the viscous sublayer, insignificant from the hydrodynamic point of view, override the diffusional mass transport throughout most of the hydrodynamic viscous sublayer. Thus the diffusion controlled mass transfer sublayer is much thinner than viscous sublayer. Although not initially intended for application in the viscous sublayer, modifications to turbulence models for near wall regions, coupled with the use of the turbulent Schmidt number, enable successful predictions of mass transfer rates in complex turbulent recirculating flow even for high Schmidt numbers. Good agreement was obtained over the large range of Reynolds numbers ($Re = 2.1 - 13 \times 10^4$ and $Sc = 1460$), without any "tuning"

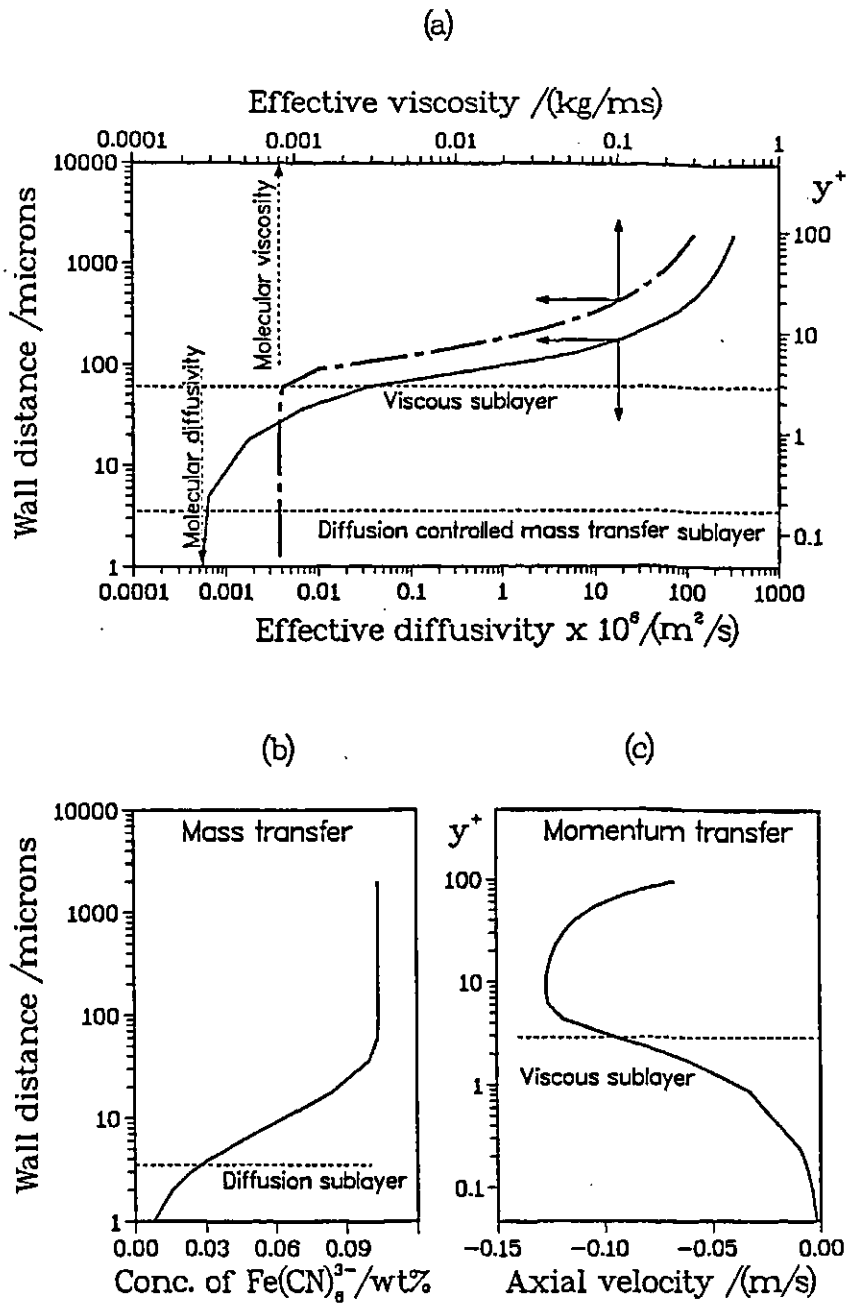

Figure 7.16: Water flow through a sudden pipe expansion; d_{in} = 20.0 mm; d_{out} = 40.0 mm; v_{in} = 1.71 m/s; v_{out} = 0.42 m/s; $Re_{out} = 2.1 \times 10^4$. Predictions for the (a) transport coefficients; (b) concentration; (c) axial velocity profiles vs. wall distance. Location: the recirculation region before the reattachment point.

of the transport equations or turbulence model.

7.4 Particle Motion Results

The first hydrodynamic tests of a similar numerical two–phase flow model to the one used in this work were done by Milojević [29], [30]. He compared his predictions with three different experiments from literature by: Snyder and Lumley [31], Wells and Stock [32] and Arnason [33], and obtained a good agreement for the dispersion of particles in a turbulent air flow field, for all three test cases. Milojević [29], [30] also compared his predictions with his own results of local flow measurements using Laser–Doppler anemometry in a two-dimensional confined two-phase jet flow. His results were good although some discrepancies were found in the region close to the wall due to the wall function approach for modelling the boundary layer flow.

In the present study the particle motion model, was tested by simulating the flow of a liquid/solid mixture through a sudden pipe expansion. The hydrodynamic measurements of Blatt et al. [44] were used to verify the accuracy of the employed flow model (Nešić and Postlethwaite [87]). Blatt et al. [44] have shown LDV measurements for flow of water carrying 1000 ppm of 800 μm diameter glass spheres through a sudden pipe expansion.

Fig. 7.17a shows the predicted fluid streamlines with the flow separation

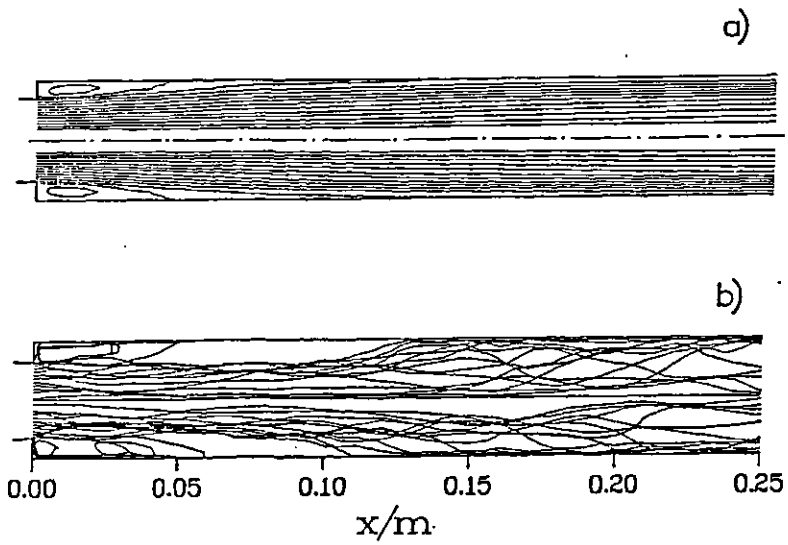

Figure 7.17: 0.1%vol. sand/water flow through a sudden pipe expansion; d_{in} = 26.0 mm; d_{out} = 40.0 mm; v_{in} = 1.14 m/s; v_{out} = 0.48 m/s; $Re_{out} = 2.4 \times 10^4$. a) Predictions for the fluid flow streamlines; b) A sample of 30 of the 2000 predicted particle trajectories.

and reattachment and the recirculation zone in the corner, and Fig. 7.17b presents a small sample (30) of the calculated particle trajectories. The effect of turbulence on the stochastic nature of particle motion is clearly visible. It can be noticed that a small proportion of particles gets caught up in the recirculation zone, while the majority are carried toward the wall by the fluid.

The measured and predicted decay of the mean fluid axial centreline velocity is shown in Fig. 7.18a. Both curves have the same character with the maximum discrepancy (10%) being somewhat larger than for single–phase flow (Fig. 7.4a). Predictions show somewhat faster spreading of the jet which is typical for the used model of turbulence. Further, downstream higher values are obtained in the simulations. It is suspected that "migration" of particles towards the walls is higher in the predictions, yielding smaller concentrations

of particles in the core, this causing lower drag and smaller deceleration of the fluid. The opposite effect is noticeable when measurements and predictions are compared in the near–wall region (Fig. 7.18a). The axial velocity 2 mm from the wall is slightly underpredicted.

Fig. 7.18b shows comparisons of predictions and measurements of the fluid radial velocity components, mean and fluctuating, 2 mm from the wall. As in LDV measurements the measuring volume is approximately 1 mm in diameter, and the gradients in the near wall region are very high, predictions near the wall are shown as a shaded area bordered with values obtained at 1.5 mm and 2.5 mm, from the wall. The predictions of the fluid fluctuating velocity show good agreement with the measured values, taking into account that the predictions show a space–averaged value, while the measurements present the radial component of the fluctuating velocity near the wall. The predicted asymptotic value is higher, as it is known that near the wall the axial component of the fluctuating velocity is larger than the radial, so the predicted space–averaged value is expected to be larger than the measured radial component. Predictions of mean fluid radial velocity show moderate agreement with the experiments.

Fig. 7.18c shows the particle mean axial velocity at the centreline and 2 mm from the wall. In case of the centreline velocity, the agreement between the predictions and measured values is good. The near–wall values show larger

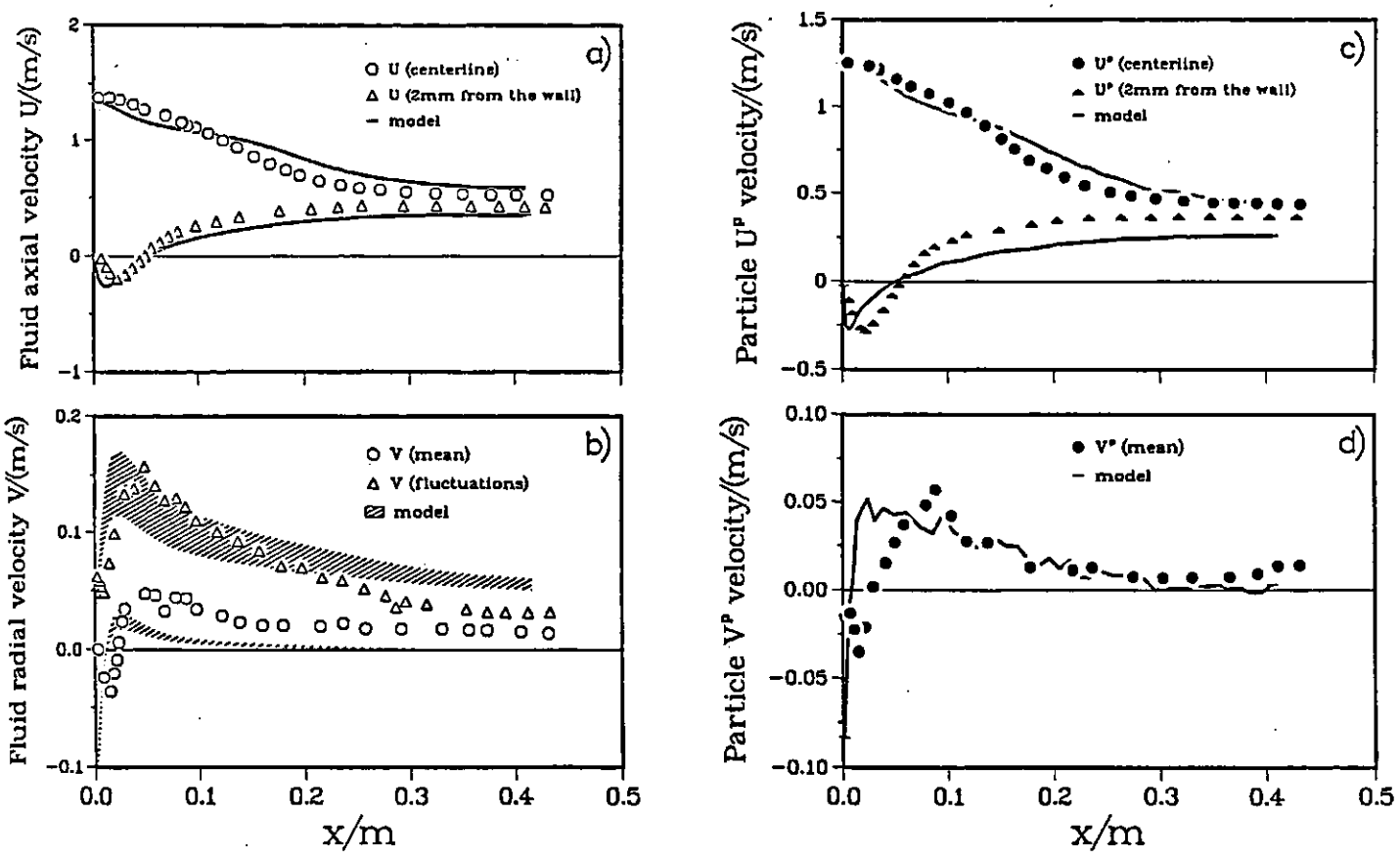

Figure 7.18: 0.1% sand/water flow through a sudden pipe expansion; d_{in} = 26.0 mm, d_{out} = 40.0 mm; v_{in} = 1.14 m/s; v_{out} = 0.48 m/s; Re_{out}=2.4x10^4. a) Predictions and measurements of the mean axial fluid velocity. b) Predictions and measurements for the mean and fluctuating component of the radial fluid velocity, 2 mm from the wall. c) Predictions and measurements of the particle mean axial velocity. d) Predictions and measurements for the particle mean radial velocity, 2 mm from the wall. Measurements taken from Blatt et al.

discrepancies, although the character of the curve is captured with the predictions. The agreement for the near-wall particle mean radial velocity profiles shown in Fig. 7.18d is similar. Milojević et al. [29], [30] reported similar problems in the near wall region when they simulated flow of a confined coaxial air jet loaded with glass spheres. One explanation is the inadequacy of the wall function approach in modelling two-phase flow, as particles interfere with the shape of the universal velocity profile. Also, near the wall due to the particle–wall interactions, interpretation of particle parameters is quite complicated. Overall, we can consider the agreement of the predicted and measured hydrodynamic parameters satisfactory.

7.5 Erosion Results

Being reasonably satisfied with the verification of the particle motion model the next step was to verify the erosion model and to check which of the erosion equations presented perform the best when coupled with our two–phase flow model. Some preliminary analysis was done to estimate the feasibility of application of each particular set of erosion equations.

7.5.1 The Preliminary Test

A simple test case was selected: impact of a stream of particles at $\alpha = 30^o$ angle on the surface of mild steel at a rate of $\tilde{m}^p$=1 kg/m^{2}s and velocity of $\vec{V}^p$ =3

m/s. Then predictions were made by using Bitter's erosion equations (6.4) as well as Finnie's (6.2) and Bergevin's (6.6). Using Bitter's equations (6.4) metal loss rates obtained were: deformation wear $Q_D \approx 0.23$ mm/y, cutting wear $Q_C \approx 4.83$ mm/y yielding the total wear of $Q \approx 5$ mm/y. When using the same yield strength and critical velocity, Bergevin's equations (6.6) predicted $Q \approx 3.5$ mm/y while Finnie's equations (6.2) gave $Q \approx 11.15$ mm/y (if the constant $c = 0.5$ then $Q \approx 5.5$ mm/y). Although Bitter's equations (6.4) have the most sound theoretical basis they also have the largest number of experimental constants which are difficult to obtain. Consequently, Bitter's equations (6.4) were not used in the part of the program for erosion.

7.5.2 Validation of the Full Erosion Model

Stainless steel erosion measurements of Lotz and Postlethwaite [60] for flow of a 2% vol. sand slurry through a sudden pipe expansion were used as a test of the presented model of erosion (Nešić and Postlethwaite [87]). Most important geometric and hydrodynamic parameters are given in Table 7.4. In order to calculate erosion rates information on particle–wall impact is needed: angles of impact, velocities and mass of impacting particles, along the pipe wall. In order to obtain a converged numerical solution, calculation of 2000 individual trajectories was performed. Predicted particle–wall impact parameters that are presented are averages, over all impacts registered at a given location on

the wall.

At any single location on the pipe wall a spectrum of impacts was recorded. The distribution of impact angles and impact velocities at a location just downstream from the reattachment point is shown in Fig. 7.19. It can be seen that the largest proportion of the impacts occured at angles between 50° and 60° which is expected close to the reattachment point. There is a significant number of impacts at angles between 10° and 30° which are the most severe cutting conditions. However, most of the impacts were below the elastic limit for steel $V_{cr} = 0.668$m/s. As we move away from the reattachment point downstream, the maxima in the distribution curves will shift toward the lower values and vice-versa.

Predicted average particle–wall impact parameters are shown in Fig. 7.20. The average number of impacts (Fig. 7.20b) varies from 2-20 /(mm^{2}s), which corresponds to an average impact mass of 0.2-2.5 kg/(m^{2}s). The maximum is moved downstream from the reattachment point and reflects the inertia of the particles, which do not "sense" the sudden expansion directly but rather through the drag force of the fluid. The average impact angle (Fig. 7.20c) has a maximum (60°) close to the fluid reattachment point, which is to be expected, as this is the turn-around point for the particles that get caught up in the recirculation eddy. Further, downstream the average angle of impact decreases and is about 5° in the region of a fully redeveloped turbulent pipe

Table 7.4: Test case for the erosion model – important geometric, hydrodynamic and numerical parameters

Inlet diameter (mm)	21
Outlet diameter (mm)	42
Length (mm)	500
Inlet fluid velocity (m/s)	13.2
Outlet fluid velocity (m/s)	3.3
Inlet Reynolds number	340000
Outlet Reynolds number	170000
Particle diameter (μm)	430
Inlet particle velocity (m/s)	13.1
Particle concentration (%vol.)	2
Number of x grid points	58
Number of y grid points	14
Number of particle trajectories	2000
Number of iterations	351
Total error of predictions (%)	1
VAX 6320 CPU time (min)	152

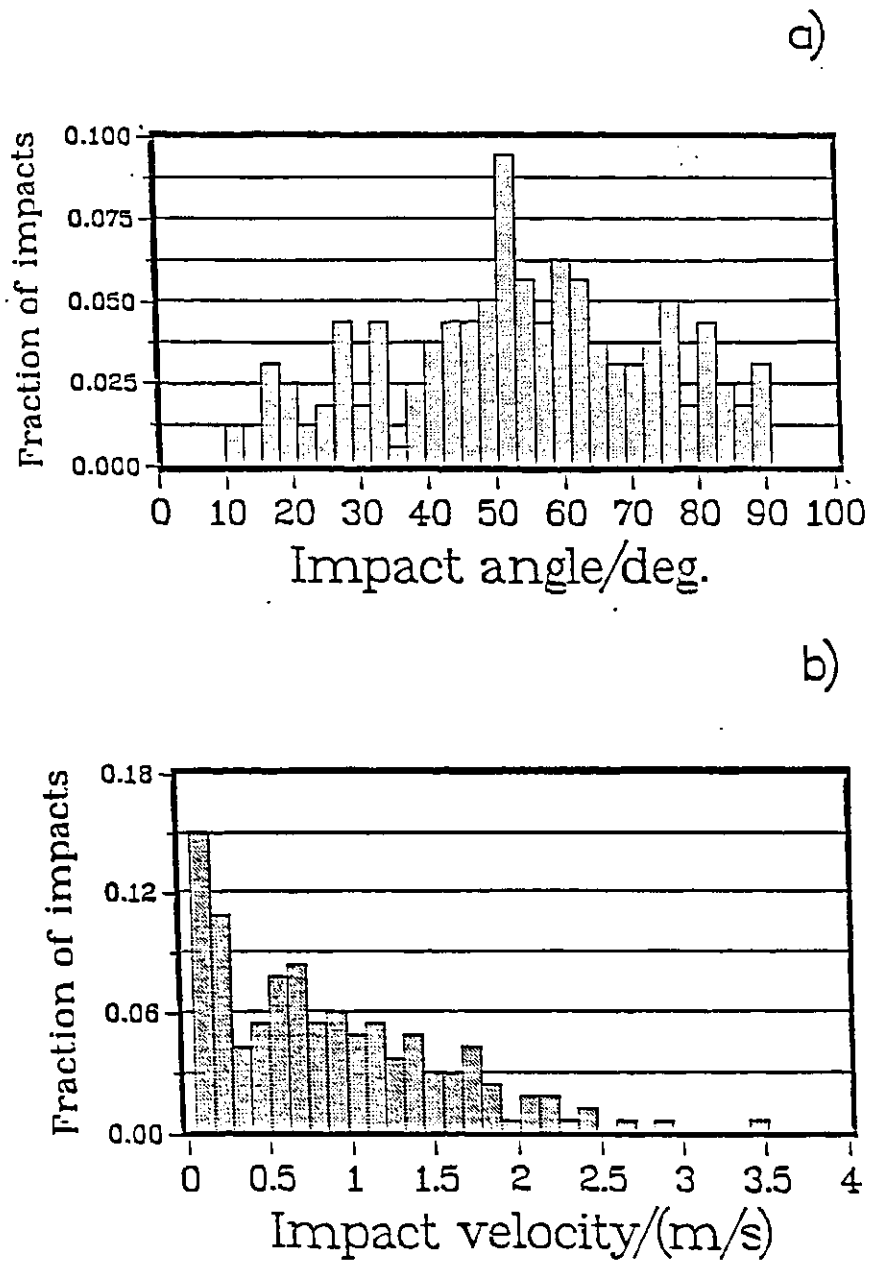

Figure 7.19: 2% sand/water flow through a sudden pipe expansion; d_{in} = 21.1 mm; d_{out} = 42.5 mm; v_{in} = 13.2 m/s; v_{out} = 3.3 m/s; Re_{out}=17.0×10^4. a) Predicted distribution of particle–wall impact angles at a location 70 mm downstream of the expansion; b) Predicted distribution of particle–wall impact velocities perpendicular to the wall at a location 70 mm downstream of the expansion. Location: just after the reattachment point.

flow. This corresponds to the so called "sliding impacts" that create very little erosion. The curve of the average particle impact radial velocity (perpendicular to the wall), shown in Fig. 7.20d, has a similar character, as the two are related directly. Maximum values of 0.8 m/s are above the critical velocity $V_{cr} = 0.668$ m/s determined by Bitter [82], for erosion of stainless steels. In the region of redeveloped turbulent flow, the predicted average impact velocity of the sliding impacts is lower than this limit, which does not mean that there are no individual impacts that exceed the limit. This can be seen on Fig. 7.21 where a comparatively smaller but finite rate of erosion was predicted despite the average velocity being smaller than critical.

Both the original Finnie equations (6.2) and Bergevin's modified equations (6.6) were incorporated into the LSD particle motion model. Predictions obtained with Finnie's equations (6.2) shown in Fig. 7.21b are an order of magnitude higher than the measured values of Lotz and Postlethwaite [60]. If the value of the arbitrary constant of $c = 0.5$ was used as suggested by Finnie [62], the predicted values would still be too high. The other problem is the shape of the predicted erosion profile, which does not resemble the character of the measured erosion profile. The local minimum close to the reattachment point corresponds to high impact angles, where this model is known to underpredict erosion. Our conclusion is that Finnie's equations (6.2), even tuned with the c constant, still do not give satisfactory predictions. The reason is

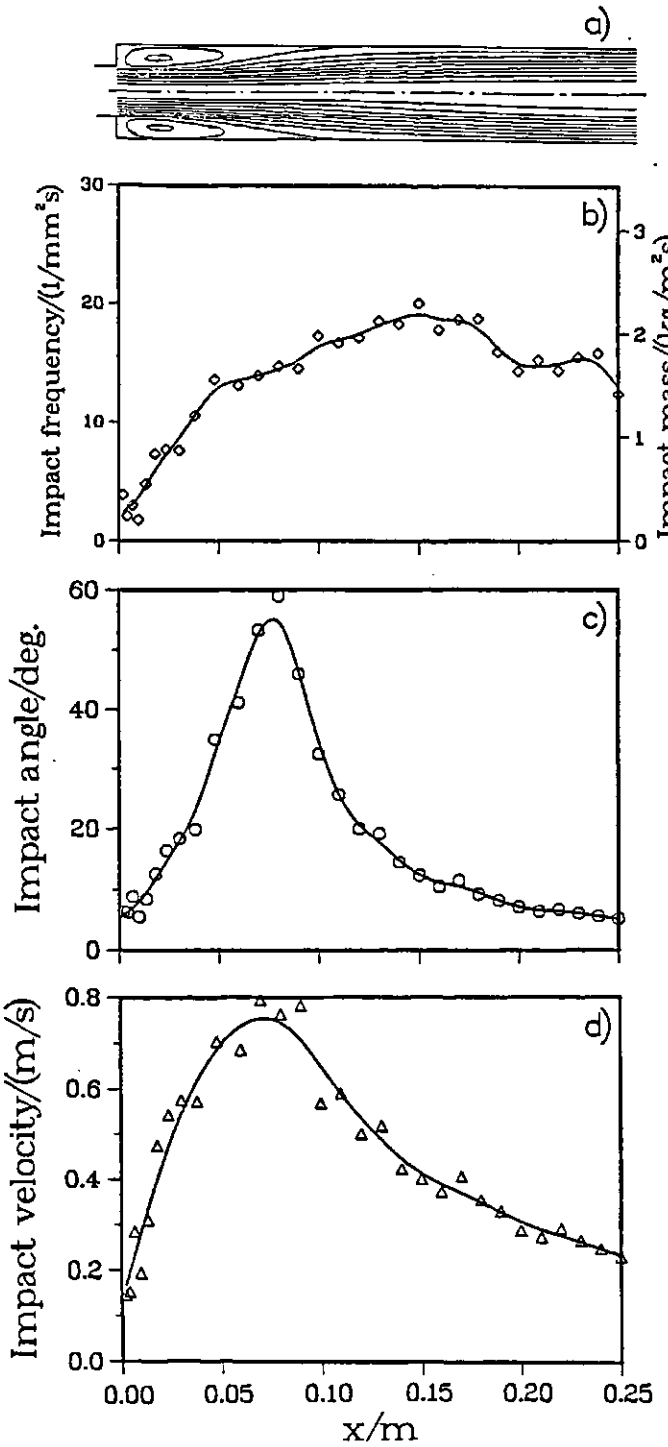

Figure 7.20: 2% sand/water flow through a sudden pipe expansion; d_{in} = 21.1 mm; d_{out} = 42.5 mm; v_{in} = 13.2 m/s; v_{out} = 3.3 m/s; Re_{out}=17.0×10^4. a) Predicted fluid flow streamlines; b) Predicted average particle–wall impact frequency and impact mass; c) Predicted average particle–wall impact angle; d) Predicted average particle–wall impact velocity perpendicular to the wall.

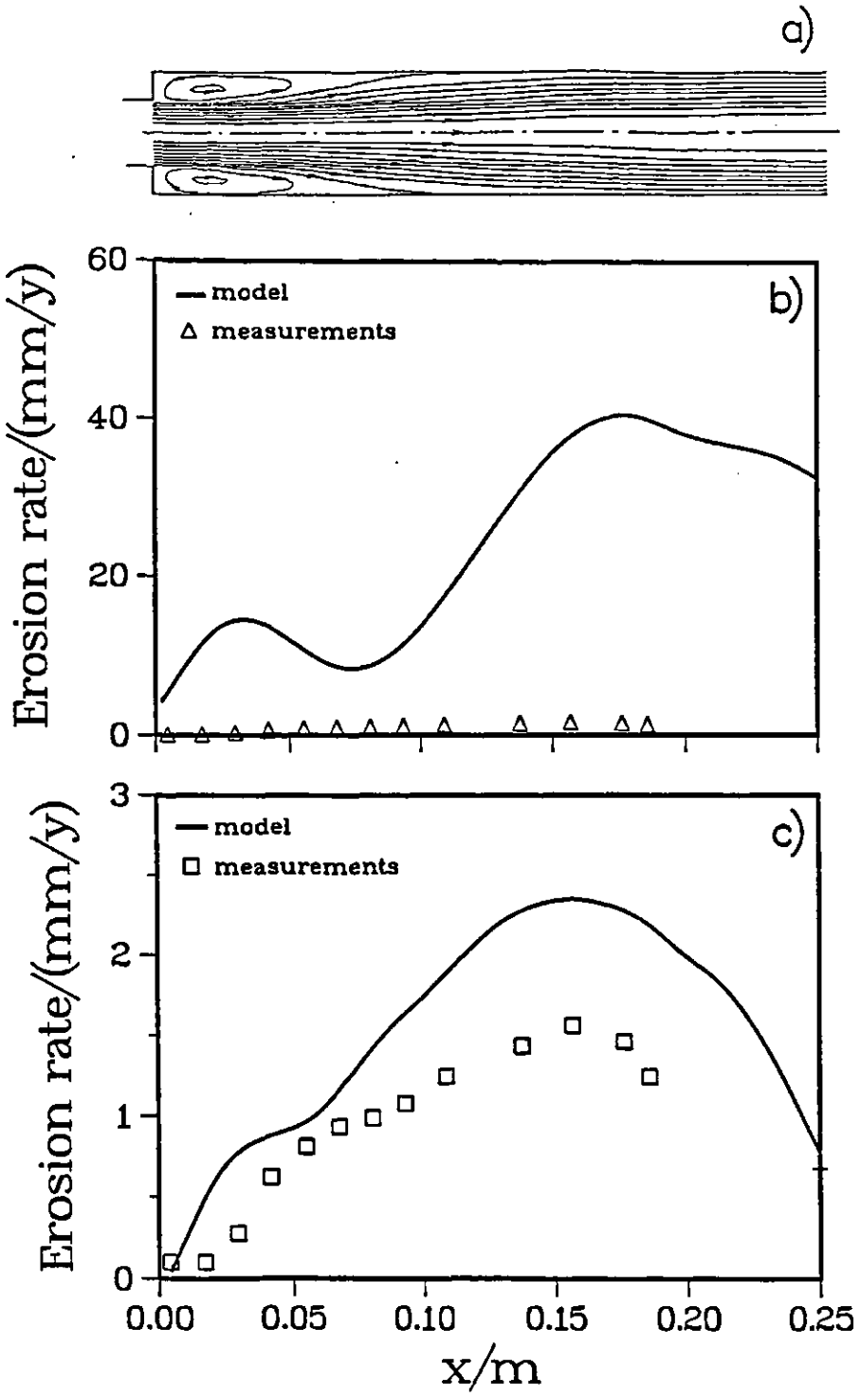

Figure 7.21: 2% sand/water flow through a sudden pipe expansion; d_{in} = 21.1 mm; d_{out} = 42.5 mm; v_{in} = 13.2 m/s; v_{out} = 3.3 m/s; Re_{out}=17.0×10^4. a) Predicted fluid flow streamlines; b) Stainless steel erosion rate measurements and predictions made with Finnie's equations; c) Stainless steel erosion rate measurements and predictions made with Bergevin's equations; Measurements taken from Lotz and Postlethwaite.

that the initial assumption inherent to the model, that every impact creates a damage, which is known to be wrong, is only masked but not eliminated with the use of the constant c.

On the other hand predictions obtained with Bergevin's equations (6.6) shown in Fig. 7.21c, have the same order of magnitude and character as the measured profile of erosion. This suggests that using Bitter's [82] concept of critical velocity V_{cr}, is correct. His value given for stainless steel ($V_{cr} = 0.668$ m/s), used directly in our model, gave good predictions. Also, there is no need for the arbitrary constant c, which adds to the generality of the model. The shortcomings of Finnie's [62] model related to high impact angles have not been eliminated in this model completely, but are of much less significance. This could be improved by using an additive correction for high impact angles as suggested by Zeisel and Durst [57]. Some scattering of the predicted points, not shown in Fig. 7.21, was obtained due to the statistical procedure by which the results were obtained. The number of trajectories (2000) used, should be increased to smooth out the predictions, but this was impractical on the computer used, with respect to the already very long computation time (Table 7.3.).

7.6 Erosion–Corrosion Results

Once all the components of the model have been successfully tested the overall model of erosion–corrosion was to be verified.

7.6.1 Single-Phase Flow Erosion–Corrosion

In single–phase flow erosion–corrosion, in the presence of rust films mass transfer is not limited only by the presence of the fluid boundary layer, but also by presence of the rust and/or scale films. To study this problem measurements of erosion–corrosion in disturbed flow conditions in the presence of rust films, by Lotz and Postlethwaite [60] were used. Most important geometric and hydrodynamic parameters are given in Table 7.5.2.

Predicted streamlines, the level of turbulent fluctuations in the near-wall region, the corresponding profile of the wall shear stress, and the measured values of metal loss by erosion-corrosion, are shown in Fig. 7.22.

Comparing the profile of metal loss (Fig. 7.22c) with the predicted curves for wall shear stress (Fig. 7.22b), it is clear that the shear stress cannot account for increased mass transfer and corrosion due to stripping of the rust film, as shear stress is zero at the reattachment point, where metal loss rate reaches its maximum. The profile of near-wall turbulence (Fig. 7.22b) displays a similar character as the metal loss profile with the maximum slightly moved towards the expansion. Thus, we are led to conclude that local levels of turbulence are

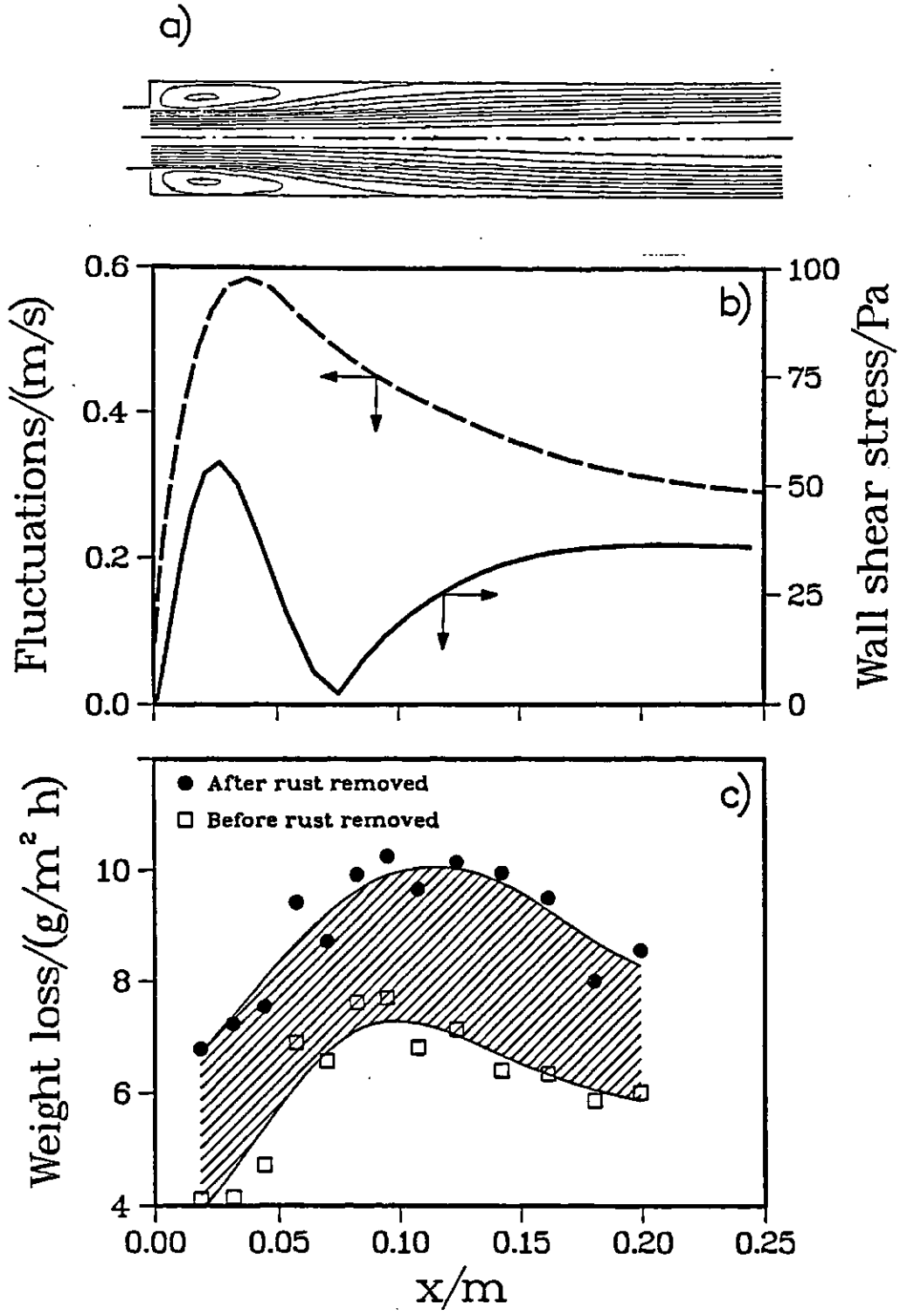

Figure 7.22: Water flow through a sudden pipe expansion; d_{in} = 21.1 mm; d_{out} = 42.5 mm; v_{in} = 13.2 m/s; v_{out} = 3.3 m/s; Re_{out}=17.0×10^4. a) Predicted fluid flow streamlines; b) Profiles of predicted near-wall turbulence and wall shear stress; c) Measured rate of metal loss by erosion-corrosion after 48h (Lotz and Postlethwaite).

somehow related to measured increased levels of metal loss. We know from the mass transfer analysis, that turbulent transport causes an increase in the local mass transfer coefficient. But when rust films are present the rate of the corrosion reaction is limited by the diffusion through the film as well as the boundary layer.

Fig. 7.22c suggests that part of the rust formed on the surface has been removed. It can also be noticed that the amount of rust retained on the surface is nearly constant but the rate of removal is highest at the point of maximum metal loss, which corresponds to the maximum in near–wall turbulence. Thus the point of maximum rate of rust removal (erosion) coincides with the point of maximum rust production (corrosion). Both are related to the maximum in the near–wall turbulence. Where near-wall turbulence is not as high, corrosion rate and production of the rust is slower, but so is the erosion of the rust by the pounding turbulent fluctuations. This explains the rather uniform thickness of the film.

On the other hand, if the thickness of the rust layer is uniform it would mean that its resistance to mass transfer is also uniform. Measured differences in metal loss rates, along the length of the expansion are then only a consequence of the differences in mass transfer through the boundary layer. So the overall shape (character) of metal loss curve is determined by the transport through the boundary layer (by the flow structure), while the magnitude of the metal

loss rate is additionally influenced by the transport through the rust film which acts as a damper. Flow (near-wall turbulence) affects both. Although initially a large proportion of formed rust is removed, as time progresses experience tells us that the thickness of the rust layer increases which decreases the overall metal loss rate. In addition, damping of the flow effect must increase, to a point where it cannot be distinguished.

In order to estimate the magnitude of the effects discussed, we can use the correlation from Fig. 7.9 and use the $k-\epsilon$ WF model to predict levels of near–wall turbulence. For the maximum level of turbulent fluctuation of 0.6 m/s ($x \approx 50$ mm) the correlation in Fig. 7.9 gives $Sh/Sc^{0.33} = 845$ and corrected for the Schmidt number (Sc=352), Sh=5852. This means that the corresponding mass transfer coefficient for the liquid boundary layer is $k_l = ShD/d = 3.26 \times 10^{-4}$ m/s. The estimated effective thickness of the mass transfer boundary layer at this point is 5 μm, which is at least an order of magnitude smaller than the estimated thickness of the hydrodynamic boundary layer for the same point.

From the measured maximum corrosion loss rate we can calculate the overall mass transfer coefficient to be $k_o = 2.13 \times 10^{-4}$ m/s. Here, we can keep in mind that this is an average value for the time interval measured (48 h) while the instantaneous value is smaller. If we assume the double layer resistance for mass transfer:

$$\frac{1}{k_o} = \frac{1}{k_l} + \frac{1}{k_s} \tag{7.2}$$

and an increase in the liquid mass transfer coefficient by a factor of 1.8, to account for the effect of roughness (Lotz and Postlethwaite [60]), then $k_l = 5.86 \times 10^{-4}$ m/s, and the mass transfer coefficient for the rust layer is $k_s = 3.34 \times 10^{-4}$ m/s. Comparing the two values we can conclude that at the point of maximum turbulence and mass transfer, the limiting resistance for mass transfer is in the rust film. Had we used an instantaneous value of the overall mass transfer coefficient instead of the time average the difference would be even larger. Further, downstream where the effect of disturbed flow is lost, the two resistances are of the same order.

7.6.2 Two-Phase Flow Erosion–Corrosion

Sudden Expansion. Measurements of Lotz and Postlethwaite [60], with flow of an oxygen saturated 2% sand slurry, through a sudden carbon–steel pipe expansion, were used to verify the model of two–phase flow erosion–corrosion. In their analysis the authors suggested that nearly all the formed rust was removed by the erosive action of the particles which was one of the assumptions in our corrosion model. As the corrosion rate was oxygen–mass transfer controlled, in the absence of a rust layer the only resistance for mass transfer was in the liquid boundary layer.

The local corrosion rates were calculated from the local oxygen wall–mass fluxes. Concentration of oxygen at the wall was set to zero. The wall-flux was calculated based on the knowledge of the molecular diffusion coefficient and the concentration of oxygen in the node closest to the wall (which was placed deep into the molecular–diffusion–controlled mass transfer boundary layer). In the case of iron the reaction scheme shown below applies [59], where it was assumed that the overall reaction is completed at the pipewall and that none of the Fe^{++} ions produced by the primary electrochemical reactions are transported across the mass transfer boundary layer prior to their subsequent chemical oxidation.

$2Fe \rightarrow 2Fe^{++} + 4e^{-}$	electrochemical reactions
$O_2 + 2H_2O + 4e^{-} \rightarrow 4OH^{-}$	at the pipewall
$2Fe^{++} + 4OH^{-} \rightarrow 2Fe(OH)_2$	precipitation at the pipewall
$\underline{2Fe(OH)_2 + \frac{1}{2}O_2 + H_2O \rightarrow 2Fe(OH)_3}$	chemical oxidation at the pipewall
$2Fe + 1\frac{1}{2}O_2 + 3H_2O \rightarrow 2Fe(OH)_3$	overall reaction

As a first approximation, to predict the mass transfer resistance of the boundary layer we used the correlation for the Sherwood number (Fig. 7.9). The predicted level of turbulent fluctuations in the law–of–the–wall region,

for this case, 100 mm downstream of the expansion, where measured erosion–corrosion rate reaches its maximum, is 0.43 m/s. The correlation yields a Sherwood number Sh=4882, when corrected for the actual Schmidt number ratio. This corresponds to a mass transfer coefficient of 2.72×10^{-4} m/s, and finally an increase by a factor 1.8, to account for the effect of roughness (Postlethwaite and Lotz [91]), gives a predicted oxygen–mass transfer coefficient $k_l = 4.9 \times 10^{-4}$ m/s. Converted into a metal loss rate this is 25 mm/y. When we add the erosion component of the bare metal determined by the erosion model with Bergevin's equations (6.6) of 1.5 mm/y, the final predicted metal loss rate is 26.5 mm/y. The measured rate of metal loss in the erosion–corrosion experiments (Fig. 7.23b), was 27 mm/y. The agreement with the predicted value is very good.

Further, downstream the flow returns to a fully developed turbulent pipe flow, and going through the same calculation procedure we can predict a corrosion rate of 19.2 mm/y and an erosion rate of 0.8 mm/y. The total metal loss rate of 20 mm/y is close to the asymptotic value suggested by the experimental curve. A corrosion rate of 23 mm/y is obtained, if the experimental correlation of Postlethwaite and Lotz [91] for mass transfer at rough surfaces in pipes carrying slurries, is used instead, which is slightly higher.

Comparison of the overall predicted rate of metal loss (corrosion plus erosion), is in good agreement with the measured erosion–corrosion rate (Fig. 7.23b).

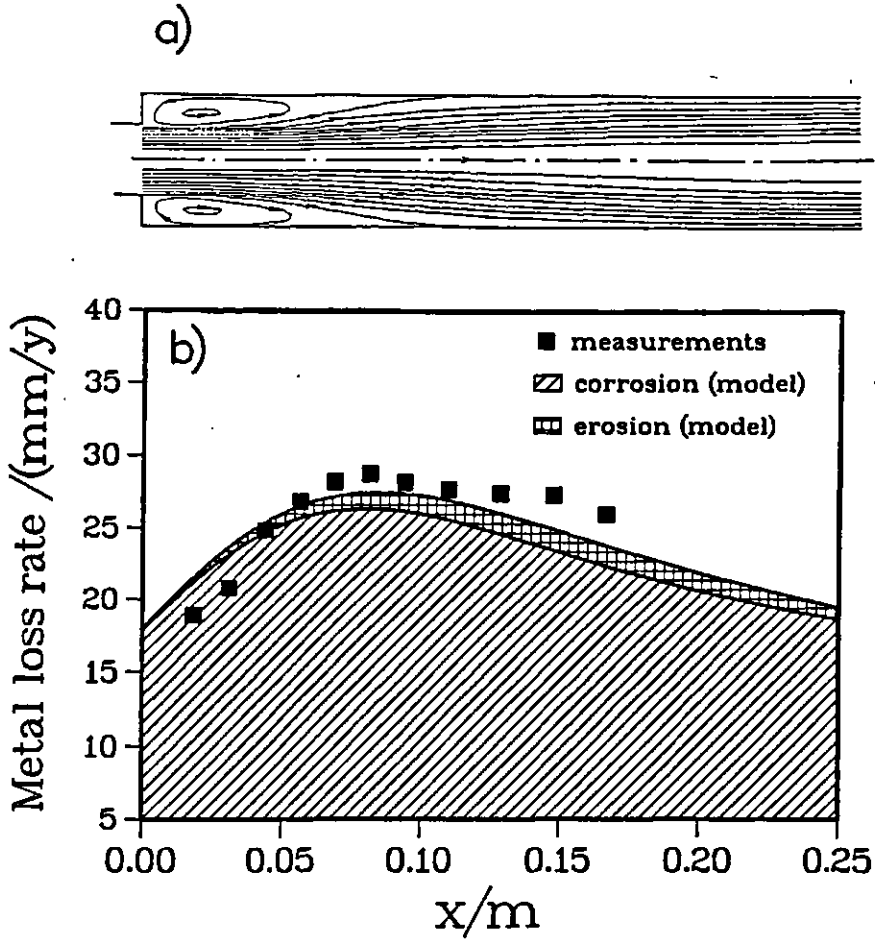

Figure 7.23: 2% sand/water flow through a sudden pipe expansion; d_{in} = 21.1 mm; d_{out} = 42.5 mm; v_{in} = 13.2 m/s; v_{out} = 3.3 m/s; Re_{out}=17.0×10^4. a) Predicted fluid flow streamlines; b) Measured rates of mild steel erosion–corrosion (Lotz and Postlethwaite) and predicted rates of corrosion and erosion of the base metal using the mass transfer correlation

It is clear that the dominant mode of metal loss is corrosion, with the sand removing the protective rust film. The rate of erosion of the base metal metal was an order of magnitude smaller than the rate of corrosion.

The more general approach – solution of full mass transport equations coupled with the LRN model for the boundary conditions, was tested subsequently (Nešić and Postlethwaite [92]). Comparison of the overall predicted rate of metal loss (corrosion + erosion), is in moderate agreement with the measured erosion–corrosion rate (Fig. 7.24b) in this case. The character of the metal loss profile is captured in the predictions. The obtained discrepancy is largest (35%) in the region before the reattachment point (in the recirculation zone) where the turbulence model used overpredicts turbulent oxygen mass transport. Since the erosion–corrosion surface is rough, while the model is designed for smooth surfaces, an increase in the predicted mass transfer rates of 20% has been included to take into account the increased surface area[3]. Far downstream of the expansion both the measured and the predicted curves asymptotically approach the values given by the well established straight-pipe mass transfer correlation of Berger and Hau [89], shown as the shaded area, with the lower and upper limits being the smooth and rough surface values respectively.

Again it is obtained that the dominant mode of metal loss is corrosion, with the sand removing the protective rust film. The rate of erosion of the base

[3]Based on microphotographs of the crossection of a erosion–corrosion roughened surface

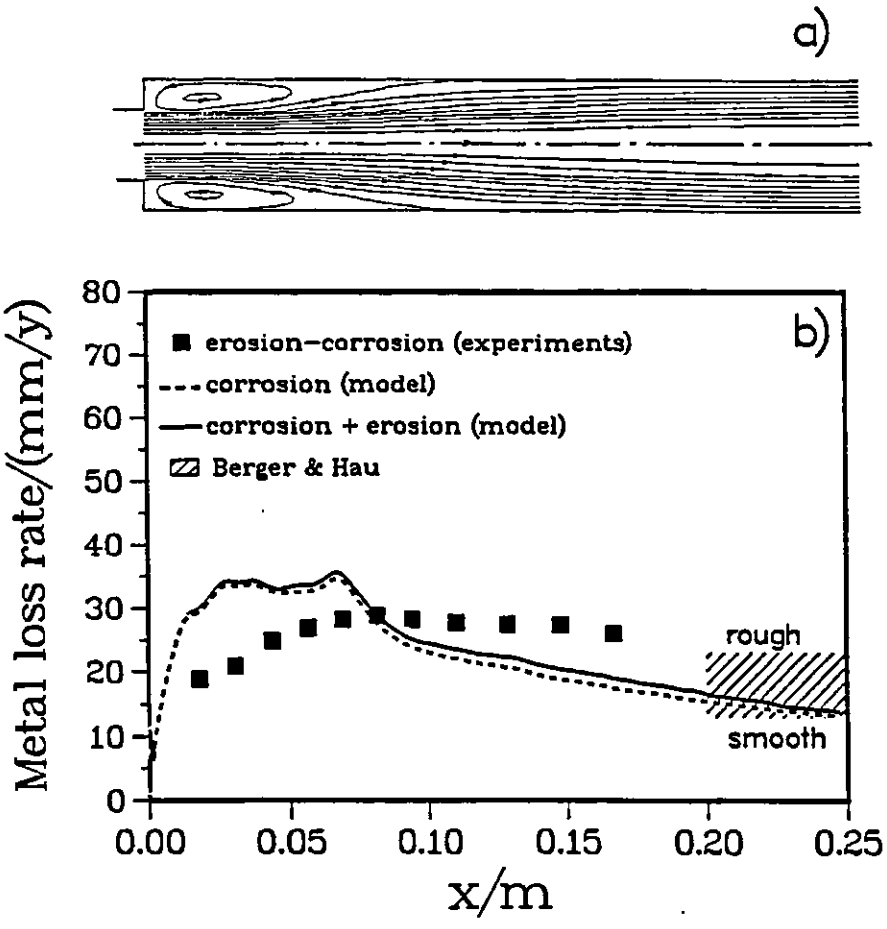

Figure 7.24: 2% sand/water flow through a sudden pipe expansion; d_{in} = 21.1 mm; d_{out} = 42.5 mm; v_{in} = 13.2 m/s; v_{out} = 3.3 m/s; Re_{out}=17.0×10^4. a) Predicted fluid flow streamlines; b) Measured rates of mild steel erosion–corrosion (Lotz and Postlethwaite) and predicted rates of corrosion and erosion of the base metal using the LRN flow and mass transfer model

metal metal was an order of magnitude smaller than the rate of corrosion. The previously used semi–empirical correlation (Fig. 7.23b) for mass–transfer controlled corrosion gave somewhat more accurate predictions for the specific geometry simulated, but is considered less general than the full mass transfer model used subsequently.

Groove. The model was then used to predict the rates of metal loss for flow over a groove in a pipe. It has been reported that in oil and gas production severe erosion–corrosion occured at pipe joints where grooves and/or misfits were present [93],[94]. To study this problem flow of an oxygen–saturated, sand 100 μm diameter in water mixture (1%vol.), at 15 m/s, over a 10 mm groove in a 100 mm diameter pipe was simulated. Predictions of particle–wall impact parameters, erosion and erosion–corrosion profiles are shown in Fig. 7.25 and Fig. 7.26.

The disturbed flow conditions at the groove create increased rates of particle wall impacts far downstream (Fig. 7.25b). However, only in the first 10 mm downstream from the trailing groove edge are the impact angles and velocities significant (Fig. 7.25c and 7.25d). Further, downstream the normal impact velocity decreases under the elastic limit (V_{cr}), and the angles below 2° suggest that only nondestructive 'sliding' impacts occur. Increased rates of erosion are predicted in the first 10 mm (Fig. 7.26b), with the very high erosion rates in the first 2-3 mm. No erosion was predicted inside the groove.

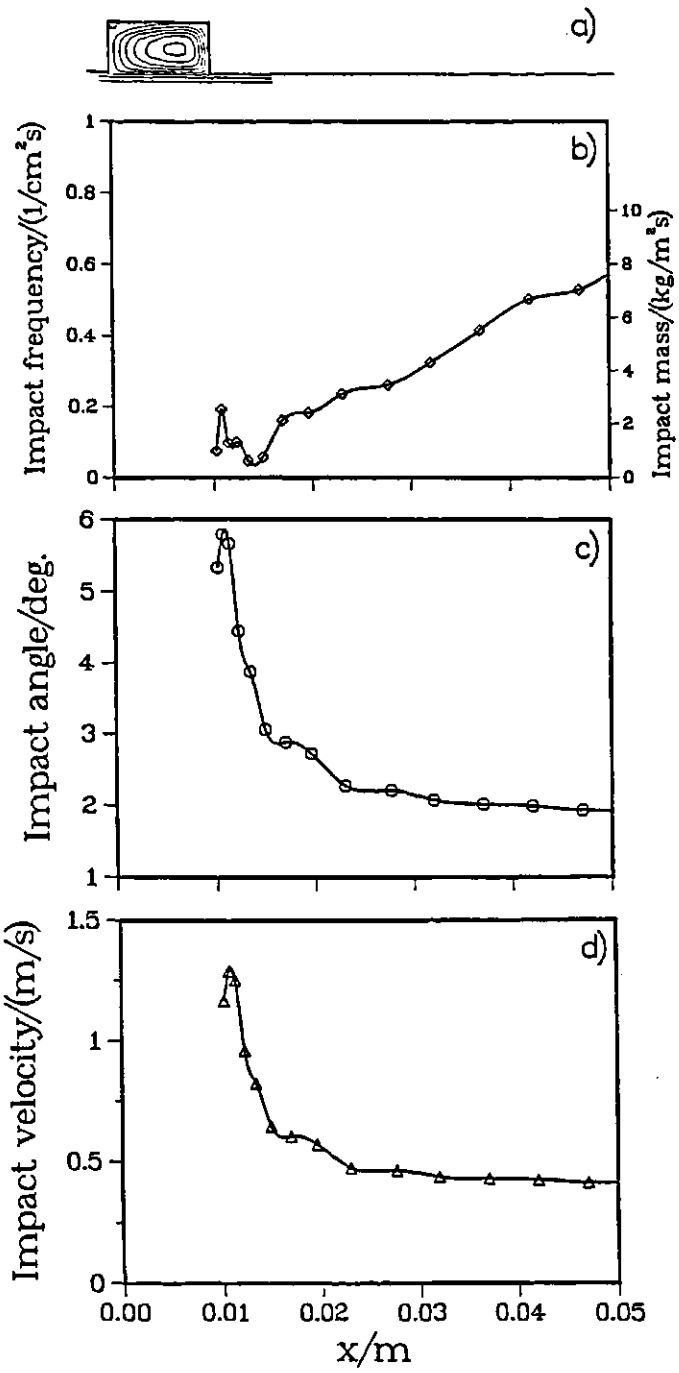

Figure 7.25: 1%vol. sand/water flow over a 10 mm groove in a 100 mm diameter pipe; v = 15 m/s; $Re = 1.87 \times 10^6$. a) Predicted fluid flow streamlines; b) Predicted average particle–wall impact frequency and impact mass; c) Predicted average particle–wall impact angle; d) Predicted average particle–wall impact velocity perpendicular to the wall.

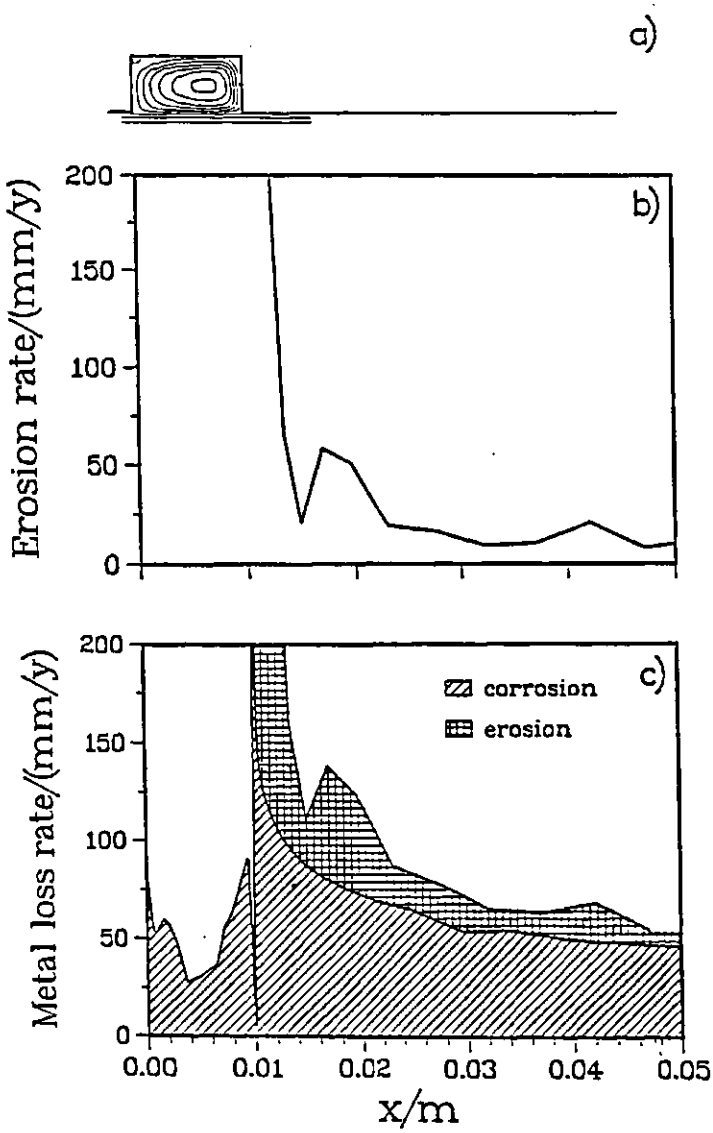

Figure 7.26: 1%vol. sand/water flow over a 10 mm groove in a 100 mm diameter pipe; $v = 15$ m/s; $Re = 1.87 \times 10^5$. a) Predicted fluid flow streamlines; b) Mild steel erosion rate predictions; c) Predictions of corrosion and erosion of mild steel.

The flow disturbance at the downstream edge of the groove also creates increased oxygen–mass transfer rates and corrosion (Fig. 7.26c). At the actual tip the predicted corrosion rate was practically infinite, this effect scaled down within 1 mm downstream. The composite plot (Fig. 7.26c) shows the relative and absolute contributions of the two mechanisms of metal loss. These findings correspond to experimental observations that in case of grooves in pipes most severe damage was located at or very close to the downstream edge [94].

When 400 μm particles were simulated the direct erosion contribution to the overall metal loss was small and the groove did not introduce a significant increase in the local rate of erosion. This is due to the fact that 'heavy' 400 μm particles had high enough inertia which was not significantly affected by the flow disturbance at the groove. Thus the rate of particle–wall impacts and erosion at the groove was similar (low) as elsewhere in the pipe.

Chapter 8

Conclusions

1. For disturbed flow conditions there is no simple relation between the bulk flow parameters and the near-wall hydrodynamics, mass transfer, and erosion–corrosion, so they must be measured or obtained from numerical simulation studies.

2. The hydrodynamics of disturbed flow has been simulated by using a eddy–viscosity $k-\epsilon$ turbulent flow model. In the near wall region two approaches were used, the wall function (WF) approach and the low Reynolds number (LRN) approach. Both were tested by comparing the predictions with LDV measurements of liquid flow through a sudden pipe expansion [44],[18]. Satisfactory agreement for the mean flow parameters has been achieved with both approaches. However, the LRN approach which is significantly costlier from the standpoint of computer memory

and time, predicted better turbulence parameters especially in the near wall region which is important for mass transfer simulations. The hydrodynamic model used can be considered reliable for predicting the flow structure in future erosion–corrosion studies.

3. Rates of mass transfer through the liquid boundary layer are directly related to the levels of turbulence near the wall.

4. To validate the model of mass–transfer–controlled corrosion, mass transfer in aqueous, turbulent, recirculating flow was simulated with a LRN $k-\epsilon$ EVM model. The predictions were tested against experimental data [47], for flow through a sudden pipe expansion ($Re = 2.1 - 13 \times 10^4$ and $Sc = 1460$). Good agreement was obtained over the whole range, without any "tuning" of the transport equations or turbulence model.

5. For flows with high Schmidt numbers, the mass transfer boundary layer is completely embedded within the viscous sublayer. Low levels of turbulent transport in the viscous sublayer, insignificant from the hydrodynamic point of view, override the diffusional mass transport throughout most of the hydrodynamic viscous sublayer. Thus the diffusion controlled mass transfer sublayer is much thinner than the viscous sublayer. Although not initially intended for application in the viscous sublayer, modifications to turbulence models for near wall regions, coupled with the use of the turbu-

lent Schmidt number, enable successful predictions of mass transfer rates in complex turbulent recirculating flow even for high Schmidt numbers.

6. When rust films are present the overall shape (character) of metal loss curve is determined by the transport through the boundary layer (by the flow structure), while the magnitude of the metal loss rate is additionally influenced by the transport through the rust film which acts as a damper. Near-wall turbulence fluctuations affect both. Except in the early stages of corrosion the limiting resistance for mass transfer is in the rust film.

7. The predictions made with the two-phase flow model, which includes a EVM $k-\epsilon$ model of turbulence (WF), accompanied with a Lagrangian Stochastic Deterministic (LSD) model for particle motion, have shown an overall good agreement with the LDV measurements, for flow of water carrying 1000 ppm of 800 μm glass spheres, through a sudden pipe expansion [44]. Some discrepancies obtained for the near–wall region are ascribed to the difficulties in measurements close to the walls, and to the inadequacy of the applied WF approach, for modelling near-wall two-phase flow.

8. An erosion model was incorporated into the LSD model for particle motion. Predictions of erosion rates were in good agreement with the stainless steel erosion measurements, for a 2% water/sand slurry flow through a sudden expansion. The model of erosion used, requires as input only the

yield strength of the eroded material and the critical velocity for plastic deformation. Both are relatively simple to obtain experimentally.

9. Predictions of metal loss by erosion–corrosion were made and compared with erosion–corrosion measurements for flow of oxygen saturated 2% water/sand slurry through a sudden pipe expansion [60]. It was found that the dominant mode of metal loss is corrosion, with the sand removing the protective rust film. Rate of erosion of the base metal was an order of magnitude smaller than the rate of corrosion. The model of erosion-corrosion used was successful in predicting the overall pattern and rate of metal loss.

10. After the model had been successfully verified for its hydrodynamic, corrosion, erosion, and erosion–corrosion predictions for flow through a sudden pipe expansion, erosion–corrosion under disturbed flow conditions created by a groove in a pipe was investigated and the predictions obtained were used to explain patterns and rates of metal loss observed in practice.

11. The model of erosion–corrosion presented is general and can handle a wide variety of different geometries of interest for industry.

Chapter 9

Recommendations

As it usually happens, the more we know, the more we realize how much we do not know. One of the achievements of the present work is that it partially untangled the knot of complex relationships between the fluid/particle flow and erosion–corrosion. It has opened many new questions but it also pointed to the ways that they should be solved. Nearly every aspect of the problem considered in the present work has room for improvement and some of the suggestions are listed below.

1. Hydrodynamics

   - Incorporating body fitted grids in the model would enable modelling of a much wider range of geometries, including curved ducts, rounded edges and nonorthogonal walls. Minor revisions to the computer code would be needed as well as an addition which would handle the grid

generation procedure.

- Extension of the hydrodynamic model to a full three dimensional model would bring the overall model even closer to reality. Further, turbulence and particle motion models would largely benefit as both phenomena are inherently strongly three-dimensional.
- Better turbulence models should be considered such as the Reynolds stress transport models (RSTM) and the benefits for the overall erosion–corrosion model should be estimated.

2. Corrosion

- Corrosion situations with more than one species diffusing should be modelled. This should be relatively easy as mass transport equations for more than one species are built into the computer code as well as the possibility for bulk chemical reactions.
- Study of corrosion under partial coverage of the metal surface with protective films has been initiated and the first findings were encouraging. More should be done on studying this mode of corrosion.
- A model of heat transfer and the effect of local temperature on corrosion rate should be accounted for. The basis for this exists as the computer code has the heat transport equation for determining the temperature field built in, but the relationship between corrosion and

heat transfer has not yet been fully established.

3. Particle motion

   - Movement of the particles under a wider variety of flow and turbulence conditions should be modelled and validated with LDV measurements.
   - More accurate models could be made for particle–wall interactions (e.g. particle reflection angles and velocities).
   - Behaviour of non–spherical particles should be studied as well as particle–particle interactions.
   - The effect on particles on the hydrodynamic and mass transfer boundary layers should be investigated.
   - Higher particle concentrations should be modelled and an alternative Eulerian model should be tested. Since Eulerian models treat particles as just another species the corresponding equations are very similar to existing mass transfer equations so their implementation would be relatively straightforward.

4. Erosion

   - There is room for improvement of the model of erosion to take into account the particle parameters such as shape, surface structure and hardness.

- Erosion of scales and oxide films has not been modelled at all, as very little is known about this phenomenon. Discovering the mechanisms of removal of protective films in both single–phase and two–phase flows should be one of the primary thrusts of future work in erosion–corrosion, as this is a completely missing link in the existing models of localized erosion–corrosion.

5. Erosion–corrosion

- To improve predictions of erosion–corrosion the coupling of individual phenomena should be modelled in more detail. For example the present model accounts for the effect of fluid/particle flow on the erosion–corrosion process but the reverse effect is not modelled. As the metal loss alters the geometry of the flow field this should be fed back into the flow model to get the new flow pattern.
- The previous suggestion implicitly calls for introducing *time* as a new variable in the model. Non-steady state models are the ultimate goal, although as a stepping stone quasi-steady state models should be looked at. This is possible as the time scales of erosion and corrosion are many order magnitudes larger then the ones for the flow. However, even todays fast computers would have troubles with producing comprehensive results for non-steady state models in

a reasonable time frame.

Bibliography

[1] L.Prandtl, "Uber die ausgebildete Turbulenz", *ZAMM*, **5**, p.136. (1925).

[2] T.Cebeci and A.M.O.Smith, "Analysis of Turbulent Boundary Layers", *Applied Mathematics and Mechanics*, **15**, New York Academic (1974).

[3] M.E.Crawford and W.M.Kays, "STAN–5 – A Program for Numerical Computation of Two–Dimensional Internal/External Boundary Layer Flows", *Stanford Univ., Dept. Mech. Eng.*, Report HMT–23 (1975).

[4] P.Bradshaw, D.H.Ferris and N.P.Atwell, "Calculation of Boundary Layer Development Using the Turbulent Energy Equation", *J. Fluid. Mech.*, **28**, pp.593–616 (1967).

[5] C.C.Shir, "A Preliminary Numerical Study of Atmospheric Turbulent Flows in the Idealised Planetary Layer", *J. Atmospheric Sciences*, **30**, p.1327 (1973).

[6] M.M.Gibson and D.B.Spalding, "Two–Equation Model of Turbulence Applied to the Prediction of Heat and Mass Transfer in Wall Boundary Layers", *ASME 72-HT-15*, New York, pp.1–8 (1972).

[7] W.P.Jones and B.E.Launder, "The Calculation of Low–Reynolds Number Phenomena with a Two–Equation Model of Turbulence", *Int. J. Heat Mass Transfer*, **16**, pp.1119–1130 (1973).

[8] A.D.Gosman, E.E.Khalil and J.H.Whitelaw, "The Calculation of Two–Dimensional Turbulent Recirculating Flow", in *Turbulent Shear Flows I*, F.Durst, B.E.Launder, F.W.Schmidt and J.H.Whitelaw, Eds., Springer–Verlag, New York, pp.237–255 (1979).

[9] L.H.Back and E.J.Roschke, "Shear–Layer Flow Regimes and Wave Instabilities and Reattachment Lengths Downstream of an Abrupt Circular Channel Expansion", *ASME, J.Appl.Mech.*, **94**, pp.677–681 (1972).

[10] Ha Minh,H. and P.Chassaing, "Perturbations of Turbulent Pipe Flow", in *Turbulent Shear Flows I*, F.Durst, B.E.Launder, F.W.Schmidt and J.H.Whitelaw, Eds., Springer–Verlag, New York, pp.178–197. (1979).

[11] R.D.Gould, W.H.Stevenson. and H.D.Thompson, "Investigation of Turbulent Transport in an Axisymmetric Sudden Expansion", *AIAA J.*, **28**, pp.276–283 (1990).

[12] C.R.Yap, "Turbulent Heat and Momentum Transfer in Recirculating and Impinging Flows", *Ph.D. thesis*, Univ. of Manchester, Manchester, U.K. (1987).

[13] J.W.Baughn, M.A.Hoffman, B.E.Launder, D.Lee and C.Yap, "Heat Transfer, Temperature and Velocity Measurements Downstream of an Abrupt Expansion in a Circular Tube at a Uniform Wall Temperature", *ASME J.Heat Transfer*, **111**, pp.870–876 (1989).

[14] S.Hirai, T.Takagi and T.Higashiya "Numerical Prediction of Flow Charachteristics and Retardation of Mixing in a Turbulent Swirling Flow", *Int.J.Heat Mass Transfer*, **32**, pp.121–130 (1989).

[15] L.Khezzar, J.H.Whitelaw and M.Yianneskis, "An Experimental Study of Round Sudden Expansion Flows", *Proc. 5th Symp. on Turb. Shear Flows*, Cornell Univ. pp.5–25 (1985).

[16] R.T.Szczepura, "Flow Characteristics of an Axisymmetric Sudden Pipe Expansion: Results Obtained from the Turbulence Studies Rig, Part I: Mean and Turbulence Velocity Results", *Report TPRD/B/0702/N85*, CEGB, Berkeley Nuclear Laboratories, U.K. (1985).

[17] R.P.Durrett, W.H.Stevenson and H.D.Thompson, "Radial and Axial Turbulent Flow Measurements with an LDA in an Axisymmetric Sudden Expansion Air Flow", *ASME, J.Fluids Engng.*, **110**, pp.367–372 (1988).

[18] M.Stieglmeier, C.Tropea, N.Weiser and W.Nitsche, "Experimental Investigation of the Flow Through Axisymmetric Expansions", *ASME, J. Fluids Engng.*, **111**, pp.464–471 (1989).

[19] C.T.Crowe, "Review Numerical Methods for Dilute Gas–Particle Flows", *ASME J. Fluids Engng.*, **104**, pp.91–96 (1982).

[20] G.Hestroni, "Particles–Turbulence Interaction", *ASME Fed-Vol.75*, New York, pp.1–12 (1988).

[21] S.Elgobashi, T.Abou–Arab, M.Rizk and A.Mostafa, "Prediction of the Particle–Laden Jet with a Two–equation Turbulence Model", *Int. J. Multiphase Flow*, **10**, pp.697–710 (1984).

[22] S.Elgobashi and T.W.Abou–Arab, "A Two-Equation Turbulence Model for Two–Phase Flows", *Phys. Fluids*, **26**, pp.931–938 (1983).

[23] D.Modarress, H.Tan and S Elgobashi, "Two–Component LDA Measurements in a Two–Phase Turbulent Jet", *AIAA J.*, **22**, pp.624–630 (1984).

[24] M.A.Rizk and S.Elgobashi, "A Two–Equation Turbulence Model for Dispersed Dilute Confined Two–Phase Flow", *Int. J. Multiphase Flow*, **15**, pp.119–133 (1989).

[25] Y.Tsuji, Y.Morikawa and H.Shiomi, "LDA Measurements of an Air–Solid Two–Phase Flow in a Vertical Pipe", *J. Fluids Mech.*, **139**, pp.417–434 (1984).

[26] M.Maeda, K.Hishida and T.Furutani, "Optical Measurements of Local Gas and Particle Velocity in an Upward Flowing Dilute Gas–Solids Suspension", in *Proc. Polyphase Flow and Transport Technology*, Century 2-ETC, San Francisco, p.211 (1980).

[27] F.Pourahmadi and J.A.C.Humphrey, "Modelling Solid–Fluid Turbulent Flows With Application to Predicting Erosive Wear", *Physico–Chemical Hydrodynamics*, **4**, pp.191–219 (1983).

[28] R.L.Peskin, "Stochastic Estimation Applications to Turbulent Diffusion", *Proc. Int. Symp. on Stochastic Diffusion*, C.L.Chiu ed., Univ. Pittsburg, p.251, (1971).

[29] D.Milojević, T.Borner, F.Durst, "Prediction of Turbulent Gas-Particle Flow Measurement in a Plain Confined Jet", *Proc. World Congress Particle Technology, Part IV*, Partikel Technologie Nurnberg, Nurnberg, pp.485–505 (1986).

[30] D.Milojević, "Two-Dimensional Turbulent Flow of a Fluid/Particle Mixture – With Heat and Mass Transfer Aspects", *Ph.D. thesis* in Serbo–Croatian, Univ. of Beograd, Beograd, Yugoslavia (1986).

[31] W.H.Snyder, J.L.Lumley, "Some Measurements of Particle Velocity Autocorrelation Functions in a Turbulent Flow", *J. Fluid Mech.*, **48**, pp.41–71 (1971).

[32] M.R.Wells, D.E.Stock, "The Effect of Crossing Trajectories on the Dispersion of Particles in a Turbulent Flow", *J. Fluid Mech.*, **136**, pp.31–62 (1983).

[33] G.Arnason, "Measurement of Particle Dispersion in Turbulent Pipe Flow", *Ph.D. thesis*, Washington State University, Pullman (1982).

[34] A.Berlemont, P.Desjonqueres and G.Gouesbet, "Particle Lagrangian Simulation in Turbulent Flows", *Int. J. Multiphase Flow*, **16**, pp.19–34 (1990).

[35] K.Hishida, K.Kaeneko and M.Maeda, "Turbulence Structure of a Gas–Solid Two–Phase Circular Jet", *Trans. JSME Ser. B*, **51**, pp.2330–2337 (1985).

[36] J.S.Shuen, A.S.P.Solomon, Q.F.Zhang and G.M.Faeth, "Structure of Particle Laden Jets", *Report AIAA-84-0038* (1985).

[37] T.Durst,D.Milojević and B.Schonung, "Eulerian and Lagrangian Predictions of Particulate Two–Phase Flows: A Numerical Study", *Appl. Math. Model.*, **8**, pp.101–115 (1984).

[38] A.A.Mostafa and Mongia, "On Modelling of Turbulent Evaporating Sprays: Eulerian versus Lagrangian approach", *Int. J. Heat Mass Transfer*, **30**, pp.2583–2593 (1987).

[39] A.S.P.Solomon, J.S.Shuen, Q.F.Zhang and G.M.Faeth, "A Theoretical and Experimental Study of Turbulent Evaporating Sprays", *NASA CR 174760* (1984).

[40] A.Adeniji–Fashola and C.P.Chen, "Modelling of Confined Turbulent Fluid–Particle Flows Using Eulerian and Lagrangian Schemes", *Int. J. Heat Mass Transfer*, **33**, pp.691–701 (1990).

[41] S.L.Lee and F.Durst, "On the Motion of Particles in Turbulent Duct Flows", *Int. J. Multiphase Flow*, **8**, pp.125–146 (1982).

[42] B.Ruck and B.Makiola, "Particle Dispersion in a Single–Sided Backward–Facing Step Flow", *Int. J. Multiphase Flow*, **14**, pp.787–800 (1988).

[43] C.J.Park and L.-D.Chen, "Experimental Investigation of Confined Turbulent Jets Part II: Particle–Laden Flow Data", *AIAA J.*, **27**, pp.1511–1516 (1989).

[44] W.Blatt, T.Kohley, U.Lotz and E.Heitz, "The Influence of Hydrodynamics on Erosion–Corrosion in Two-Phase Liquid/Particle Flow", *Corrosion*, **45**, pp.793-803 (1989).

[45] E.Heitz, "Chemo–Mechanical Effects of Flow on Corrosion", *NACE Corrosion/90 Conf.*, paper No.1, NACE, Houston (1990).

[46] J.Postlethwaite, "Effect of Resistance to Mass Transport on the $M^{z+} + z \rightleftharpoons M$ reaction" *Electochimica Acta*, **15**, pp.1847–1852 (1970).

[47] T.Sydberger and U.Lotz, "Relation Between Mass Transfer and Corrosion in a Turbulent Pipe Flow", *J.Electrochem.Soc.*, **129** pp.276–283 (1982).

[48] L.W.Shemilt, C.Y.Cha, E.Fiadzigbe, A.B.Ponter, "Steel Pipe Corrosion Under Flow Conditions – III Effect of Sulphate Ion", *Corros. Sci.*, **20**, pp.443–455 (1980).

[49] H.R.Copson, "Effects of Velocity on Corrosion by Water", *Ind. and Eng. Chem.*, **44**, pp.1745–1752 (1952).

[50] B.K.Mahato, S.K.Voora and L.W.Shemilt, "Steel Pipe Corrosion Under Flow Conditions – I. An Isothermal Correlation for a Mass Transfer Model", *Corros. Sci.*, **8**, pp.173–193 (1968).

[51] K.D.Efird, "Effect of Fluid Dynamics on the Corrosion of Copper–Base Alloys in Sea Water", *Corrosion*, **33**, pp.3–8 (1977).

[52] D.C.Silverman, "Rotating Cylinder Electrode for Velocity Sensitivity Testing", *Corrosion*, **20**, pp.443–455 (1980).

[53] W.Blatt and E.Heitz,, "Hydromechanical Measurements for Erosion–Corrosion", *NACE Corrosion/90 Conf.*, paper No.25, NACE, Houston (1990).

[54] S.Nešić and J.Postlethwaite, "Erosion–Corrosion Under Disturbed Flow Conditions in Slurry Pipelines", *NACE Corrosion/90 Conf.*, paper No.26, NACE, Houston (1990).

[55] S.Nešić and J.Postlethwaite, "Relationship Between the Structure of Disturbed Flow and Erosion–Corrosion", *Corrosion*, **46**, pp.874–880 (1990).

[56] B.C.Syrett, "Erosion–Corrosion of Copper–Nickel Alloys in Sea Water and Other Aqueous Environments – A Literature Review", *Corrosion*, **32**, pp.242–252 (1976).

[57] H.Zeisel and F.Durst, "Computations of Erosion–Corrosion Processes in Separated Two-Phase Flows", *NACE Corrosion/90 Conf.*, paper No.29, NACE, Houston (1990).

[58] C.Loss and E.Heitz, "Zum Mechanismus der Erosionkorrosion in schnell stromenden Flussigkeiten", *Werkstoffe u. Korrosion*, **24**, pp.38–48 (1973).

[59] J.Postlethwaite, M.H.Dobbin and K.Bergevin, "The Role of Oxygen Mass Transfer in the Erosion–Corrosion of Slurry Pipelines", *Corrosion*, **42**, pp.514–521 (1986).

[60] U.Lotz and J.Postlethwaite, "Erosion–Corrosion in Disturbed Two–Phase Liquid/Particle Flow", *Corros. Sci.* **30**, pp.95–106 (1990).

[61] U.Lotz, "Velocity Effects in Flow Induced Corrosion", *NACE Corrosion/90 Conf.*, paper No.27, NACE, Houston (1990).

[62] I.Finnie, "Erosion of Surfaces by Solid Particles", *Wear*, **3**, pp.87–103 (1960).

[63] G.Sundararajan and P.G.Shewmon, "A New Model for the Erosion of Metals at Normal Incidence", *Wear*, **84**, pp.237–258 (1983).

[64] C.de Waard and D.E.Milliams, "Carbonic Acid Corrosion of Steel", *Corrosion*, **31**, pp.177–181 (1975).

[65] D.Migdal and V.D.Agosta, "A Source Flow Model for Continuum Gas–Particle Flow", *Trans. ASME J. Appl. Mech.*, **34E**, pp.860–865 (1967).

[66] J.Boussinesq, "Essai sur la théorie des eaux courantes", *Mém prεés/ par div. savant à l'acad sci.*, Paris (1877).

[67] A.N.Kolmogorov, "Equations of Turbulent Motion of an Incompressible Fluid", *Izv. Akad. Nauk. SSR, Seria Fizicheska VI*, **No.1-2**, pp.56-58 (1942).

[68] L.Prandtl, " Bermerkungen zur theorie der freien turbulenz", *ZAMM*, **22**, pp.241–243 (1942).

[69] K.Hanjalić, V.Vujović and M.Ivanović, "Modelling of Buoyancy Effects in Turbulent Shear Flows with Suspended Particles" in Serbo-Croatian, *Mathematical Models of Turbulent Transport Processes*, ANU BiH, pp.117–137 (1984).

[70] H.Schlichting, *Boundary Layer Theory*, 7^{th} edition, McGraw–Hill (1979).

[71] V.Levich, *Physicochemical Hydrodynamics* Prentice–Hall, pp.144–154 (1962).

[72] V.C.Patel, W.Rodi and G.Scheurer, "Turbulence Models for Near-Wall and Low Reynolds Number Flows: a Review", *AIAA J.*, **23**, pp.1308–1319 (1985).

[73] C.K.G.Lam and K.Bremhorst, "A Modified Form of the $k-\epsilon$ Model for Predicting Wall Turbulence", *ASME J.Fluids Eng.*, **103**, pp.456–460 (1981).

[74] Y.Nagano and M.Hishida, "Improved Form of the $k-\epsilon$ Model for Wall Turbulent Shear Flows", *ASME J.Fluids Eng.*, **109**, pp.156–160 (1987).

[75] S.V.Patankar, *Numerical Heat Transfer and Fluid Flow*, McGraw-Hill, (1980).

[76] S.V.Patankar and D.B.Spalding, "A Calculation Procedure for Heat, Mass and Momentum Transfer in Three–Dimensional Parabolic Flows", *Int. J. Heat Mass Transfer*, **15**, pp.1787–1806 (1972).

[77] W.M.Kays and M.E.Crawford, *Convective Heat and Mass Transfer*, McGraw-Hill, pp.225-229 (1980).

[78] B.E.Launder, "Second–Moment Closure and Its Use in Modelling Turbulent Industrial Flows", *Int. J. Numerical Methods in Fluids*, **9**, pp.963–985 (1989).

[79] B.E.Launder, "Review: Second–Moment Closure: Present ...and Future", *Int. J. Heat and Fluid Flow*, **10**, pp.282–300 (1989).

[80] A.V.Levy, "The erosion of metal alloys and their scales", *Proc. Corrosion erosion wear of materials in emerging fossil energy systems*, NACE, Houston, pp.298–376 (1982).

[81] I.Finnie, J.Wolak, and Y.Kabil, "Erosion of Metals by Solid Particles", *J. of Materials*, **2**, pp.682-700 (1967).

[82] J.G.A.Bitter, "A Study of Erosion Phenomena – Part II", *Wear*, **6**, pp.169–163 (1963).

[83] J.G.A.Bitter, "A Study of Erosion Phenomena – Part I", *Wear*, **6**, pp.5–21 (1963).

[84] K.Bergevin, "Effect of Slurry Velocity on the Mechanical and Electrochemical Components of Erosion–Corrosion in Vertical Pipes", *M.Sc. thesis*, Univ. of Saskatchewan, Saskatoon, Canada (1984).

[85] J.Postlethwaite, B.J.Brady, E.B.Tinker, "Study of Erosion-Corrosion Wear Patterns in Pilot Plant Slurry Pipelines", *Fourth International Conference on the Hydraulic Transport of Solids in Pipes*, paper J2, Banff, Canada, pp.17-26 (1976).

[86] S.Nešić and J.Postlethwaite, "Hydrodynamics of Disturbed Flow and Erosion–Corrosion, Part I – A Single–Phase Flow Study", *Can. J. Chem. Eng.*, **69**, pp.698–703 (1991).

[87] S.Nešić and J.Postlethwaite, "Hydrodynamics of Disturbed Flow and Erosion–Corrosion, Part II – A Two–Phase Flow Study", *Can. J. Chem. Eng.*, **69**, pp.704–710 (1991).

[88] S.Nešić and J.Postlethwaite, to appear in *Int.J.Heat Mass Transfer* (1991).

[89] F.P.Berger and K.-F. F.-L. Hau, "Mass Transfer in Turbulent Pipe Flow Measured by the Electrochemical Method", *Int.J.Heat Mass Transfer*, **20**, pp.1185–1194 (1977).

[90] H.Tennekes and J.L.Lumley, *A First Course in Turbulence*, MIT Press, London, pp.156–162, (1987).

[91] J.Postlethwaite and U.Lotz, "Mass Transfer at Erosion–Corrosion Roughened Surfaces", *Can. J. Chem. Eng.*, **66**, pp.75–78 (1988).

[92] S.Nešić and J.Postlethwaite, "A Predictive Model of Localized Erosion–Corrosion", to appear in *Corrosion* in August 1991.

[93] J.S.Smart, "A Review of Erosion–Corrosion in Oil and Gas Production", *NACE Corrosion/90 Conf.*, paper No.10, NACE, Houston (1990).

[94] G.Schmitt, W.Bruckhoff, K.Faessler and G.Blummel, "Flow Loop Versus Rotating Probes – Correlations Between Experimental Results and Service Applications", *NACE Corrosion/90 Conf.*, paper No.23, NACE, Houston (1990).

Nomenclature

a_N, a_S, a_E, a_W - transport coefficients in the discretized transport equations

A^p - projected area for the particle

c - volume concentration or constant

C_D - drag coefficient

$C_\mu, C_{\epsilon 1}, C_{\epsilon 2}, C_{\epsilon 3}$ - constants in the $k-\epsilon$ model of turbulence

D - mass diffusion coefficient

E - constant in the logarithmic law-of-the-wall or voltage

$\mathcal{E}$ - Young's modulus.

$\tilde{e}, e, E$ - strain rate (instantaneous, fluctuating, mean)

f - mass fraction of particles in the overall particle mass flow rate $\dot{m}^p$

f_μ, f_1, f_2 - constants in the LRN turbulence model

F - body force (e.g. gravity)

G - mass flow rate

h - enthalpy

i - current density

J - total flux

k - kinetic energy of turbulence or mass transfer coefficient

$\vec{l}^p$ - particle coordinate vector

L - length scale

m - mass

$\dot{m}^p$ - overall particle mass flow rate

$\check{m}^p$ - particle–wall impact rate (mass)

$\tilde{m}, m, M$ - species mass concentration (instantaneous, fluctuating, mean)

n_i - number of particle size fractions

n_j - number of particle starting locations

n_k - number of trajectories assigned to each starting location

n^p - number of particles in a control volume

$\dot{N}^p_{ijk}$ - the number of particles moving along a particular trajectory "ijk"

p' - pressure correction

$\tilde{p}, p, P$ - pressure (instantaneous, fluctuating, mean)

Pe - Peclet number

Pr - Prandtl number

q - flux

Q - volume of metal eroded

r - radial coordinate

R - universal gas constant

$\mathbf{R}$ - scale retention ratio

Re - Reynolds number

Re_y - turbulence Reynolds number

Re_T - turbulence Reynolds number

$\tilde{s}, s, S$- source term (instantaneous, fluctuating, mean)

S_C, S_P - coefficients of the linearized source term

Sc - Schmidt number

T - absolute temperature

T_u - turbulence intensity

u, v, w - components of the fluctuation velocity vector

$\tilde{u}, \tilde{v}, \tilde{w}$ - components of the instantaneous velocity vector

U, V, W - components of mean velocity vector

U^+ - nondimensional velocity

U_τ - friction velocity

$\vec{V}$ - velocity vector

x, y, z - Cartesian coordinates

y^+ - nondimensional distance from the wall

Greek letters

α - impact angle

Γ - diffusion coefficient

δ - boundary layer thickness

δ_{ij} - Kronecker's delta operator

δ, ∂ - differentiating operators

ϵ - dissipation of kinetic energy of turbulence

ε - energy needed to remove a unit volume of material by deformation wear

ϑ - Poisson's ratio

κ - constant in the logarithmic law-of-the-wall

μ - dynamic viscosity

μ_t - turbulent viscosity

ν - kinematic viscosity

ξ - underrelaxation factor

ϱ - amount of energy needed to "scratch" out a unit volume from the surface

σ - stress

σ_o - yield strength

$\sigma_k, \sigma_\epsilon, \sigma_\Phi, \sigma_m$ - turbulent Prandtl-Schmidt numbers

τ - time

τ_w - wall shear stress

$\tilde{\tau}^p$ - particle relaxation time

Φ - general variable

ψ - source term or angle

ψ_R - reflection coefficient

ρ - density

Υ - elastic load limit

Subscripts

a - refers to anodic

b - refers to bulk

c - refers to node "c" closest to the wall in the WF approach, or to cathodic

C - refers to cutting wear

cr - refers to a critical value

D - refers to deformation wear

e - refers to "east" face of the control volume

eff - refers to effective value (molecular + turbulent)

i - particle size fraction counter

j - particle starting location counter

k - particle trajectory counter

i, j, k - refers to differentiation with respect to the three coordinate directions

k - refers to kinetic energy of turbulence

l - refers to a coordinate direction, or to liquid

m - refers to molecular

m, M - refers to mass

n - refers to "north" face of the control volume

o - refers to overall

R - refers to reflection

s - refers to "south" face of the control volume, or to the surface, or to scale

t - refers to turbulent value

U, V, W - refers to the x, y, z momentum equation

w - refers to wall or "west" face of the control volume

x, y, z - refer to the x, y and z coordinate directions

ϵ - refers to dissipation of kinetic energy of turbulence

Φ - refers to a general variable

$\perp$ - refers to a perpendicular component

$\|$ - refers to a parallel component

Superscripts

d - refers to deviatoric

p - refers to particles

s - refers to species

Φ - refers to a general variable

$\tilde{}$ - stands for instantaneous value

$'$ - stands for standard deviation

Acronyms

ASM - Algebraic stress model

CPU - Central processing unit

EVM - Eddy viscosity model

LDV - Laser Doppler velocimetry

LRN - Low Reynolds number

LSD - Lagrangian stochastic–deterministic

RSTM - Reynolds stress transport models

WF - Wall function